Topological Disorder in Phosphate and Other Ceramics

by

Attiganal Narayanaswamy Sreeram

Submitted to the Department of Materials Science and Engineering
in partial fulfillment of the requirements for the degree of

Doctor of Science in Ceramics

at the

MASSACHUSETTS INSTITUTE OF TECHNOLOGY

September 1995

Author .....
Department of Materials Science and Engineering
August 11, 1995

Certified by .....
Linn W. Hobbs
John F. Elliott Professor of Materials
Thesis Supervisor

Accepted by .....
Carl V. Thompson II
Chairman, Departmental Committee on Graduate Students

Topological Disorder in Phosphate and Other Ceramics

by

Attiganal Narayanaswamy Sreeram

Submitted to the Department of Materials Science and Engineering
on August 11, 1995, in partial fulfillment of the
requirements for the degree of
Doctor of Science in Ceramics

Abstract

Single crystals of lead pyrophosphate ($Pb_2P_2O_7$) and aluminum orthophosphate ($AlPO_4$) were irradiated with 200 kV TEM electrons to a fluence $\sim 10^{27} e/m^2$. High resolution transmission electron microscopy and electron diffraction were used to investigate the mechanism of radiolysis for the two single crystals. Lead pyrophosphate single crystals were found to be beam stable up to this high fluence whereas aluminum orthophosphate readily amorphizes at surprisingly low electron fluence of $\sim 2 \times 10^{23} e/m^2$.

Single crystals of lead pyrophosphate, lead pyrophosphate glasses and lead metaphosphate glasses were ion irradiated with 100 kV P^+ ions with several fluences in the range of $1 \times 10^{15}/m^2$ - $2 \times 10^{20}/m^2$ and with 55 kV O^+ ions with several fluences in the range of $1 \times 10^{16}/m^2$ - $1 \times 10^{21}/m^2$. Cross-section high resolution transmission electron microscopy (XTEM-HRTEM), zero-loss cross-section scanning transmission electron microscopy imaging (XTEM-STEM), energy-filtered electron diffraction (EFED) and high performance liquid chromatography flow injection analysis (HPLC-FIA) were used to characterize the metamict crystals and glasses.

The lead pyrophosphate single crystals undergo metamictization under 100 kV P^+ and 55kV O^+ ions at fluences lower than $1 \times 10^{17}/m^2$, indicating relative ease of amorphization of phosphates in comparison with other ceramic materials. Furthermore, the interface between the completely diffraction-amorphous layer and the pristine single crystalline layer of the metamict lead pyrophosphate single crystals was very sharp, almost one atom plane sharp, for fluences over and above a certain threshold, as revealed by XTEM-HRTEM. EFED results further revealed a strong reduction in the intensities of the first sharp diffraction peak (FSDP) for all of the metamict phosphates, glass or single crystal. This indicates a significant change in the medium-range-order which was confirmed by the radial distribution functions (RDFs) generated from EFED data of metamict phosphates. HPLC-FIA results reconfirmed that the medium-range-order for all of the metamict phosphates are different.

Topological descriptions were made in terms of of connectivity $\{V, C\}$ and struc-

tural freedom f for phosphate and also for a wide range of structures found in various ceramic materials. Ceramic materials (structures) with values of structural freedom, $f > 0$, amorphize readily while those with values of $f < 0$ tend to remain crystalline until very high ion irradiation fluences. A criteria for topological disorder (f) for a wide range of ceramic materials is proposed, and for the first time, able to explain the wide ranging amorphizability of ceramic materials.

Thesis Supervisor: Linn W. Hobbs
Title: John F. Elliott Professor of Materials

Acknowledgments

I would like to express my gratitude towards my advisor Prof. Linn W. Hobbs for introducing me to the subject of this thesis and for providing an opportunity to obtain a doctorate degree from M.I.T. His support and encouragement throughout the course of this study is most appreciated. I would also like to thank Profs. Yet-Ming Chiang and W. H. Orme-Johnson to have served as members of my thesis committee and provide helpful suggestions. I appreciate all the help from CMSE staff members: J. Adario, W. Correa, J. DiFrancesco, Dr. A. J. Garratt-Reed, M. Frongillo, P. Kearney, R. Perilli and F. Wilson; without their help this study could not have been completed efficiently. I also like to thank Drs. Ning Yu and M. Nastassi of Los Alamos National Laboratory for O^+ Ion-Implantations and Drs. B. C. Sales and L. A. Boatner of Oak Ridge National Laboratory for their help with the HPLC-FIA experiments. I also thank Prof. R. C. Ewing for providing berlinte samples for this study.

I would like to extend my utmost thanks for Dr. L. C. Qin for his friendship and help in particular with the theory of electron diffraction. I also thank Dr. Michael Liberatore for his longanimity, moral support and friendship throughout the course of my stay at M.I.T. Friendship and help from other graduate student friends at M.I.T. Atul Adya, Kin Ha, Satbir Khanuja, Vikas Sharma, Ujjwal Sinha, Dr. C. S. Yoon and also Aman Rustagi is most appreciated. I am unable to collect enough euphemism to thank all of the above friends mentioned in this paragraph for their uncanny support and friendship. In addition, I would also like to thank ex- and current groupmates, officemates and friends, whose names too numerous to mention, for all their help.

My parents, brother and sister always deserve my thanks for their unending encouragement to do and thrive for the best. I would also like to thank my wife for all her support and love that she provided me with when we got married during the final stages of this study. Last but not the least, I thank my uncle Dr. A. R. Vasudevamurthy, emeritus professor of inorganic and mineral chemistry, Indian Institute of Science, Bangalore, India, for his encouragements, guidance and help; whom I consider my idol and dedicate this thesis to.

Contents

List of Figures

List of Tables

Chapter 1

Introduction

The science and technology of noncrystalline materials have intrigued scientists for well over a century. Several terminologies have been used to describe these materials such as glass, amorphous, aperiodic and metamict. Glass is traditionally defined as an inorganic product of fusion that has cooled to a rigid condition without crystallizing. Two problems with such a definition of glass become readily apparent: Firstly, several polymers (an organic product of fusion) are found to be glassy and this was realized quite early [1, 2]. Secondly, some glasses like elemental selenium glass can be formed by vapor deposition techniques in addition to the traditional method of thermal quenching; therefore a glass does not have to be formed as 'a product of fusion' (fusion in glass technology essentially means melting). The term metamict was first coined in the late nineteenth century [3] to classify a group of naturally occurring materials which, while retaining crystalline habit, exhibited glass-like properties, such as lower than normal density, conchoidal fracture, isotropic optical behavior, etc. These phenomena were later found to be the result of damage from recoil α-emitting radionuclides accumulating over geologic periods in these materials [4, 5]. The Webster's Third New International Dictionary (1986), defines metamict materials as amorphous because of the disruption of crystal structure by radiation contained or nearby radioactive atoms. The terms noncrystalline, amorphous and aperiodic have been used in the literature interchangeably for over five decades now, to describe any material that is diffraction-amorphous (x-ray, electron or neutron). We prefer to use

the term 'topologically disordered', because all of the classes of materials mentioned above are essentially topologically disordered. A structure is topologically ordered if it has long-range orientational order and translational periodicity, i.e., if the material is crystalline; otherwise the material is topologically disordered. However, the structural connectivity of the topologically disordered material can be identical to that of the corresponding crystal of exactly the same chemical composition as illustrated in Fig. 1-1. At this point it is enough to mention that topological descriptions will be discussed in detail in chapters 3 and 4.

1.1 Motivations for Study

The motivations for this study fall into two main categories, *viz*, radiation damage of ceramics and to establish a criteria for all of ceramic materials that can describe the behavior (amorphization) of these materials as a response to radiation. When we mention radiation in this manuscript, we mean energetic fast particle (electrons and ions) radiation.

1.1.1 Motivation to study radiation damage of ceramics

Ceramic materials are exposed to adverse radiation environments such as in fission reactors, fusion reactors, high-level nuclear waste storage materials, ion-beam techniques (processing as well as characterization), radiation exposure in space applications, etc., which have a significant impact in determining the choice of materials for application under radiation environments. The response to radiation of ceramic materials often result in a change of a range of important materials properties such as strength, toughness, electrical and thermal conductivities, dielectric response, bulk density, chemical durability, optical behavior and loss of crystallinity [6]. This study focuses on the last response mentioned, i.e., loss of crystallinity or more loosely amorphization. Phosphate ceramics are of particular interest because of the recent interest in lead-iron phosphate glass [7] as a potential candidate for high-level nuclear waste storage. Besides, very limited structural studies have been reported in literature of ra-

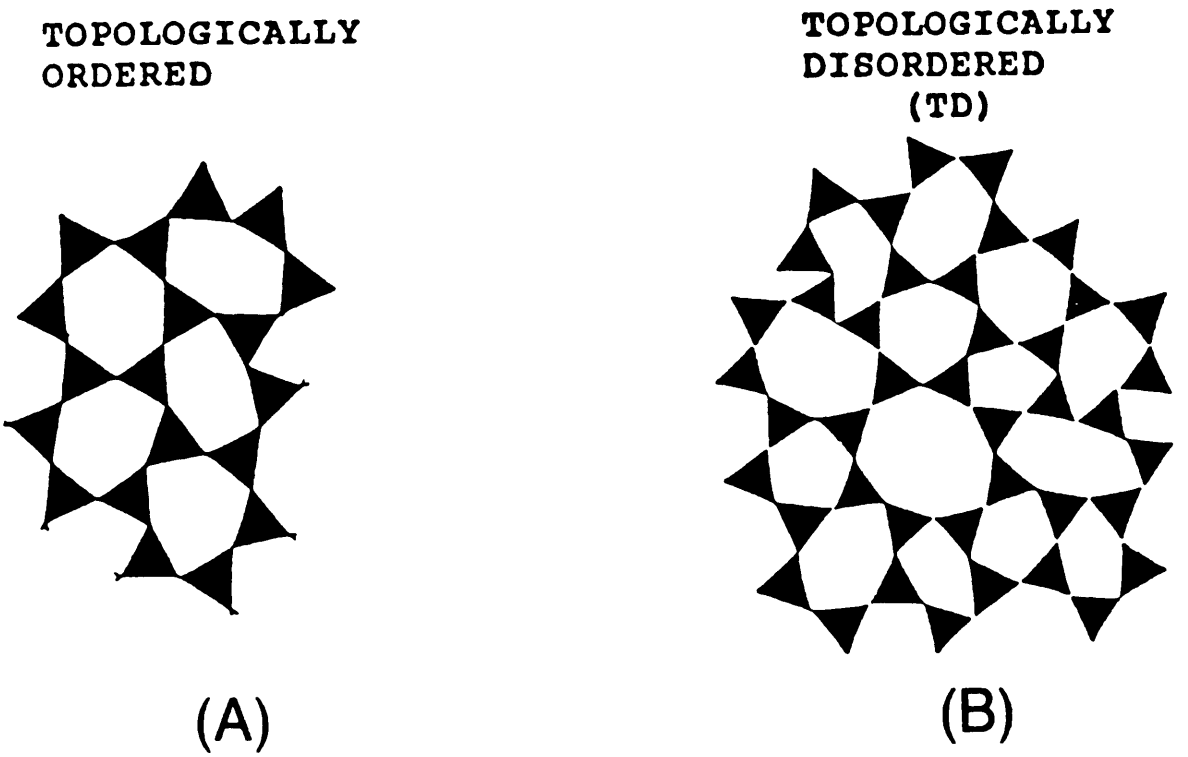

Figure 1-1: Schematic representation of a structure displaying topological order (A) and topological disorder (B). (Described in detail in Chapter 3.)

diation damage to phosphate ceramics. Inspite of a plethora of literature is available for radiation damage studies, structural or otherwise, for silica and silicate glasses [6], one cannot extrapolate the available information to phosphate glasses mainly because the former is based on a 4-corner-sharing tetrahedral network, whereas phosphate glasses are generally based on 3-corner-sharing tetrahedral network, see chapter 3 for further details.

1.1.2 Motivation to establish amorphization criteria

Amorphization is a common response of ceramic materials upon exposure to radiation [6]. Readily amorphizable non-metallic solids are typically more complex ionically-bonded, covalently-bonded or mixed-bonded solids and have been tabulated in Table 1.1, [8]. Several criteria have been used in the available literature to explain the amorphization behavior of ceramics as a response to radiation [8, 6]. These are tabulated in Table 1.2, [8]. Structure-type [9, 10], ionicity [11], melting point [12], homologous crystallization temperature [13] and structural and chemical complexity as measured by number of inequivalent cation site environments and number of atom types respectively [14] have been used as criteria to explain the ease of amorphization of ceramic materials. At best, only limited success has been achieved in applying any one of the above criteria over a large range of structurally very different ceramics [8]. As an example, for disorder induced by ion irradiation, the critical damage energy per target atom, which is often used as a measure of ease of amorphization [15], is shown in Fig. 1-2 in relation to % ionicity in the ceramic. Silicas and a range of abundant silicates can be argued to have upto 50% ionicity character but amorphize almost as easily as Si, would all clearly fall out of place in Fig. 1-2, [8].

1.2 Phosphate Ceramics Used for this Study

In lieu of the large amount of information available for radiation damage of silicas [8], it would be very interesting to study pure phosphorus pentoxide, P_2O_5, with respect to radiation damage. Both these structures are based on corner-sharing tetrahedra,

Table 1.1: Amorphizable solids and their response to corresponding radiation.

Compact Solids	
Cu	none
CuTi	electrons
NaCl	no (radiolysis)
MgO	heavy ions (difficult)
Al_2O_3	heavy ions (high fluence)
$CaTiO_3$	heavy ions (high fluence)
Molecular Solids	
$(\text{-}CH_2\text{-})_n$	electrons (radiolysis)
$C_{14}H_{10}$	electrons (radiolysis)
Network Solids	
SiO_2	electrons (radiolysis)
$NaAlSi_3O_8$	electrons (radiolysis)
Si	light ions (low fluence)
SiC	light ions (low fluence)
Si_3N_4	ions (moderate fluence)
$ZrSiO_2$	ions (moderate fluence)

Table 1.2: Amorphization criteria for irradiated ceramics used in literature.

Atom (ion) size ratios (atom packing)
Ionicity (directed covalent bonds)
Melting Point (bond strength)
Crystallization Temperature (diffusion)
Structural Complexity (# cation sites)
Chemical Complexity (# atom types)

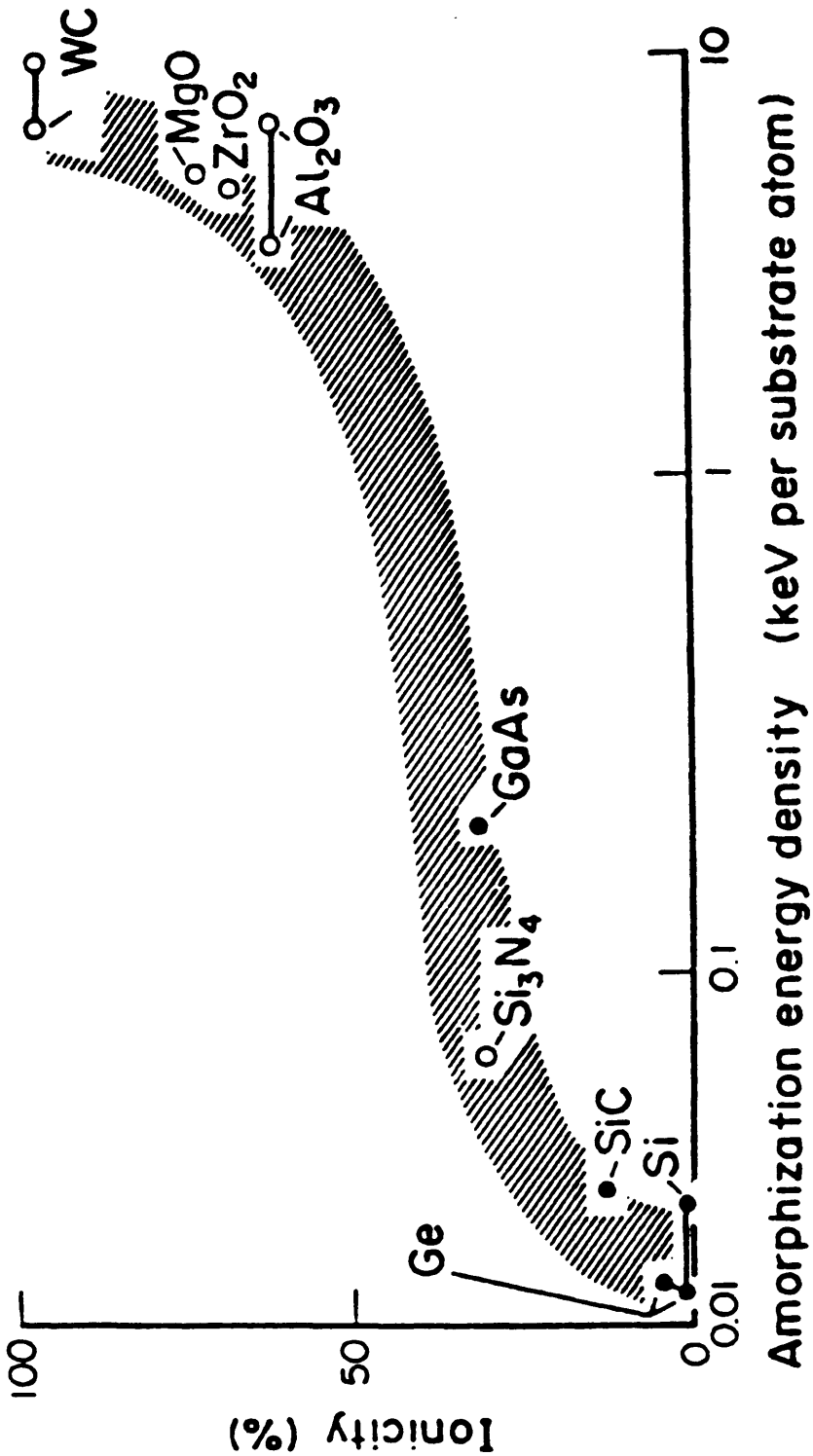

Figure 1-2: Relationship between energy density for amorphization by ion irradiation and ionicity.

$[SiO_4]$ and $[PO_4]$ tetrahedra for silicas and phosphorus pentoxide respectively. The major difference lies in the fact that all four of the corners of the $[SiO_4]$ tetrahedron are shared in a silica network, whereas only three of the four corners of the $[PO_4]$ tetrahedra are shared in a P_2O_5 network (for details, refer to Chapter 3). However, P_2O_5 is one of the most hygroscopic materials, which makes the handling of the samples difficult, to the extent that radiation damage studies of this material in pure form become practically impossible. However, adding lead (II) oxide to P_2O_5 to form lead phosphates produces materials which are chemically stable under ambient conditions. Moreover, lead phosphates have the same three-corner sharing $[PO_4]$ tetrahedral network similar to that in phosphorus penta oxide.

There are three common stoichiometric lead phosphate compounds: lead metaphosphate, $PbO{\cdot}P_2O_5$ (or $Pb(PO_3)_2$), lead pyrophosphate, $2PbO{\cdot}P_2O_5$ (or $Pb_2P_2O_7$) and lead orthophosphate, $3PbO{\cdot}P_2O_5$ (or $Pb_3(PO_4)_2$). Lead pyrophosphate is triclinic, space group $P\bar{1}$ with $a = 0.6941(2)$ nm, $b = 0.6966(2)$ nm, $c = 1.2751(4)$ nm and $\alpha = 96.82°$, $\beta = 91.14°$, and $\gamma = 89.64°$ [16]. Large single crystals of the other two lead phosphates could not be made phase-pure and were not explored in this study. Another class of phosphate ceramics, berlinite or aluminum orthophosphate, $AlPO_4$, was explored. The interesting part of the structure of Berlinite is that its network is based on alternating $[PO_4]$ and $[AlO_4]$ tetrahedra and the structure is isostructural to quartz, [17] with space group $P3_121$-D_3^6, $a = b$ =0.4933nm, c =1.083nm, $\alpha = \beta =$ 90.00°, γ =120.00°.

Diffraction Studies of Phosphate Glasses: To the best knowledge of the author, no electron diffraction data for phosphate glasses and metamict lead phosphates have been reported in literature prior to this study. Also, there are only two studies reported in [18, 19] on phosphate glasses using X-ray diffraction, in which radial distribution functions were generated for lime phosphate ($22CaO{\cdot}78P_2O_5$, $28CaO{\cdot}72P_2O_5$) [18] and for hydrothermally grown amorphous $AlPO_4$ [19]. In this respect, the diffraction studies reported in this work are unique.

Literature Available on Metamict Phosphates: Again, only a very limited literature is available on metamict phosphates. All previously available work was done at Oak Ridge National Laboratory, Oak Ridge, TN, by L. A. Boatner and coworkers [7]. Their work involved the characterization of Pb^{3+} and O^{2+} ion irradiated metamict lead pyrophosphate single crystals and glasses using high-performance liquid chromatography flow injection analysis (HPLC-FIA) which will be discussed in subsequent chapters.

1.3 Objectives of the Present Study

The objectives of this study are summarized as follows:

- Explore radiolysis mechanism of lead pyrophosphate and aluminum orthophosphate single crystals using high resolution transmission electron microscopy (HRTEM).
- Develop and explore electron amorphography for the three component glassy and metamict lead phosphates and study changes in medium-range order of these materials.
- Explore various imaging techniques using electron microscopy to characterize metamict phosphate ceramics.
- Define and establish topological descriptions for phosphate and a wide range of ceramic materials.
- Explore the possibility of topological descriptions to explain the ease of amorphizability of these and analogous network structures and other ceramic materials.

Chapter 2

Experimental Procedures

2.1 Sample Preparation

$Pb_2P_2O_7$ single crystals, and various lead phosphate glasses were prepared by using ultrapure (99.9999%) lead (II) oxide PbO, and ammonium dihydrogen phosphate $(NH_4)H_2PO_4$ as raw materials. The single crystals of $Pb_2P_2O_7$ were prepared by slow cooling of the melt, resulting from a batch of equimolar quantities of the two raw materials in powder form, in a Pt crucible. The batch was first heated at a rate of 100 K/h and held at 775 K for an hour, during which the NH_3 and water produced as a result of decomposition of $(NH_4)H_2PO_4$ were allowed to escape. The batch was further heated at the same rate to 1175 K and held for 10 h to form a low viscosity homogeneous liquid, which was stirred occasionally at 1175 K by shaking the Pt crucible held with a pair of tongs. This liquid was slow cooled at the rate of 1 K/h down to 950 K, and then subsequently cooled to room temperature at the rate of 50 K/h. This resulted in a large chunk of micaceous material, from which large, transparent single crystals could be easily cleaved off. Although fairly large crystals, 18x15x2 mm^3, could be obtained, the average large-sized single crystals obtained were closer to 8x6x0.2 mm^3. X-ray Laue back-reflection measurements confirmed that these were single crystals and that the micaceous facets were perpendicular to the c crystallographic axis. X-ray powder diffraction analysis of the ground single crystals confirmed that they were phase-pure. Refinement yielded the following triclinic crystal param-

eters: $a = 6.961(3)\mathring{A}$, $b = 6.978(5)\mathring{A}$, $c = 12.774(7)\mathring{A}$, $\alpha = 83.11(8)°$, $\beta = 91.14(4)°$ and $\gamma = 90.21(5)°$. Our attempts to grow phase-pure large single crystals of lead ortho- and lead metaphosphate compositions using slow cooling from the melt were not successful. Figure 2-1 shows the PbO-P_2O_5 pseudo-binary phase diagram, and, at least for the orthophosphate composition (line compound), it is clear as to the difficulty involved in trying to grow phase-pure crystals as even slight variations in batching can result in multiple phases. Due to limitations in funding, we did not explore state of the art techniques for single crystal growth such as MBE, laser-assisted growth etc. for the lead ortho- and metaphosphate compositions.

$Pb_2P_2O_7$ glasses were prepared by rapidly quenching the same melt, as in the case for the single crystals, from 1175 K to room temperature between two thick cold copper plates (300 x 250 x 12.5 mm^3) at a quenching rate estimated to be 1000 K/s. The glass was then immediately transferred to a specially designed refractory boat preheated to 650 K (20 K below the T_g of the glass), which in turn was transferred to a separate furnace maintained at this lower temperature. The glass was then annealed at this temperature for an hour and then cooled to room temperature at a rate of 50 K/h. Using this technique, shattering of the glass due to residual stresses arising as a consequence of a high quenching rate was minimized, and large (40 x 30 x 0.3 mm^3), mechanically stable, transparent lead pyrophosphate glasses could be easily prepared.

Lead metaphosphate ($PbO{\cdot}P_2O_5$) glass was prepared by mixing appropriate amounts of powders of lead (II) oxide and ammonium dihydrogen phosphate (of previously mentioned purity levels) and following the same heating schedule as for the lead pyrophosphate glass. However, instead of quenching between two copper plates, the melt was poured in graphite molds preheated to 574 K (again 20 K below T_g) and the mold (with the glass in it), immediately transferred to a separate furnace held at 574 K. The glass was then annealed in a similar fashion as that for the pyrophosphate composition. Glasses whose compositions lay in the range between the lead meta- and pyrophosphate compositions were also prepared by the same technique.

DSC measurements were made for all glasses at a heating rate of 10 K/min on a Seiko DSC 320 H5200 high-temperature thermal analysis system. The glass transition

Table 2.1: Lead phosphate glass compositions and corresponding glass transition temperatures.

Glass Composition	T_g (K)
$1.0PbO.P_2O_5$	594
$1.1PbO.P_2O_5$	598
$1.2PbO.P_2O_5$	600
$1.3PbO.P_2O_5$	602
$1.4PbO.P_2O_5$	616
$2.0PbO.P_2O_5$	670

temperatures for all of the well-annealed glasses were determined and are presented in Table 2.1. None of the glasses displayed multiple glass transition temperatures, and the difference between T_g and the crystallization temperatures was only 50-75 K, virtually ruling out any possibility for phase separation.

Berlinite ($AlPO_4$) single crystals were provided to the author by Prof. R. C. Ewing of University of New Mexico, NM. The samples were originally prepared in France [20] where the samples were grown hydrothermally by reacting phosphoric acid and aluminum sulphate in a solution of sulphuric acid. One large ($100 \times 10 \times 0.1$ mm^3) sample with c-axis perpendicular was supplied, which proved to be more than sufficient to carry out electron irradiation experiments on berlinite.

2.2 Irradiations

The types of radiation used in this study were restricted to fast particle radiations. Energetic fast electrons and ions have been used for irradiating phosphate ceramics and glasses.

2.2.1 Electron Irradiations

Electrons with energies greater than 10 keV are called energetic fast electrons. For the purpose of this study we used 200 keV TEM electrons (wavelength ~2.5 pm),

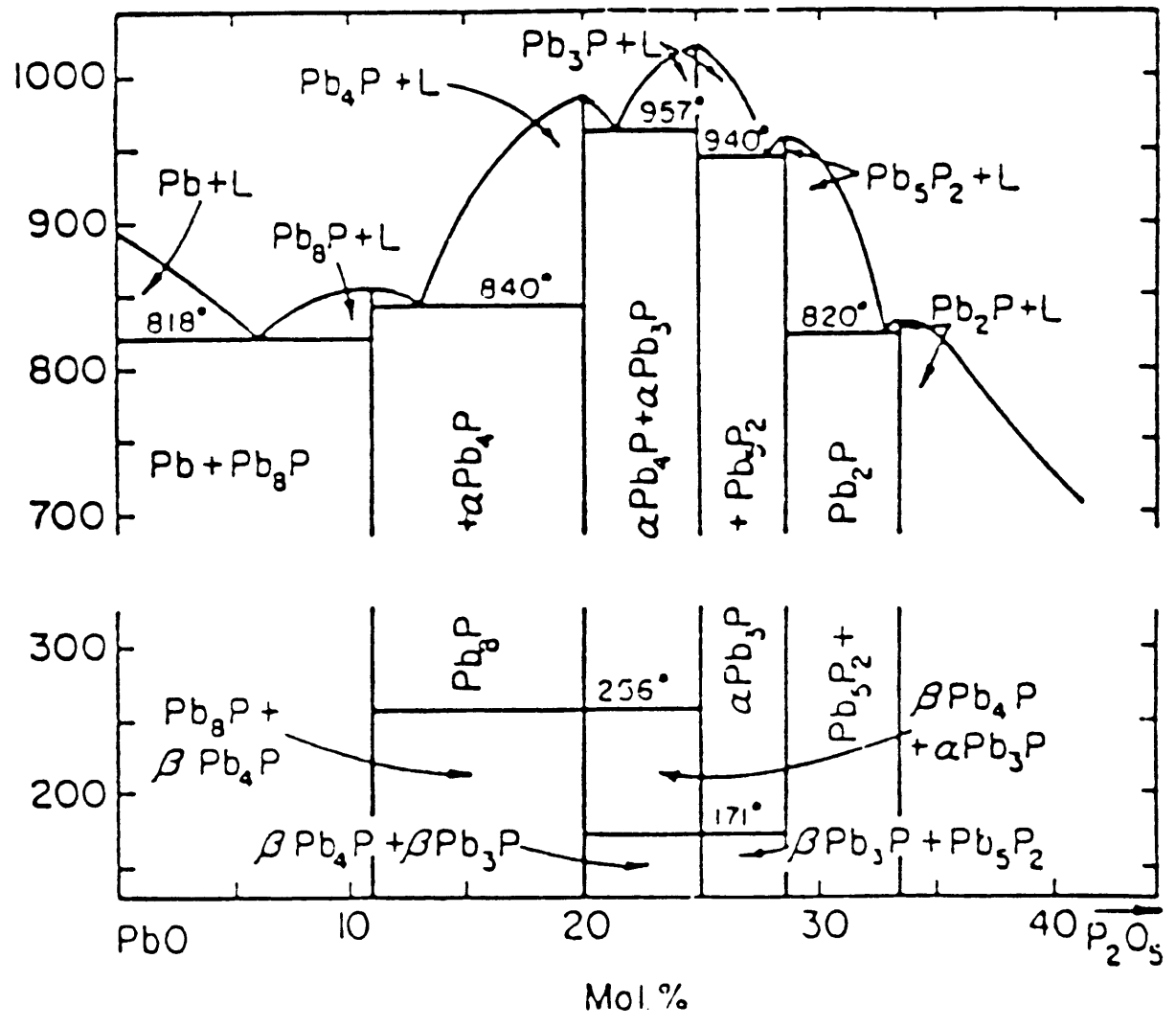

Figure 2-1: PbO-P_2O_5 pseudo-binary phase diagram. P stands for P_2O_5 and Pb for PbO.

that were conveniently available by using Topcon OO2B ultra high resolution 200 kV TEM. The electron irradiation flux was of order $10^{24}e/m^2/s$ with a strongly focused e beam. For lead pyrophosphate single crystals, irradiations were carried out to fluences $> 10^{27}e/m^2$. However, for aluminum orthophosphate, which damages radiolytically very quickly under the e beam, the electron flux was reduced to $\sim 10^{22}e/m^2$, which could still be achieved in the high resolution mode using the OO2B instrument.

2.2.2 Ion Irradiations

Two different types of ion irradiations were used to implant lead phosphate ceramics, *viz*, P^+ and O^+. The P^+ implantations were performed at room temperature using the 300 kV Accelerators Inc. ion-implanter with red-phosphorus powder as the ion source. The accelerating energy for P^+ implantations was 100 kV. This accelerating voltage was so chosen mainly for experimental convenience. At this energy, the maxima of the ion-induced damage profile is at $\sim$75 nm below the surface of the sample, which in turn was determined by using the Monte Carlo TRIM simulation. Also, Sales *et al.* [68] had used O^{++} and Pb^{+++} ions to implant lead pyrophosphate single crystals and glasses where the damage profile maxima was also at 75 nm deep. We implanted P^+ into these two materials, and in addition also into lead metaphosphate glass, over a very wide ion fluence range of $10^{15}/m^2$ - $2\times10^{20}/m^2$.

We collaborated with Drs. Ning Yu and Michael Nastassi of LANL to conduct O^+ implantations, mainly because the Accelerators Inc. ion-implanter at M.I.T. was withdrawn from service. The O^+ implantations were carried out at 55 kV accelerating voltage, at liquid nitrogen temperature, the accelerating energy again chosen to locate the maxima of the damage profile at 75 nm depth. Lead pyrophosphate single crystals, lead pyrophosphate glass and lead meta phosphate glass were irradiated with O^+ ions to a wide fluence range of $10^{16}/m^2$ - $10^{21}/m^2$.

For ion irradiations, the lead pyrophosphate single crystals were prepared as dis-

cussed in section 2.1. The micaceous single crystals were then polished to an optical finish by using 0.06 μm γ-Al_2O_3 and a non-aqueous polishing media (Buehler polishing oil). The well-annealed lead pyro- and metaphosphate glasses were sectioned to roughly the same size as the single crystals, and also polished similarly up to an optical finish. During ion irradiations, the crystalline samples were tilted at an angle of 7° , to the c axis, which is the conventional way of minimizing the effect of ion channeling; the glass samples were also similarly tilted for consistency.

For electron irradiations, minor modification was required to make a TEM specimen from polished single-crystal lead pyrophosphate, mainly because those materials were very fragile and micaceous. Because the TEM sample holders require the samples to be 3mm diameter, crystals slightly smaller than 3×3 mm were cut out and mounted on molybdenum single-hole grids (3 mm OD and 1mm ID) with epoxy and then further thinned down, dimpled and ion-milled to electron transparency.

In order to characterize the ion-irradiated samples by electron microscopy (HRTEM and STEM), cross-section TEM (XTEM) samples of the lead phosphates were prepared. The ion-irradiation-induced metamict layer was found to be of order 200 nm (see Chap. 4). For the case of the metamict lead pyrophosphate and the metamict lead metaphosphates, two ion-irradiated specimens were sandwiched and glued together by electron-beam-resistant epoxy. This sandwiched layer was then cut and ground to size so that it could fit in a thin-walled steel tube of 3 mm OD. The remaining volume of the steel tube was filled by two appropriately-sized Ta rod halves, and the whole assembly glued together by a hard epoxy. The tube (with the metamict sample sandwich and the Ta rod halves) was then sliced to thin sections and polished to an optical finish using 6, 3, 1 and 0.25 μm diamond paste. These XTEM samples were then dimpled and ion-milled. The XTEM samples of ion-irradiated metamict lead pyrophosphate single crystals were prepared in a similar fashion; however, extra care was taken at each thinning and cutting step to minimize the induced stresses. This turned out to be most critical, as the preparation of cross section samples of

very easily-cleavable micaceous crystals was very difficult.

2.3 Characterization Techniques

2.3.1 High Resolution Electron Microscopy

Imaging thin samples by transmission electron microscopy has come a long way since the first lattice images of crystalline copper- and platinum-pthalocyanine which resolved 1.2 nm spacing [21]. The development of the HRTEM technique has mainly resulted from a significant advancement in technological improvement of the instrumentation, both the electron optics and the recording technique, for example, the availability of recording data digitally through a powerful computer, making dynamic experiments practicable. Cowley [22] was first to point out the difficulties in correlating HRTEM images to crystal structures. The technique of high resolution electron microscopy is a very well established technique for over two decades now and the author chooses not to discuss it, an enthusiastic reader may refer to the books by Spence [23] and by Buseck, Cowley and Eyring [24].

Instrumentaion

High resolution electron microscopy was performed with a Topcon OO2B HRTEM operating at 200 kV and with a spatial resolution of 0.18nm. Electron irradiations were performed to fluences ranging from 10^{22}-$10^{24} e/\mathrm{m}^2\mathrm{s}$, depending upon the specimen being irradiated. The wide fluence range available was very useful, in particular, for looking at berlinite samples. The spherical aberration coefficient was 0.4mm. The focusing spread caused, by chromatic aberrations, was taken as 5 nm in image simulations. The electron beam divergence (twice the semi-divergence angle) was estimated to be about 1 mrad.

2.3.2 HRTEM Image Processing

Image processing generally deals with the enhancement in contrast of the HRTEM image, the restoration of certain parts of the image, and finally the interpretation of the image.

The image wave functions are determined by the coupling of the electron waves exiting the specimen and the contrast transfer function imposed on the electron wave caused by imperfections of the imaging system.

In order to obtain digital diffractograms, the HRTEM images were first digitized using a CCD camera with a 1024×1024 pixel resolution coupled to an image grabber 486 personal computer and using the HRTEM negative film in the transmission mode. This digital image was then transfered to a Silicon Graphics Personal IRIS 4D/35 workstation which was loaded with the software SEMPER VI to compute the power spectra from these digitized images. The corresponding power spectra of HRTEM images contain information of the spatial frequency distribution present in corresponding images. When the HRTEM image appears fully crystalline, the corresponding power spectrum shows very sharp Fourier peaks, which is an indication of discrete distribution of spatial frequencies in the original image; a uniform background indicates that the content of irregular noise in the background to be minimal [25]. However, when the crystalline image begins to degrade, it is apparent in the calculated power spectrum of the image where the higher order Fourier peaks fade in intensity and a diffuse background appears as background signal. This fading of the corresponding Bragg reflections in the electron diffraction pattern can be qualitatively understood by a simple two-cell model [26] as described below.

The average structure factor $< F(\mathbf{g},t) >$ can be expressed in terms of the contribution from the undamaged perfectly crystalline structure with structure factor $F^{(0)}(\mathbf{g})$ and the completely amorphized structure with an average structure factor $F^{(d)}(\mathbf{g},t)$

$$< F(\mathbf{g},t) >= n(t)F^{(0)}(\mathbf{g}) + [1 - n(t)]F^{(d)}(\mathbf{g},t), \tag{2.1}$$

in which $n(t)$ is the undamaged fraction as a function of time t.

The fading of the intensity of a Bragg reflection is represented by the intensity ratio

$$\frac{I(\mathbf{g},t)}{I^{(0)}(\mathbf{g})} = n^2(t) + [1-n(t)]^2 b^2 + 2n(t)[1-n(t)]b, \tag{2.2}$$

where

$$b = \frac{F^{(d)}(\mathbf{g},t)}{F^{(0)}(\mathbf{g})} \tag{2.3}$$

However, it must be noted that the corresponding power spectrum for an amorphous image gives only the instrument's contrast transfer function (CTF) [27].

2.3.3 Energy-Filtered Electron Diffraction

History and Overview

Diffraction techniques using X-ray, neutron or electron radiation are powerful methods in structure determination of materials. For crystalline materials, the systematic correlation of the atom positions due to the long-range spatial periodicity of the structure give rise to discrete sharp diffraction peaks located at the reciprocal space lattice points. However, for aperiodic topologically-disordered non-crystalline materials, the only correlation of atom positions present is due to the interatomic bonds of closely prescribed lengths which gives a modulation of the diffracted intensities with a period roughly proportional to the reciprocal of bond lengths. The diffraction patterns appear as diffuse halos superimposed on a uniform background.

X-ray, neutron and electron diffraction have also been employed as powerful characterization techniques for the structural studies of noncrystalline material [28]-[34]. With electron diffraction, the very strong interaction with matter makes possible the analysis of very small volumes with acceptable statistics. As a rule of thumb, about 0.1 μm^3 of material is needed to get good electron diffraction data from noncrystalline material, which is about 6 orders of magnitude less than that required for X-ray diffraction and about 12 orders less than that for neutron diffraction. This means that the information obtained by the later two diffraction techniques is averaged over much larger volumes of sample material.

In diffraction experiments, the signal that contains structural information is always superimposed upon the noise, which reduces the quality of the signals collected, and often some technique is used to enhance the signal-to-noise ratio. For electron diffraction patterns from noncrystalline materials, the major sources that contribute to the background noise are energy fluctuations that arise from the energy distribution of the electron source and inelastic scattering events occurring as electrons pass through the sample material. This is not a problem (generally) for crystalline materials because the Bragg diffraction peaks are positioned at a discrete set of positions and the signal to noise ratio can be greatly enhanced by using spatial filtering techniques which are common in image processing. However, with a noncrystalline material, there are no discrete Bragg peaks present in the diffraction pattern, and spatial filtering becomes practically impossible.

Energy-filtering of the electron diffraction patterns from noncrystalline materials is essential for two major reasons: (a) Electron diffraction patterns contain both elastically and inelastically scattered electrons; the inelastically scattered electrons contribute to a continuous background arising from various scattering mechanisms superimposed on the elastic peaks that contain information of the atom correlations. If not energy-filtered this background will render certain peaks (elastic) difficult to recognize. (b) There are many different scattering mechanisms with various scattering cross-sections contributing to the inelastic background, such as plasmon excitation, core and valence electron excitations, and electron-phonon scattering; these processes are not yet as well-understood as the elastic scattering process, scattering theories and are not yet well enough established to quantify the inelastic background or to relate the inelastic intensity distribution to specimen structures in an analytical fashion.

By elastic scattering we mean that the state of the atom is undisturbed due to the scattering process. Although, in general, the collision between an electron and an atom is a many-body problem, to a very good approximation it can be treated as a scattering problem in which the incident electron wave is scattered by the potential field of the atom [35]. In particular, it is most tractable in the so called fast-electron regime, where the incident electron possess kinetic energies between 10 keV and 10

MeV, typically encountered in electron microscopy experiments.

Transmission electron diffraction has long but infrequently been employed to investigate structures of noncrystalline material. Although energy-filtering has long been used to study the energy losses for spectroscopic analysis, it has not been as widely applied for diffraction studies. In an attempt to improve the resolution of their scanning electron diffraction instrument [36]-[38], Grigson and his colleagues installed an electrostatic energy filter [39], and the structure of amorphous Ge films deposited onto carbon substrates was investigated [40]. Graczyk and Moss [41] at M.I.T. built a similar scanning unit and installed it in a transmission electron microscope. With such an instrument, studies were made on the structures of amorphous silicon [42], vapor-deposited and ion-implanted thin films of amorphous germanium [43] and glow-discharge amorphous silicon [44]. More recently, the technique has been reinvestigated by Cockayne and McKenzie [45] and their colleagues. With the use of modern energy-loss spectrometers, they have studied both polycrystalline [46] and amorphous materials, such as hydrogenated amorphous silicon-carbon alloy [47], boron- and phosphorus-doped hydrogenated amorphous silicon [48] and BN [49].

Theory

Selected-area electron diffraction patterns (SAEDPs) from the partially metamict states

The amplitude of a scattered electron wave from a sample is

$$A(\mathbf{q}) = \sum_{j}^{N} f_j \exp(-2\pi i \mathbf{q} \cdot \mathbf{r}_j) \ , \tag{2.4}$$

where f_j is the atomic scattering amplitude for the atom positioned at $\mathbf{r}_j$, N is the total number of scattering atoms, and q is the scattering vector defined by

$$q = \frac{2\sin(\Theta/2)}{\lambda} \ , \tag{2.5}$$

with Θ and λ being the scattering angle and the electron wavelength, respectively.

If the material consists of two portions, one crystalline, and one metamict with an aperiodic atomic arrangement, the amplitude (2.4) can be decomposed into two parts,

$$A(\mathbf{q}) = A_a(\mathbf{q}) + A_c(\mathbf{q}) \ , \tag{2.6}$$

where

$$A_a(\mathbf{q}) = \sum_j^{N_a} f_j \exp(-2\pi i \mathbf{q} \cdot \mathbf{r}_j) \ , \tag{2.7}$$

in which the summation is done over the metamict region which contains N_a atoms, and

$$A_c(\mathbf{q}) = N_c F_c(\mathbf{q}) \ , \tag{2.8}$$

where F_c is the structure factor for the crystal divided by the number of atoms in the unit cell, and N_c is the number of atoms contained in the crystalline portion. The total scattering intensity is hence

$$\begin{aligned} I(\mathbf{q}) &= |A(\mathbf{q})|^2 \\ &= |A_a|^2 + |A_c|^2 + A_a^* A_c + A_a A_c^* \ . \end{aligned} \tag{2.9}$$

Taking an ensemble average over all orientations, we arrive at the Debye equation [51]

$$|A_a|^2 = \sum_j \sum_k f_i f_j \frac{\sin(2\pi q r_{ij})}{2\pi q r_{ij}} \ , \tag{2.10}$$

for the aperiodic part, where r_{ij} is the interatomic distance between atoms i and j; while

$$|A_c|^2 = N_c^2 |F_c|^2 \ , \tag{2.11}$$

for the crystalline part, and the cross terms

$$A_a^* A_c + A_a A_c^* = 2 \sum_k^{N_c} f_k \sin(2\pi \mathbf{q} \cdot \mathbf{r}_k) \sum_j^{N_a} f_j \frac{\sin(2\pi q r_j)}{2\pi q r_j} \tag{2.12}$$

are in fact relatively small compared with the first two terms which account for the independent scattering intensity from the crystalline and metamict portions, respec-

tively. Neglecting these cross terms, we therefore have

$$I(\vec{q}) = \sum_{i}^{N_a} \sum_{j}^{N_a} \frac{\sin(2\pi q r_{ij})}{2\pi q r_{ij}} + N_c^2 |F_c(\vec{q})|^2 \ . \tag{2.13}$$

Defining the unit intensity functions

$$I_a(q) = \frac{1}{N_a^2} \sum_{i}^{N_a} \sum_{j}^{N_a} \frac{\sin(2\pi q r_{ij})}{2\pi q r_{ij}} \ , \tag{2.14}$$

and

$$I_c(\mathbf{q}) = |F_c(\mathbf{q})|^2 \ , \tag{2.15}$$

the electron intensity then measured is proportional to

$$I(\mathbf{q}) = p^2 I_a(q) + (1-p)^2 I_c(\mathbf{q}) \ , \tag{2.16}$$

where p is the atomic fraction of the metamict portion.

The Bragg reflection intensity degrades as the proportion of the metamict region grows. The intensity ratio of the degradation is

$$\frac{I(\mathbf{q})}{I_c(\mathbf{q})} = p^2 \frac{I_a(q)}{I_c(\mathbf{q})} + (1-p)^2 \ , \tag{2.17}$$

in which $I_a(q)$ gives rise to the diffuse halo rings, and $I_c(\mathbf{q})$ has non-zero values only at the non-extinction reciprocal lattice points.

In general the intensity ratio I_a/I_c is a decreasing function as the scattering angle increases.

Electron diffraction RDFs of amorphous materials

For a system of N atoms in total with n types of atoms, where N_α atoms belong to type α, the partial atomic density functions are defined by

$$\rho_{\alpha\beta}(\mathbf{r}) = \frac{1}{N_\alpha} \sum_{j=1}^{N_\alpha} \sum_{k=1}^{N_\beta} \delta[\mathbf{r} - (\mathbf{r}_{\alpha j} - \mathbf{r}_{\beta k})] - \delta_{\alpha\beta}\delta(\mathbf{r}) \ , \tag{2.18}$$

where $\alpha, \beta = 1, 2, ..., n$. For a chemically homogeneous system, the atomic density

function $\rho_{\alpha\beta}$ gives the atomic distribution of β atoms with respect to an arbitrarily chosen α atom.

For systems with a random distribution of atoms, we can take an ensemble average over all orientations in both real and Fourier space. This will lead to the following equations in terms of the density functions $\rho_{\alpha\beta}(r)$, which are related by Fourier transform to the partial structure factors $S_{\alpha\beta}(q)$:

$$< r(\rho_{\alpha\beta}(r) - \bar{\rho}_\beta) >= 2\int_0^\infty qS_{\alpha\beta}(q)\sin(2\pi qr)dq \ , \tag{2.19}$$

where $\bar{\rho}_\beta$ is the average number density of atoms of type β. The partial structure factors are expressible in terms of the experimentally obtainable quantities by

$$i(q) = \sum_{\alpha=1}^{n}\sum_{\beta=1}^{n} c_\alpha c_\beta f_\alpha f_\beta S_{\alpha\beta} \ , \tag{2.20}$$

where $i(q)$ is the reduced intensity

$$i(q) = \frac{I(q) - I(0)\delta_{q0}}{N} - \sum_{\alpha=1}^{n} c_\alpha f_\alpha^2 \ , \tag{2.21}$$

in which c_α is the atomic fraction for atoms of type α:

$$c_\alpha = \frac{N_\alpha}{N} \ , \tag{2.22}$$

and $I(q)$ is the elastic scattering intensity which can be experimentally measured.

Since $c_\alpha\rho_{\alpha\beta} = c_\beta\rho_{\beta\alpha}$, with the introduction of the weighted partial structure factors

$$S'_{\alpha\beta} = \frac{1}{2}(c_\alpha S_{\alpha\beta} + c_\beta S_{\beta\alpha}) \ , \tag{2.23}$$

the number of unknown partial structure factors can therefore be reduced to $n(n+1)/2$, and the partial RDFs can be obtained by the following equation

$$< c_\alpha r(\rho_{\alpha\beta}(r) - \bar{\rho}_\beta) > \ = \ < c_\beta r(\rho_{\beta\alpha}(r) - \bar{\rho}_\alpha) >$$

$$= 2\int_0^\infty qS'_{\alpha\beta}(q)\sin(2\pi qr)dq \ . \qquad (2.24)$$

The above equations are applicable to any multiple component system.

For the ternary lead phosphate system, we used a reduced structure factor modified from a reduced intensity with a sharpening function $\bar{f}(q)$. The modified RDF is obtained by

$$r(\rho_e(r) - \bar{\rho}_e) = 2\int_0^\infty qS(q)\sin(2\pi qr)M(q)dq \ , \qquad (2.25)$$

where $M(q)$ is the modification function to account for the termination effect, and $S(q)$ is the dimensionless reduced structure factor

$$S(q) = \frac{I(q) - I(0)\delta_{q0}}{N_{uc}\bar{f}^2} - \frac{1}{\bar{f}^2}\sum_{uc} f_j^2 \ , \qquad (2.26)$$

in which uc refers to a molecular unit.

In the present study, the sharpening function used was

$$\bar{f} = 2f_1 + 2f_2 + 7f_3 \ , \qquad (2.27)$$

and the Lorch modification function [50]

$$M(q) = \frac{\sin(\pi q/q_{max})}{\pi q/q_{max}} \ , \qquad (2.28)$$

was used, where the subscripts 1, 2 and 3 refer to Pb, P and O atoms respectively (note that $\bar{f}$ is for the lead pyrophosphate composition) and q_{max} is the maximum value of q measured experimentally.

The RDFs deduced from experimental intensity data were in the form of a convolution involving the partial RDFs as given in equation (2.25), with a sharpening function $\bar{f}(q)$. In the convolution, the window functions are determined by the atomic

scattering amplitudes f_j and the sharpening function $\bar{f}$

$$w_{ij}(r) = 2\int_0^\infty \frac{f_i(q)f_j(q)}{[\bar{f}(q)]^2}\cos(2\pi qr)M(q)dq\ , \tag{2.29}$$

which are essentially governed by the ratio $f_i f_j/\bar{f}^2$. An ideal case should be such that this ratio is close to a constant value, which will result in the effect that the final RDF is a linear combination of the partial RDFs as discussed below.

An alternative method to interpret the X-ray RDFs is to invoke the Warren approximation. In this approximation [52] it is assumed that

$$f_j = K_j\bar{f} \tag{2.30}$$

where $\bar{f}$ is an optimized function that makes K_j be a constant for each element.

Using this approximation, the reduced structure factor $S(q)$ in equation (2.26)

$$S(q) = \frac{I(q) - I(0)\delta_{q0}}{N_{uc}\bar{f}^2} - \frac{1}{\bar{f}^2}\sum_{uc} f_j^2 \tag{2.31}$$

can be decomposed into a linear combination of two reduced partial structure factors $S_j(q)$ as

$$S(q) = \sum_{uc} K_j S_j(q) \tag{2.32}$$

where

$$\begin{cases} S_1(q) &= K_1S_{11}(q) + K_2S_{12}(q) + K_3S_{13}(q) \\ S_2(q) &= K_1S_{21}(q) + K_2S_{22}(q) + K_3S_{23}(q) \\ S_2(q) &= K_1S_{31}(q) + K_2S_{32}(q) + K_3S_{33}(q)\ . \end{cases} \tag{2.33}$$

Equivalently, these will induce the real space density functions to be

$$\rho(r) - \bar{\rho} = \sum_{uc} K_j[\rho'_j(r) - \bar{\rho'}_j] \tag{2.34}$$

and

$$\begin{cases} \rho'_1(r) - \bar{\rho}'_1 &= K_1[\rho_{11}(r) - \bar{\rho}_1] + K_2[\rho_{12}(r) - \bar{\rho}_2] + K_3[\rho_{13}(r) - \bar{\rho}_3] \\ \rho'_2(r) - \bar{\rho}'_2 &= K_1[\rho_{21}(r) - \bar{\rho}_1] + K_2[\rho_{22}(r) - \bar{\rho}_2] + K_3[\rho_{23}(r) - \bar{\rho}_3] \\ \rho'_3(r) - \bar{\rho}'_3 &= K_1[\rho_{31}(r) - \bar{\rho}_1] + K_2[\rho_{32}(r) - \bar{\rho}_2] + K_3[\rho_{33}(r) - \bar{\rho}_3] \ , \end{cases} \tag{2.35}$$

and the reconstructed RDF would be thus given by

$$G(r) = 4\pi r^2 \sum_{uc} K_j \ [\rho'_j(r) - \bar{\rho}'_j] \tag{2.36}$$

We should note that, the Warren approximation does not make any approximation in the process of data reduction to obtain the convoluted RDFs, but it is an approximation that tries to simplify the interpretation and understanding of the deduced RDFs.

Instrumentaion

Energy-filtered electron diffraction data were collected in a VG HB5 scanning transmission electron microscope (STEM) equipped with a serial energy-loss spectrometer and operating at an accelerating voltage of 100 kV. Fig 2-2 shows the schematic diagram of the selected-area diffraction mode, which was used to collect the zero-loss energy-filtered electron diffraction data. In the selected area mode, a nearly parallel electron beam is incident onto the thin portion of the sample, and the beam scans across a range of incident angle, while the electron intensity is collected at the spectrometer. The typical energy window used, determined by the width of the slit of the spectrometer, was < 2 eV.

A selected area aperture of 30μm in diameter (and in some cases a 10μm) was used to limit recorded patterns to a small area on the specimen. A collector aperture of 70μm determined the angular resolution of the diffraction patterns at 7×10^{-5} radians. The small size of the electron probe is important in our experiments, as this can reduce the illuminated area to a minimum while maintaining quite parallel illumination. This avoids unwanted exposure of unwanted portions of the sample to

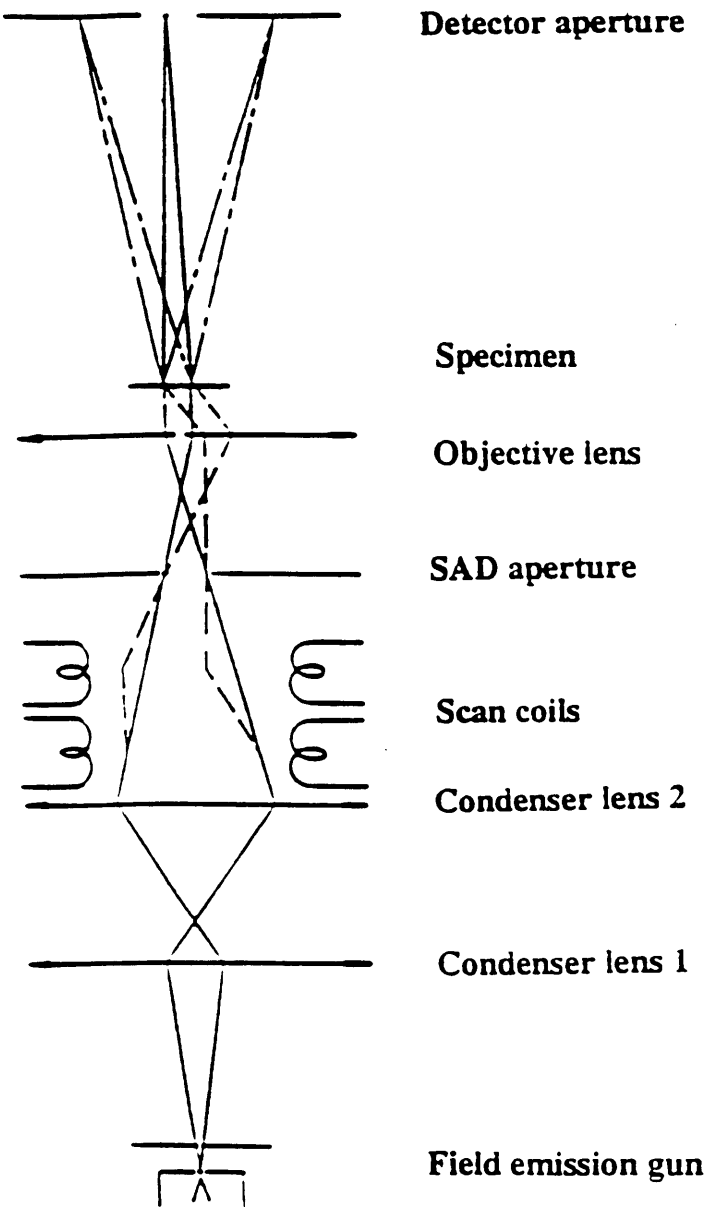

Figure 2-2: Schematic representation of the selected-area diffraction mode in the VG HB5 STEM.

the electron beam.

For all the ion-irradiation-induced metamict samples, only a portion of the metamict layer (in cross-section TEM samples) was exposed to the electron beam, by using the SAD aperture. Though this reduced the total amount of the sample contributing scattered electrons, it nevertheless avoided collecting data from the pristine (unirradiated) portion of the sample, which again is important to our experiments. Another important precaution taken in collecting EFED data from all of the ion-irradiation-induced metamict samples was to calibrate camera length each time. For the metamict lead pyrophosphate single crystals, the camera length was easily calibrated by collecting diffraction data (Bragg spots) from neighboring crystalline material in the same cross-section TEM sample. However, for metamict glasses, a thin layer of Ag was deposited, and the Bragg spots from Ag were used to calibrate the camera length.

2.3.4 High Performance Liquid Chromatography

Hisory and Overview

The earliest scientific account of separation using liquid chromatography was reported by Tswett [53] in 1903. His experiments involved separation of green plant pigments in a vertical column filled with powdered chalk. The next significant advance came in 1941, for which Martin and Synge [54]-[57] were awarded Nobel prize for their work on liquid partition chromatography. Moore and Stien [56] in 1948 developed ion-exchange chromatography for the separation of amino acids. It was not until the mid 1960's that liquid chromatography technique became a powerful chemical analytical tool. Until then, the accuracy was limited to only 5% detectable resolution in terms of reproducibility. PC (paper chromatography), TLC (thin layer chromatography) and DCC (dry column chromatography) were equally effective in separation of mixtures of chemical substances in liquid phase. The availability of specialized chromatographic column packings, sensitive on-line detection and monitoring systems, solvent (mobile phase) elution at high pressures (not just gravity-driven), and automation of the process has led to the subsequent development of high-performance liquid chro-

matography (HPLC), with the chemical analytical resolution well exceeding 1 ppb in many cases. Other common acronyms used instead of HPLC are HSLC (high speed liquid chromatography), HELC (high efficiency liquid chromatography), HPLC (high pressure liquid chromatography); but amongst all these, HPLC or high performance liquid chromatography is the most common usage.

Common Modes of Liquid Chromatography (LC)

There are four common modes of liquid chromatography, namely, liquid-liquid (partition) chromatography (LLC), liquid-solid (adsorption) chromatography (LSC), ion-exchange chromatography and exclusion chromatography. Each of these are briefly described in the following.

LLC, the most versatile mode of LC, was originally developed by Martin and Synge [54]-[57] and is good for any kind of solvent, polar or non-polar. Both the phases (stationary and mobile) are liquid. As an example, Martin and Synge separated acetylated amino acids with water as a stationary phase (on silica gel) with chloroform as a mobile phase. The liquid stationary phase is coats to a finely divided inert phase (silica gel), usually in a column (separation column). The sample to be analyzed is dispersed in the mobile phase, and its components are partitioned between the stationary and mobile phases according to their partition coefficients $K_1, K_2, \cdots K_n$. This partitioning leads to a differential rate of migration, and separation occurs.

LSC uses the principle of adsorption (again, difference in rates among the chemical species) and is usually a reversible process making use of the chemical equilibrium between adsorbent, solvent and solute.

Ion-exchange chromatography works on the principle of substitution of one ionic species for another. An example of anion exchange is given by

$$R^+Y^- + X^- \rightleftharpoons R^+X^- + Y^- \tag{2.37}$$

where R^+ can be a solid stationary phase, Y^- a liquid mobile phase and X^- the

sample. One or both of the reaction products can be detected by several available kinds of on-line spectroscopes attached to the LC, depending upon the properties (usually optical absorption) of the species to be detected.

In exclusion chromatography, also known as gel permeation or gel filteration chromatography, the solid stationary phases are usually xerogels, aerogels or cross-linked polymers. The sample goes through the pores of the solid stationary phase, and higher molecular weight moities are separated from the lower ones and detected by an on-line detector system.

The advantages of the HPLC technique over other chromatographic techniques are manifold, some of which have been listed below:

- HPLC columns can be used several times without regeneration.
- Ultra high resolution (better than 1 ppb) can be readily achieved.
- Reproducibility and quantification of chemical analysis for liquid phase separation far exceeds those with any other known technique.
- Shorter analysis time than other techniques.
- Besides low temperature operation, there are two competing phases (mobile and stationary) in HPLC compared to one phase (stationary) in gas chromatography (GC), giving much better control of the separation, and often separations impossible using GC are fairly trivial using HPLC.

Application to Phosphate Ceramics

The underlying principle for the use of HPLC to phosphate ceramics lies in the dissolution of metal phosphates in aqueous solution which occurs by a simple process where the phosphate chain and rings present in the ceramic are 'peeled off' as a result of hydration, but without polymerization. According to Van Wazer, phosphate chains from a solid phosphate never polymerize [58]. This principle allows one to characterize the chain length distribution in all of phosphate ceramics, *viz*, crystals,

glasses and metamict phosphates. However, liquid chromatography techniques cannot be applied to any other glass systems, because the network constituents readily polymerize in aqueous state, and attempts to do so for silicate and borosilicate glasses have not been wholly successful [59].

Liquid chromatography was first exploited in the early 1950's through the mid 1960's to study the structure of alkali-phosphate/alkaline-earth-phosphate glasses [60]-[62]. In these earlier studies, however, paper chromatography was used to analyze the structural content (phosphate polymerization) present in these phosphate glasses dissolved in an aqueous solution. Despite copious information obtained from these early studies, extended applications of the technique were perhaps not pursued further owing to the rather time-consuming paper chromatographic experiments and because the phosphate chains were resolved only up to a chain length of 6 [PO_4] tetrahedra [63]. It has also been suggested [63] that the ignorance of the physical scientists who study glass structure towards wet-chemical analytical techniques (liquid chromatography, for example) is responsible for neglect of this very powerful technique to analyze phosphate ceramics until recently.

More recently, with the introduction of a flow injection analysis system to detect orthophosphates [67], Brazel *elal.* [65] have further improved the technique of liquid chromatography for application to phosphates by improving the resolution of the chromatograms by several orders of magnitude. Phosphate chains as long as 18 [PO_4] tetrahedra and also 3- and 4-membered ring phosphates could be detected [65]. As an example, Fig. 2-3 shows the phosphate chain length distribution for lead metaphosphate glass [63]. Chains of [PO_4] tetrahedra from P_1 to P_{12} are shown clearly resolved in the chromatogram, along with two cyclic (ring) phosphate ions, trimetaphosphate, P_{3m}, and the tetrametaphosphate, P_{4m}. The broad envelope in the chromatogram appearing after 40 min of chromatographic separations are likely from chains much longer than 12 [PO_4] tetrahedra. This is a reasonable surmise because, in practice, in preparing glasses with compositions near the metaphosphate composition, the average chain length is typically around (and limited to) 40 [PO_4] tetrahedra due to incorporation of water in these glasses, the hydrogen ions acting as

cross-linking cations [64].

Sales *et al.* [63] extended this work to lead-iron phosphate glasses, looking at the degree of phosphate chain length distribution, and concluded that the average chain length of the lead-iron phosphate glasses decreases with increasing iron content. This conclusion is intuitive, because the addition of iron increases cross-linking between linear phosphate chains which will bring down the average chain length. In addition, structural studies of phosphate chain polymerization after Pb^{3+} ions implantation into lead pyrophosphate single crystals and lead pyrophosphate glasses were also performed [68]. Sales *et al.* [68] concluded that the structure of lead pyrophosphate glass is different from the ion-irradiated lead pyrophosphate single crystals and ion-irradiated lead pyrophosphate glass.

Instrumentation

The high-performance liquid chromatography flow injection analysis (HPLC-FIA) system used for this study comprised a dedicated facility at Sales' Boatner's group at Oak Ridge National Laboratory (ORNL), Oak Ridge, TN. The system was developed by Brazell and coworkers [65] in 1984 was adapted by Sales and Boatner for analysis of lead phosphate ceramics. The HPLC-FIA system at ORNL is briefly described as follows:

Reagents: The reagents used in the flow injection system for the determination of phosphates was a 5:1 mixture of 5×10^{-3} M ammonium molybdate, $(NH_4)_6Mo_7O_{24}{\cdot}4H_2O$, in 1.8 M H_2SO_4 and 0.05 M *L*-ascorbic acid containing 5% (v/v) acetone. The ascorbic acid partially reduces Mo(VI) to Mo(V). The Mo(VI)-Mo(V) complex combines with orthophosphate to form the heteropyroblue complex [66]. All chemicals were reagent grade and were used as received.

Sampling: Except for the large facet of the single crystal (perpendicular to *c*-axis), which was ion-irradiated, all the other five unirradiated faces of the sample were coated with Ag paint prior to dissolution of the metamict layer. For ion-irradiated glasses also, all the other faces except the ion-irradiated one were masked with Ag paint. The implanted, masked samples were then placed in 1-3 cm^3 solution of 0.22

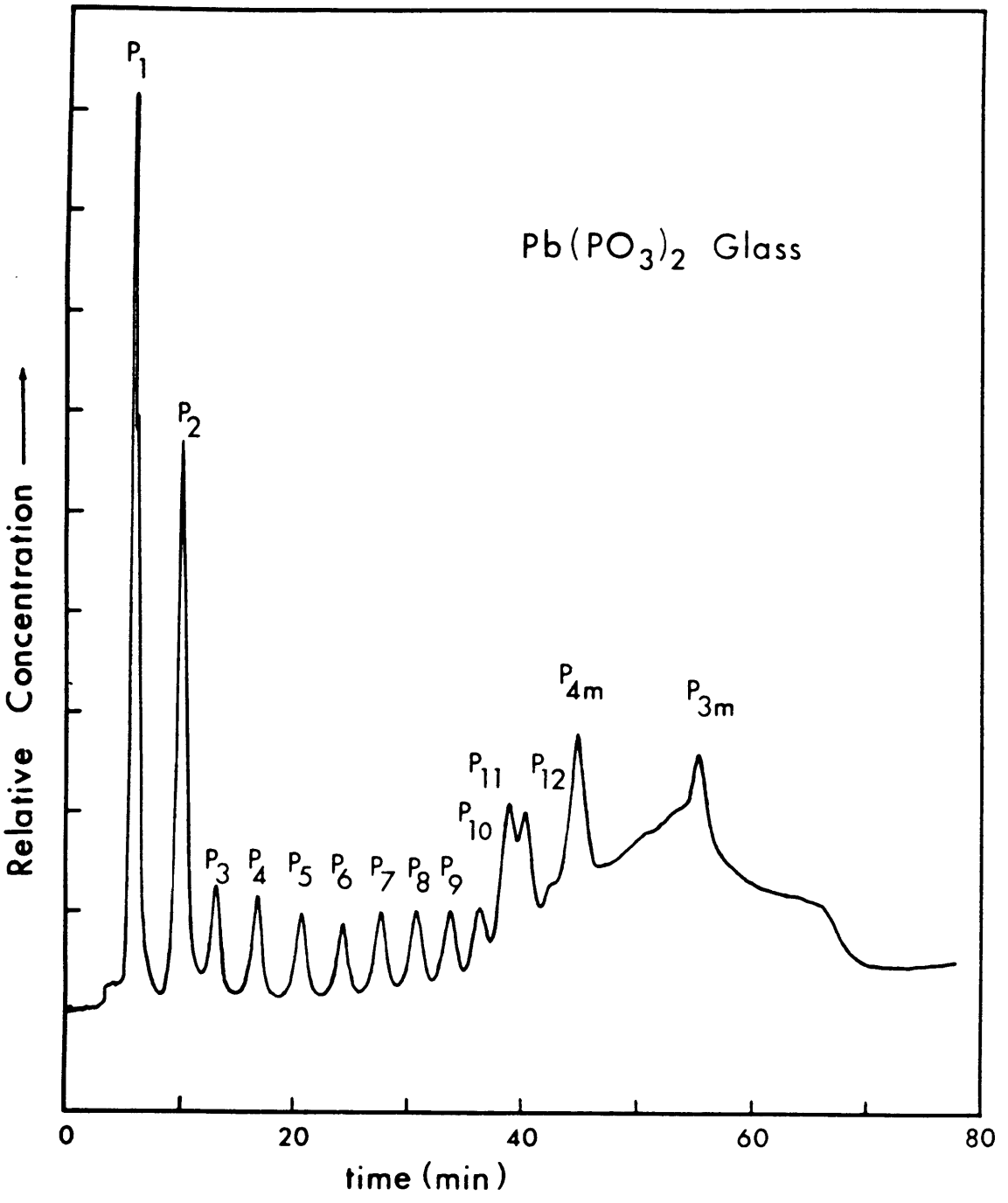

Figure 2-3: Liquid chromatogram of lead metaphosphate glass. P_{3m} and P_{4m} represent 3- and 4-membered rings. The broad envelope visible in the chromatogram after 40 min is representative of much longer chains which remain unresolved.

M NaCl and 5×10^{-3} M Na_4EDTA and were soaked until the amount of phosphorus in solution corresponded to the loss of a surface layer from the sample of about 100 nm; EDTA stands for ethylene diamine tetra-acetic acid. The process of dissolution/soaking normally took 15-30 min, but the exact time was determined for each sample separately. The chelating agent, Na_4EDTA, complexed with the Pb cations released from dissolving solid, ensuring that these cations did not interact with the phosphate anions in the solution. The solution containing the metamict lead phosphates in the aqueous state was then used as a sample for chromatographic separation.

Flow Injection Analyzer: The flow injection system adapted by the Oak Ridge group was based on the system developed by Hirai and coworkers [67]. An Eldex Model E-120-S pump (Eldex, Menlo Park, CA) delivers the molybdenum reagent at a flow rate of 0.5 ml/min. Samples for total phosphate analysis were introduced into the reagent stream with a Rheodyne Model 7125 six-port injection valve equipped with a 20 μl sampling loop. The sample and the reagent react in a 10 m PTFE coil heated to 140°C. This coil was wrapped around a 150 mm long $\times$ 50 mm OD glass tube which was then wrapped with electric heating coil. The temperature was controlled with a Barber Coleman Model 520 solid-state controller. The reacted sample passed through a 1 m long coil cooled by chilled water before flowing through an Altex Model 153 UV detector (volume 8 μl, path 10 mm). Absorption of the phosphate complex was measured at 660 nm wavelength. A 10 m backpressure coil attached to the exit of the detector prevented bubble formation caused by heating the reaction coil, thus avoiding anomalous responses.

Chromatographic Separations: A Spectra Physics 8700 solvent delivery system was used for programming and delivering the solvent at a constant flow rate of 1 ml/min through the analytical column. Samples were injected with a Rheodyne Model 7125 six-port injection valve equipped with a 50 μl sampling loop onto a Vdac SC anion guard column (40 mm long $\times$ 4 mm ID; Varian, Palo Alto, CA). The polyphosphates were separated on an Animex A-27 8% cross-linked quarternary ammonium anion exchange column (300 mm long $\times$ 4 mm ID; Bio-Rad, Richmond, CA) using NaCl

solutions containing 5 mM of Na_4EDTA. A linear gradient from 0.28 M to 0.53 M NaCl over a 40 min time interval was used, and the final eluent concentration was held constant for additional 15 min. The effluent from the analytical column was introduced directly into the stream of reagent used for FIA. Fig. 2-4 is a schematic representation of the HPLC-FIA system used.

HPLC-FIA System: The analytical system described could be used for either the rapid 'batch' analysis of total phosphate or as a detector for individual phosphate species following their chromatographic separation. The polyphosphates are hydrolyzed in the reaction coil by acidic reagent at elevated temperature to orthophosphate, which then condenses with Mo(V)-Mo(VI) to form the colored complex. To obtain optimum response, the hydrolysis must be complete. The system was optimized using various standards, including several crystalline phosphate compounds with unique chain length (i.e. unique state of phosphate polymerization) [68]. The system was optimized by analyzing various standards at different reactor coil temperatures, and the optimal operating reactor coil temperature was determined to be 140°C [65].

The maximum absorption of the complex using the conditions described above was found to be at 820 nm wavelength, but rather than modifying the entire detector system, experiments were made at 660 nm with very satisfactory sensitivity, and the linear response range was from 1.5 to 105 ppm. The relative standard deviation for replicate injections was less than 1%, and the determinations for total phosphate content could be made at the rate of 25 samples per hour.

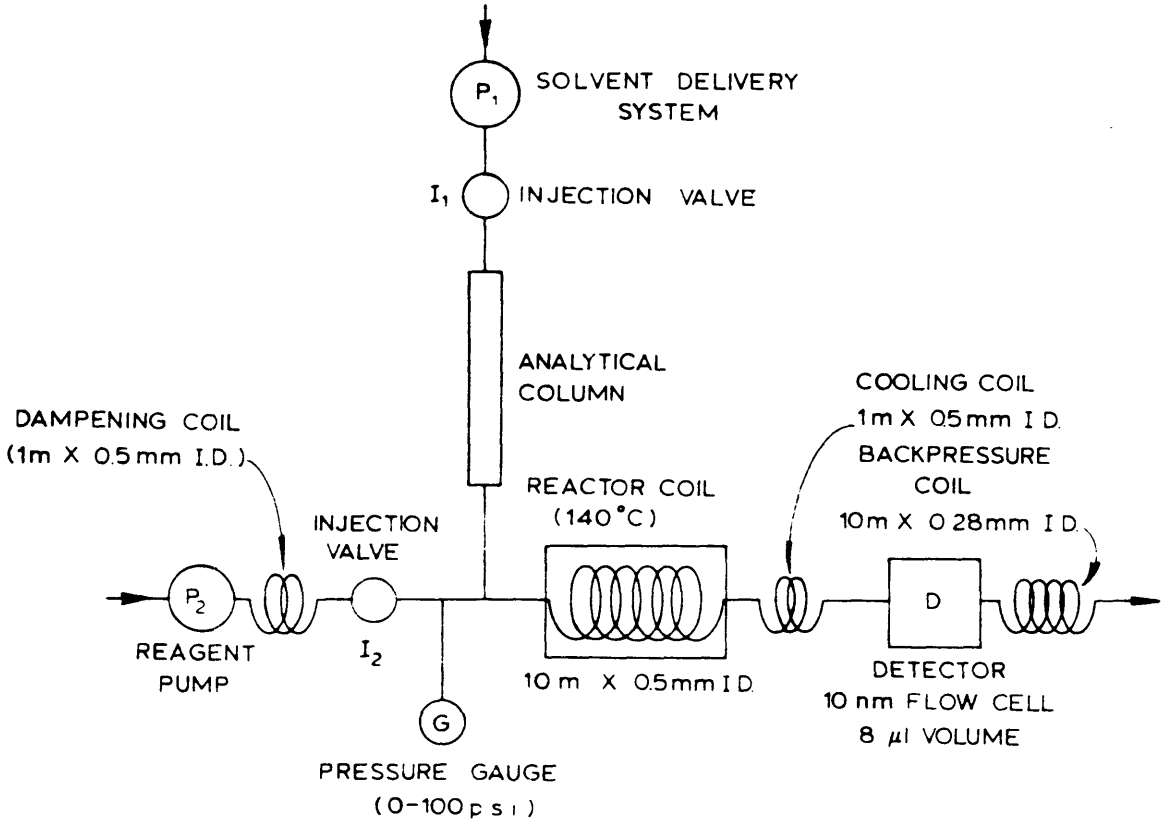

Figure 2-4: Schematic diagram of the HPLC-FIA system.

Chapter 3

Topology and Structural Freedom

3.1 Introduction

Topology is formally defined as the study of properties of geometric objects which are invariant under transformations that are continuous and with continuous inverses [69]. With reference to structure in solids, topological considerations deal with the way the structure is connected together and the way the connections govern the possibility of alternative structural arrangements. The assessment is based on connectivity and goes back more than a century to the method of 'constraint counting' introduced by Maxwell [70] to investigate the rigidity of mechanical structures. It is shown in this chapter that structural freedom to adopt alternative arrangements is a function of the connectivity of the structure.

Topology has been extensively used to explain the aperiodic nature of diffraction-amorphous solids, and several approaches have been proposed in the literature. Zachariasen [71] was first to suggest that the glass-forming ability of a system is related to its ability to form an "extended three-dimensional network lacking periodicity with an energy content comparable with that of the corresponding crystal network." An energy content comparable to that of the corresponding crystal ensures a low probability of crystal nucleation, because amorphization after all represents failure of crystallization. Zachariasen proposed that nonmetallic inorganic glasses are made up

of the same coordination polyhedra which exist in the corresponding crystals, primarily determined by the fact that comparable energy configurations must yield the same "short-range" structure, such that these polyhedra are linked together at the vertices and that the number of polyhedra sharing a vertex is also the same as in the corresponding crystal. However, unlike in crystals, the relative orientations between these vertex-sharing polyhedra "vary within rather wide limits", which is primarily responsible for the absence of long range order in these materials. Zachariasen's two dimensional schematic of an oxide glass structure shown in Fig 3-1 is probably the most frequently reproduced schematic in the glass literature. In the following section, these principles will be discussed with respect to topology and structural freedom.

3.2 Topological Descriptions of Network Structures

Topological descriptions of network structures have been widely varying and numerous, but they all fall into only a few major categories, *viz*, space-filling tessellations in real and 'hyper' space, rings and their neighbors, and connectivity. Tessellation literally means tiling of a space or, in practical terms, the filling of the space with tiles (which have the same dimensions as the space) such that none of the tiles overlap and that intersection of two such tiles must contain a face or that of three such tiles an edge. In two dimensions, the tiles of a tessellation are planar, whereas in three dimensions they are generalized polyhedra.

Our knowledge of space-filling tessellations (Euclidian space in particular) is still limited by the Euler formula [72, 73]:

$$N_0 - N_1 + N_2 - N_3 + \cdots + (-1)^{n-1} N_{n-1} = 1 - (-1)^n \tag{3.1}$$

where N_n denotes the the number of n dimensional entities, for example in a three

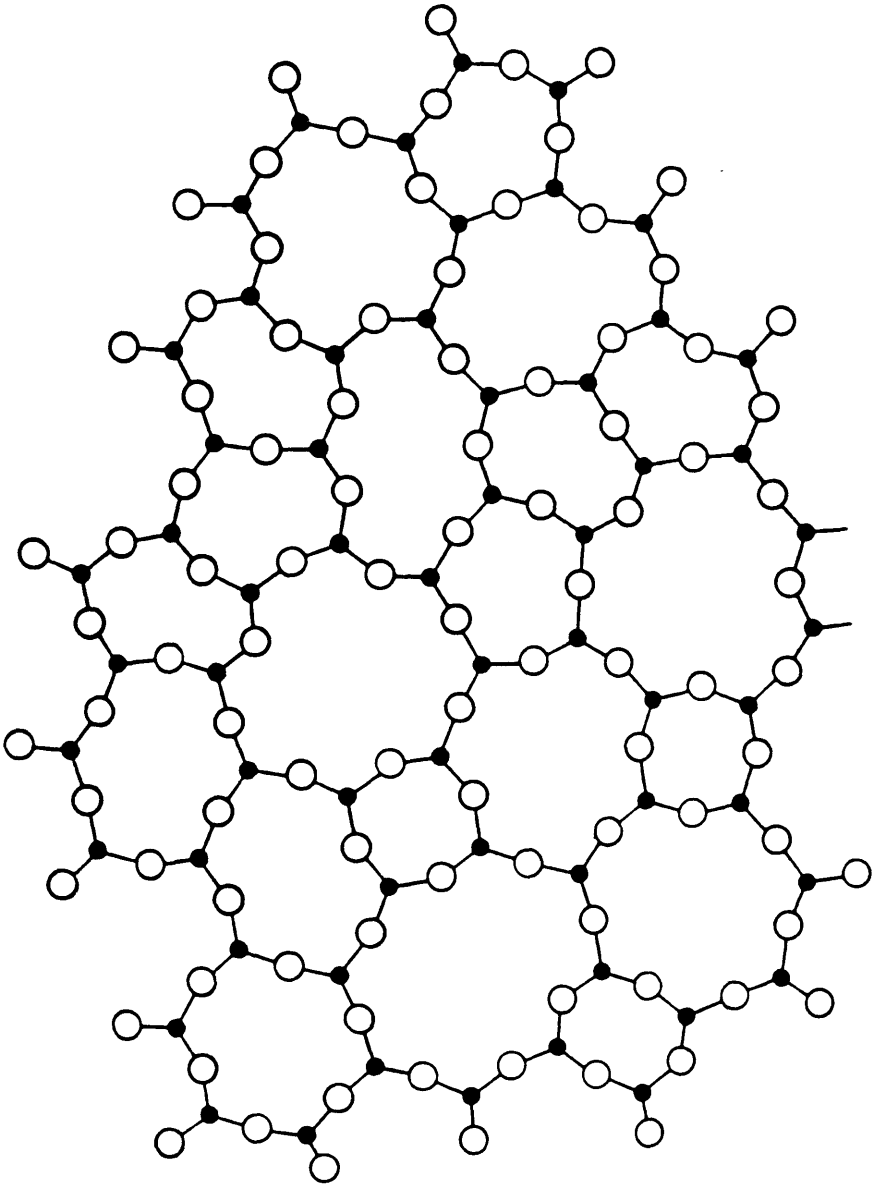

Figure 3-1: Zachariasen's schematic of an $AO_{3/2}$ glass in two dimensions.

dimensional packing, $N_0 = \sum_n V_n$, V_n the number of vertices of coordination n,

$N_1 = E$, the number of edges,

$N_2 = \sum_p F_p$, the number of faces with p sides, and

$N_3 = N$, the number of polyhedra.

Therefore in three dimensions, the equation 3.1 reduces to

$$\sum_n V_n - E + \sum_p F_p - N = 1 \tag{3.2}$$

The validity of this result becomes evident with a few simple but instructive examples shown in Fig. 3-2 and Fig. 3-3.

Equation 3.1 yields for Fig. 3-2:

(a) 3 - 3 + 1 - 1 = 0

(b) 4 - 4 + 1 - 1 = 0

(c) 4 - 6 + 4 - 1 = 1

(d) 6 - 12 + 8 - 1 = 1

(e) 8 - 12 + 6 - 1 = 1

Equation 3.1 yields for Fig. 3-3:

(a) 7 - 12 + 8 - 2 = 1

(b) 6 - 11 + 8 - 2 = 1

(c) 5 - 8 + 6 - 2 = 1

Rivier [74] explains the *disorder* in amorphous solids by rotational dislocation-type defects, called disclinations. Disclination lines in a continuous random network (CRN) are imaginary lines that go through the CRN which is made up of a structure with ions (atoms) as vertices, bonds as edges and rings as faces, see Fig. 3-4 and Fig 3-5. Rivier has established that the odd-numbered rings of atoms in a CRN constitute line defects, in that they are all threaded through by imaginary lines which end only on the surface of the material or form closed loops, or in simple terms, are located

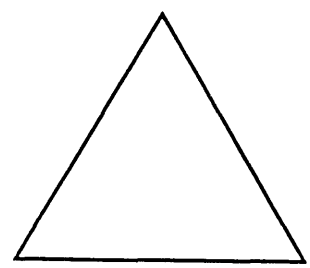

(a) = 0

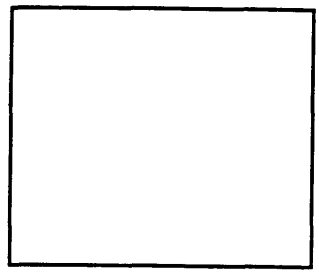

(b) = 0

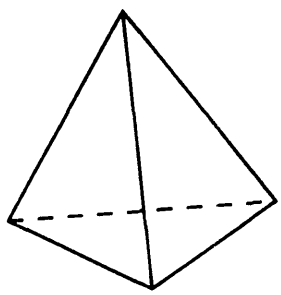

(c) = 1

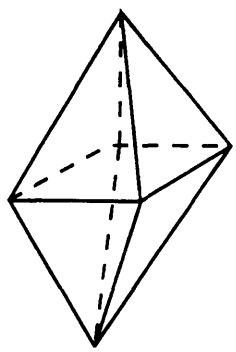

(d) = 1

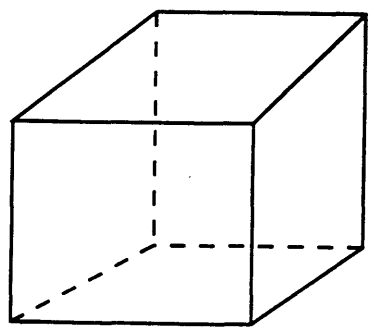

(e) = 1

Figure 3-2: Partition space-filling in two dimensions with a triangle (a) and a square (b) and in three dimensions with a tetrahedron (c), an octahedron (d) and a cube (e).

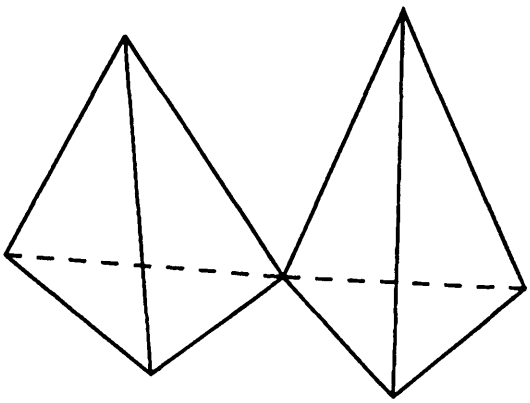

(a) Corner-Sharing

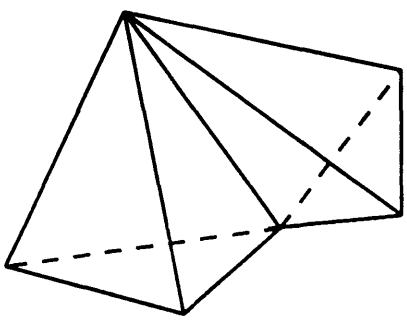

(b) Edge-Sharing

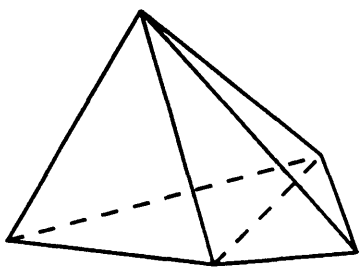

(c) Face-Sharing

Figure 3-3: Partition space-filling in three dimensions in case of polyhedra connectivity with a tetrahedron as an example using (a) corner-sharing (b) edge-sharing and (c) face-sharing.

along closed lines which cross them but do not cross even-numbered rings. These disclination lines are illustrated in Fig. 3-4. Rivier [74] also extended the work of Toulouse [75, 76] and showed that the existence of line defects associated with disclinations is consistent with the absence of rotational symmetry in the material. He also classifies the disclination lines as elements of the homotopy group $\pi_1(E_3) = Z_2$, where the Euclidian group E_3, is also the manifold of internal states of an amorphous solid and Z_2 the abelian group of order two. The use of homotopy groups in physics is beyond the scope of this thesis but the interested reader may consult reference [75].

Kleman and Sadoc [77] suggested that the structure of an amorphous material could be represented as a crystal in some ideal, curved space, projected into Rivier's [74] Euclidian space. Their idea gives a direct geometrical interpretation of a compromise between the requirements of best possible local packing of atoms and (Euclidian) space-filling [78, 79, 80]. In simpler terms, consider a tetrahedron (present in most amorphous materials with 'spherical' ions at their vertices). One can start filling space by connecting these tetrahedra, defined by a propagation, and observe the curvature of the space. If one considers a structure where the local interactions are invariant (say, no change in chemical composition or no decomposition takes place), the curvature must be constant and consequently the underlying space can be spherical, hyperbolic or eventually Euclidian. Locally, it is not a problem of space filling, but on a global scale difficulty arises on account of the impossibility of filling Euclidian space with regular tetrahedra. However, if the space is given curvature, then it can be filled, or in other words, space filling can be achieved if a network of defects is introduced. On a two-dimensional flat surface full tessellation is achieved only if the polygons have an angle which is a submultiple of 2π, a regular pentagon, with a dihedral angle of 72°, leaves a gap as shown in Fig. 3-6 but can tile a two-dimensional surface with a constant positive curvature, in this case a three-dimensional sphere ('hyper' space for a two-dimensional polygon), resulting in a dodecahedron. This is illustrated for three dimensions in Fig. 3-7. Five tetrahedra can share a common edge, but a void necessarily remains between the two triangular faces. This is due

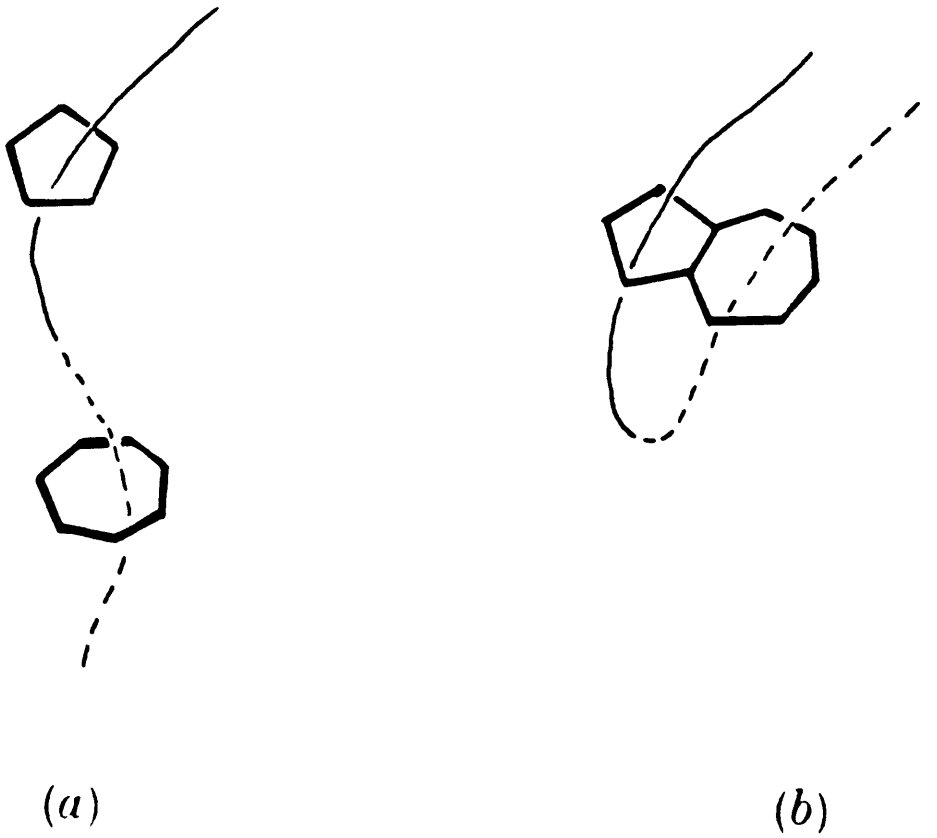

Figure 3-4: Disclination line in a continuous random network. (a)The full (dotted) line threads through five- (seven-) fold rings and imparts a positive (negative) local curvature to the network. (b) configuration of minimum elastic energy for disclination line (a).

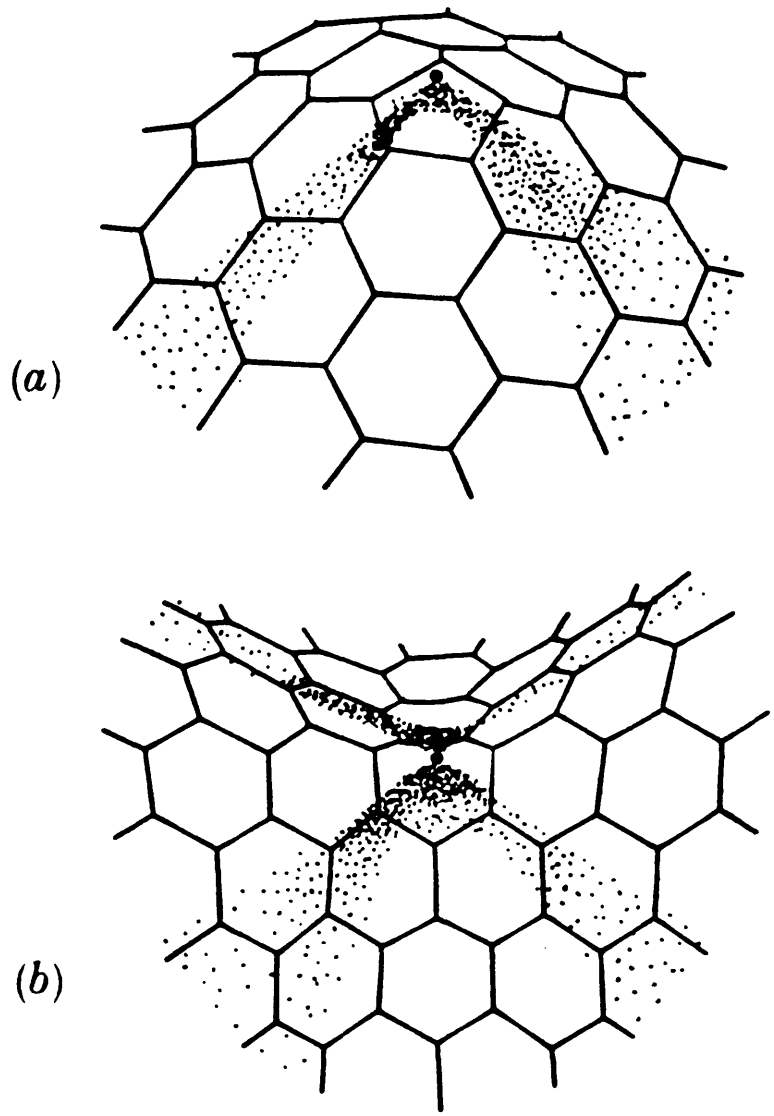

Figure 3-5: Disclination, curvature and ring parity: a two-dimensional example on the hexagonal lattice. (a) Positive curvature associated with the removal of a wedge material. A five-fold ring is created around a disclination point defect. (b) Negative curvature (saddle point) associated with the addition of material and the creation of a seven-fold ring.

to the fact that the tetrahedron dihedral angle ($\sim 70°$) is not a submultiple of 2π. This misfit angle manifests itself when one tries to propagate the tetrahedral local configuration and completely surround a given vertex. An imperfect icosahedron is then obtained. In order to define an ideal model in which space can be perfectly filled by tetrahedra, Sadoc [78]-[80] defined an 'S3' spherical (hypersphere) space in which the 'ideal' polytope (hypersphere) can be embedded in the four-dimensional Euclidian space with the equation:

$$X_1^2 + X_2^2 + X_3^2 + X_4^2 = R^2 \tag{3.3}$$

S3 being a 3D (curved) manifold, only three of the four coordinates are independent in the above equation. In terms of tetrahedron edge length, the radius of curvature is R = $(1 + \sqrt{5})/2$. This 'perfect' (ideal) tetrahedral arrangement is the analogue of a polyhedron in a higher dimension.

The concept of space-filling with connected structural units has long been known (e.g. Fedorow [81]); however, the more familiar tessellations associated with space-filling are Bernal holes [82, 83]. Although this approach has been most applied to liquids and metallic glasses, the concept is easily illustrated by overlapping such 'holes' onto Zachariasen's famous two-dimensional glass structure drawing, Fig. 3-8. Finney [72] (and references therein) describes such a result as an assembly of as Voronoi polyhedral cells (or 'Dirichlet region'), which has advantages over the simple tetrahedral net; for example, there is only one polyhedron associated with each center (property of Voronoi polyhedron). More recently, Ashby [84] showed that if a shell formed by close packing of spheres (ions) is too small to contain another sphere, then the number of distinguishable polyhedra is limited to eight and forms a canonical holes set. The difficulty with such tessellations in applying to network glasses (not so compact structures) is that they are not able to convey information on the atomic correlations in these glasses which have highly directional covalent bonding or mixed (covalent and ionic) bonding.

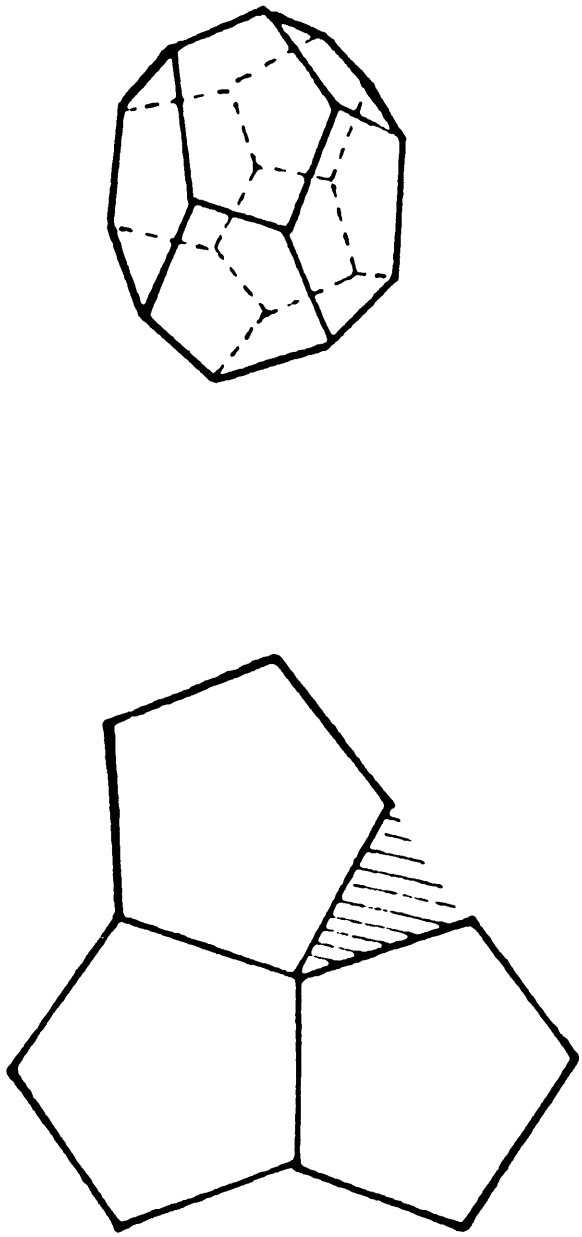

Figure 3-6: Regular pentagons do not tile a plane, but can in three dimensions as shown (top) by a sphere tiled with pentagons: the dodecahedron.

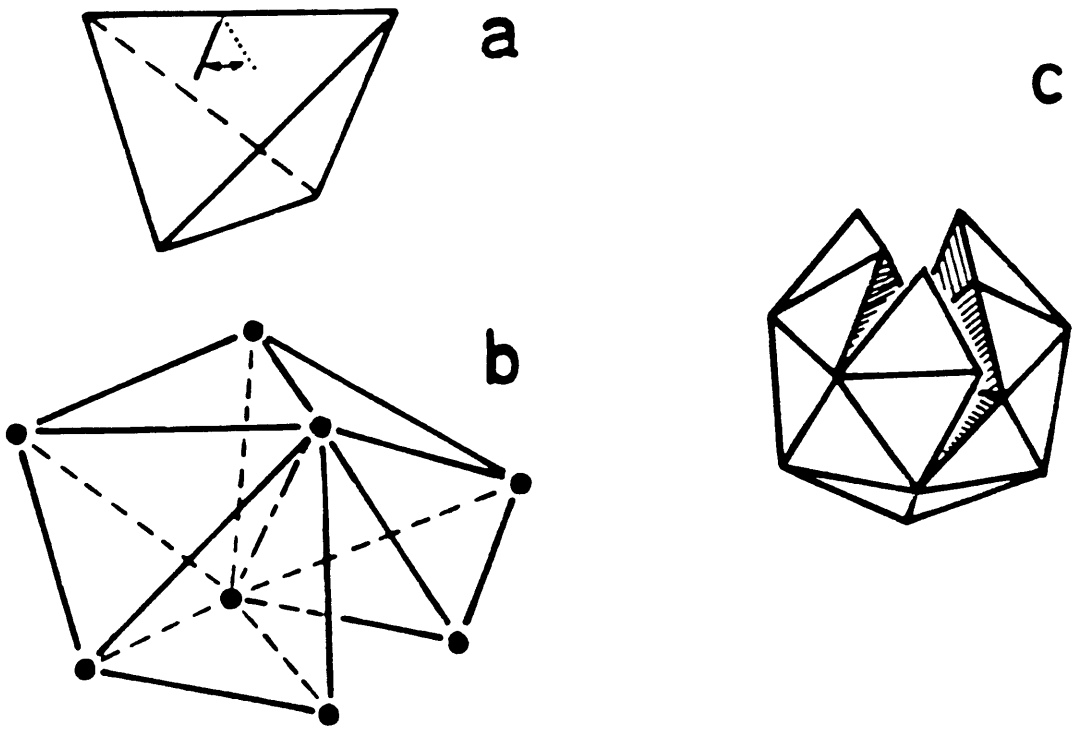

Figure 3-7: The dihedral angle of a tetrahedron (a) is not a submultiple of 2π. Five tetrahedra with a common edge leave a small unfilled space (b). An imperfect icosahedron (c) with a misfit between dashed faces.

One other topological description of network structures, as mentioned before, is by cataloging at rings and network (tetrahedral) neighbors in a random network structure. Returning back to Zachariasen's representation, we can represent an Si-O polygon by triangles in two dimensions (polyhedra as tetrahedra in three dimensions) and look at the rings formed by the edges of these triangles. This approach was initiated by Shackelford [85]-[88]. One such configuration is shown in Fig. 3-9. Shackelford demonstrated the evidence for a lognormal distribution of interstitial sizes in vitreous silica. He also demonstrated that while for pure silica glass the ring statistics are conveniently characterized by a log-normal probability distribution function, for a sodium silicate glass the ring statistics are driven away from the simple log-normal distribution [87]. However, the problem with modeling such 'interstices' is in the arbitrariness in the atomic correlation assignments in that almost all network glasses will involve some coordination polyhedra, and such unique assignments are not possible. One other problem that is apparent is that the rings are different with interstitial voids. They appear same only in two dimensions.

Another topological language (not tessellating, but very useful) for studying network structures is proposed by Marians and Hobbs [89]-[94]. Their topological approach is based on a one-dimensional characterization of tetrahedral networks which they used to uniquely quantify crystalline polymorphs of silica and their reconstructive phase transformations. For example, they proved that a transformation between cristobalite and quartz does not occur because it would involve creation or elimination of six tetrahedra. They uniquely characterized the crystalline silica polymorphs and at least generally the glass by defining a set of *primitive rings* (and *local cluster*) that pass through the tetrahedron of interest. A ring is a *primitive ring* if it cannot be decomposed into two or more smaller rings without any overlap. In other words, for a ring to be *primitive*, the (network) path distance between any two vertices must be equal to the lesser of the lengths of the two paths along the ring which connects the two vertices. This definition of a *primitive ring* is always computable in a non-

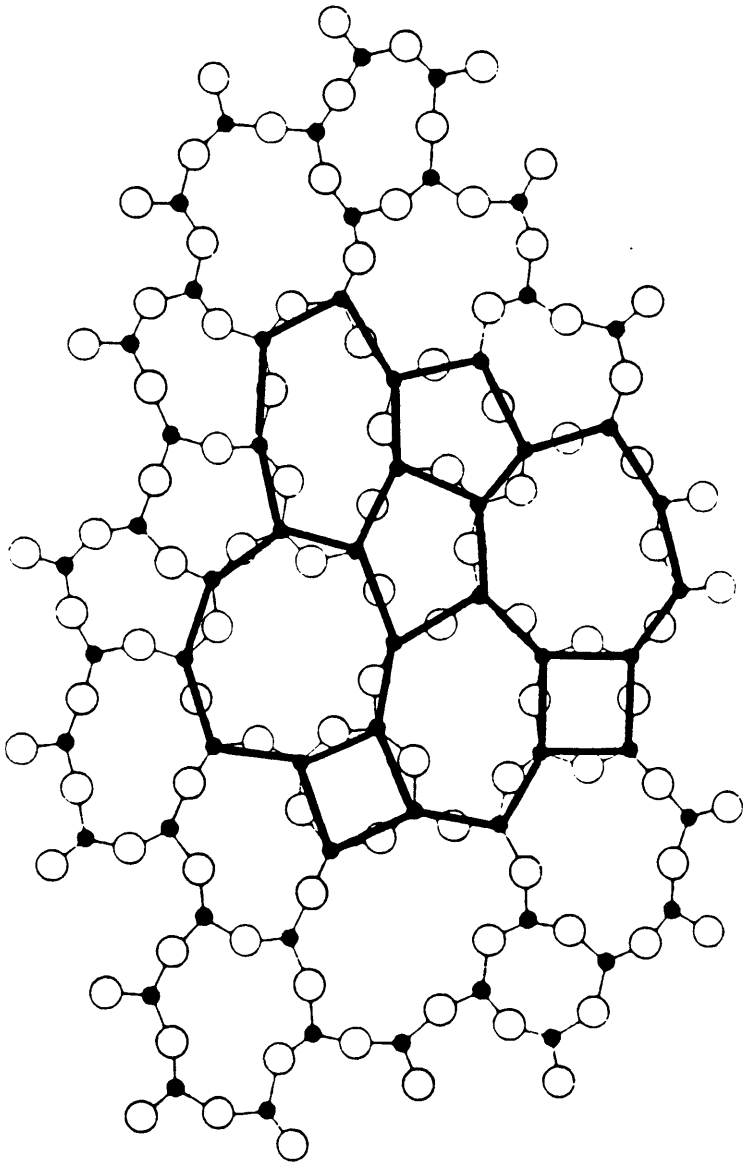

Figure 3-8: 'Bernal' holes and voids as seen in a Zachariasen glass.

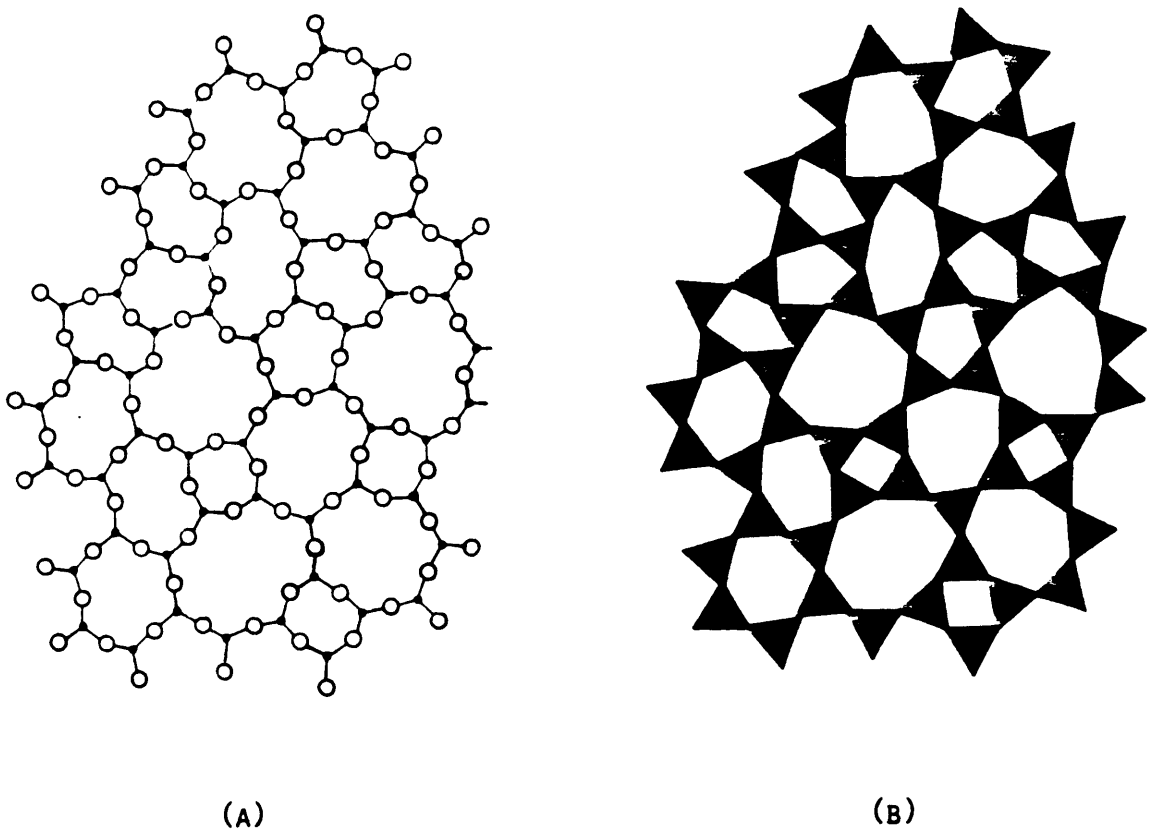

Figure 3-9: (a) Zachariasen's glass (b) An array of triangles displaying rings formed by the triangle edges. (One other configuration of rings can be generated by connecting the centers of these triangles.)

ambiguous fashion and is the basis of finding and defining *primitive rings* in a network structure. As an example, Fig. 3-10 shows a non-primitive 8-ring: (7,6,4,3,10,9,8). The reason that this ring is non-primitive is that the distance between vertices 3 and 7 is three (path (3,2,1,7)) and both paths between those two vertices along the ring ((7,6,5,4,3) and (7,8,9,10,3)) have length four.

The *local cluster* of a tetrahedron in a network contains all the *primitive rings* (and their tetrahedra) that pass through that tetrahedron. The rings of this local cluster comprise a subnetwork. A *local cluster* is absolutely finite and entirely descriptive of each of the polymorphs of silica. Marians and Hobbs also showed that larger *primitive ring* sizes yield higher density values, which at a first glance is counter intuitive. *Primitive ring* and *local cluster* statistics were also used to characterize lower density silicas (gels etc.) and also surfaces. A detailed description of their approach is beyond the scope of this thesis; however, the interested reader is referred to references [89]-[94] for a more detailed study.

3.3 Connectivity and Topology

This section invokes the topological formulations of Cooper and Gupta [95]-[98], which will later on be used to describe real structures and their response (amorphization) upon irradiation with high energy particle beams. With reference to structure in solids, topological considerations deal with the way the structure is connected together and the way the connections govern the possibility of alternative structural arrangements. Before continuing, a few definitions must be established.

Polytopes: Polytopes can be considered to be the basic topological unit in a network. These are normally generalizations of basic 'structural units' in a space of arbitrary dimension. One dimensional polytopes would be 'rods', polygons are two-dimensional polytopes, polyhedra are three-dimensional polytopes. The corresponding geometrical figures in four-dimensional (hyper) space, like those of Sadoc [78]

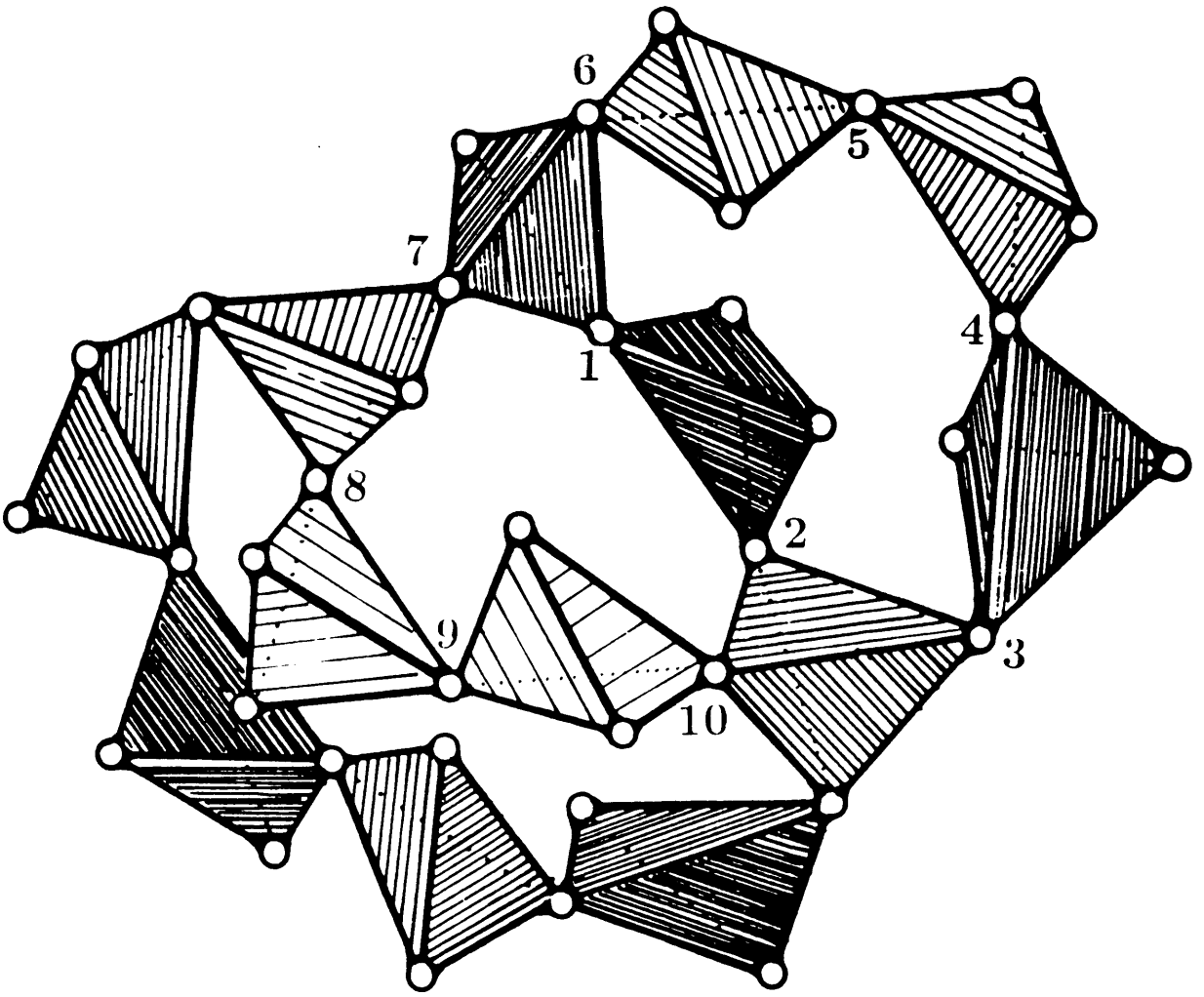

Figure 3-10: A non-primitive intersecting rings (8-ring).

discussed earlier, would also be considered polytopes.

Polytope Dimension δ: The minimum dimension of Euclidian space necessary to fully describe a polytope is its dimension δ. This would mean δ (point) = 0, δ (rod) = 1, δ (polygon) = 2, δ (polyhedron) = 3, δ ('hyper sphere') = 4 and so on.

Regular, Congruent & Rigid Polytopes: A δ-dimensional polytope is regular if all of its faces are alike and all faces are regular (δ - 1)-dimensional polytopes. As an example, a polygon is regular if all of its sides ('faces' with δ - 1 dimension) are equal and it is equiangular. While there are an infinite number of regular polygons, there are only a finite number of regular polytopes in three dimensions (and in 'hyper-space') [73]. Congruent polytopes are identical in all respects. Congruent regular polytopes have the same dimensions, number of vertices and the same size. Rigid polytopes have a fixed shape and size. In real aperiodic (amorphous) structures, the coordination polyhedra, considered as polytopes, may not be rigid, as lack of rigidity of the polyhedra always favors random network formation.

Vertex Number V: V is simply defined as the number of vertices for a given polytope. For example, V (rod) = 2, V (triangle) = 3, V (square) = 4, and so on. Also, Y is defined as the fraction of vertices that are edge-sharing and Z is the fraction of vertices sharing p-sided faces.

Network Dimension d: The minimum dimension of the Euclidian space in which a network can be embedded by deforming without severing or adding any extra connections is called the network dimension, d.

Connectivity C: This is defined as the average number of polytopes sharing a given vertex.

Structural Connectivity: This utilizes the definition of V and C (defined above) to represent the connectivity in a given structure (network). We represent the structural connectivity by $\{V, C\}$.

Topologically Equivalent, Topologically Ordered & Topologically Disordered Networks: Two networks can be considered topologically equivalent when one can be converted into the other without severance of any connections. Thus a network is topologically ordered if it is topologically equivalent to a crystalline network, other-

wise it is topologically disordered, even if the structural connectivity, $\{V, C\}$, is the same. This is illustrated in Fig. 3-11, which shows topologically ordered and disordered network for the same {3,2} structure.

A fundamental explanation for variability (randomness) in network structures is topology and involves an assessment of what may be called 'structural freedom' [69]. This assessment is based on connectivity and goes back more than a century to the method of 'constraint counting' introduced by Maxwell [70] to investigate the rigidity of mechanical structures. The approach has been more recently applied to glass-forming ability independently by Cooper [95, 96] and Phillips [99]-[101]. The principal parameter to be evaluated is available freedom to form an alternative structural arrangement. In considering the topological foundations of Zachariasen's rules for glass formation [71], Cooper considered the connectivity of structuring polytopes (for three-dimensional ceramic compounds, these are the familiar cation coordination polyhedra of Pauling's rules) and showed that, for some combinations of polytope and connectivity, a structure is constrained (usually *over*-constrained) to be crystalline, while in other cases *marginally*- or *under*-constrained and free to adopt aperiodic configurations.

It is shown below that structural freedom to adopt alternative arrangements is a function of the connectivity of the structure. As a way of recognizing the relationship between topology and structural freedom, we first consider some simple, but instructive, examples depicted in Fig. 3-12 and Fig. 3-13. Representing connectivity by {V,C}, the two-dimensional structures in Fig. 3-12 and Fig. 3-13 are {2,2}, {2,3}, {2,4}, {2,6}, {3,2}, {3,3} and {4,2}. In two dimensions, V=2 for one dimensional rods, V=3 for two dimensional triangles, V=4 for two dimensional squares, and so on. As is clear from the schematic models depicted in Fig. 3-12 and Fig. 3-13, the {2,2} arrangement is limited only by the intersection of two rod polytopes, and the {2,3} arrangement by intersection of three rod polytopes; these structures are *under*-constrained and can take on irregular configurations while still satisfying the

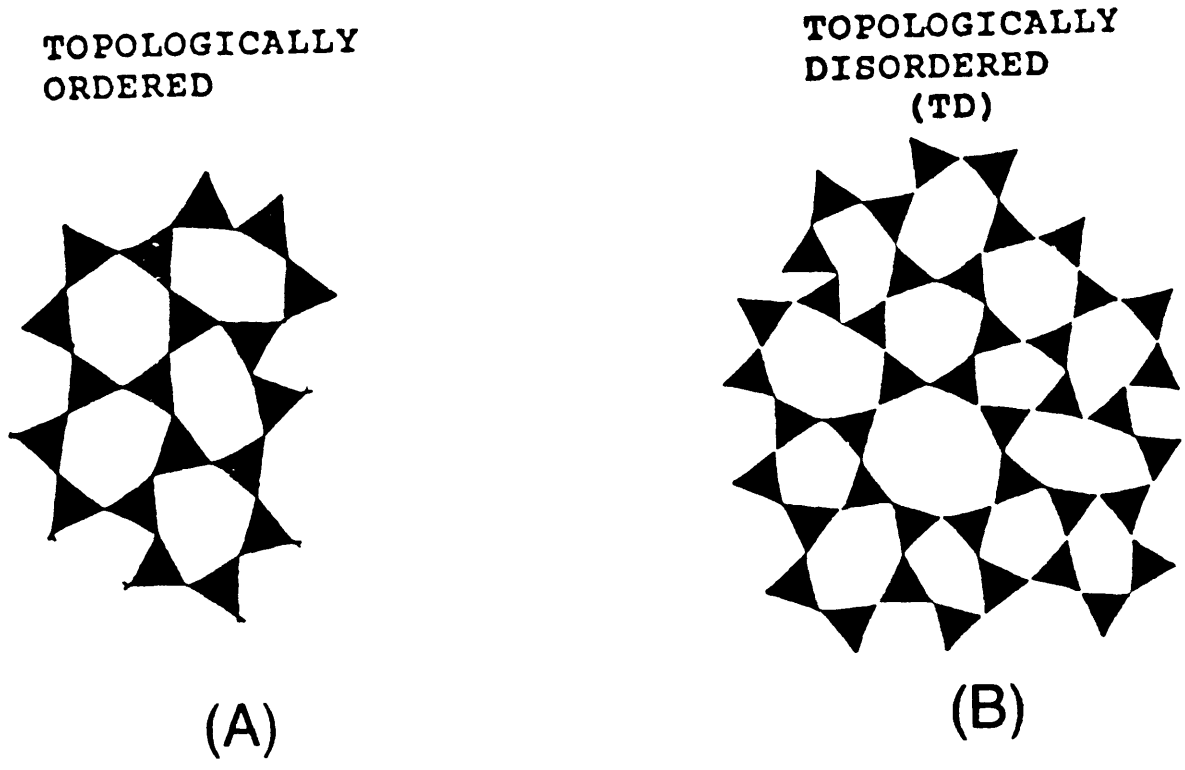

Figure 3-11: Schematic of a {3,2} network exhibiting topological order (A) and topological disorder (B).

prescribed connectivity. In order to evaluate the constraints imposed by more complex connectivities, it is useful to establish the degree of structural freedom f, which is equal to the dimensionality d of the structure (which is also the degree of freedom potentially available to a vertex) less the the number of constraints h imposed by connections to the neighboring elements. Gupta and Cooper [97, 98] have quantified the available freedoms in such arrangements and shown that, for a polytope of dimension δ,

$$f = d - C\{\delta - [\delta(\delta+1)/2V)\} - (d-1)(Y/2) - [(p-1)d - (2p-3)](Z/p), \quad (3.4)$$

where the number of constraints h is given by

$$h = C\{\delta - [\delta(\delta+1)/2V)\} - (d-1)(Y/2) - [(p-1)d - (2p-3)](Z/p) \quad (3.5)$$

where Y is the fraction of edge-sharing vertices and Z is the fraction of vertices sharing p-sided faces.

For the {2,2} and {2,3} arrangements in Fig. 3-12, f is +1.0 and +0.5 respectively, and the arrangements are unconstrained and free to adapt arbitrary configurations. Conversely, for {2,6}, f is -1.0 and is overconstrained, and indeed forced to be crystalline. The two-dimensional arrangements {3,3} and {4,2}, which have f = -1.0 and -0.5 respectively, are similarly *over*-constrained. Also, it is seen (Fig. 3-13) that {4,2} has more *freedom* than {3,3}. However, for arrangements {2,4} and {3,2}, which have $f = 0$, the structure is marginally-constrained; there is no freedom once the boundary is set, but altering the boundary allows other possibilities. Values of $f > 0$ therefore imply freedom to rearrange arbitrarily, while the values of $f < 0$ imply rigid crystalline options.

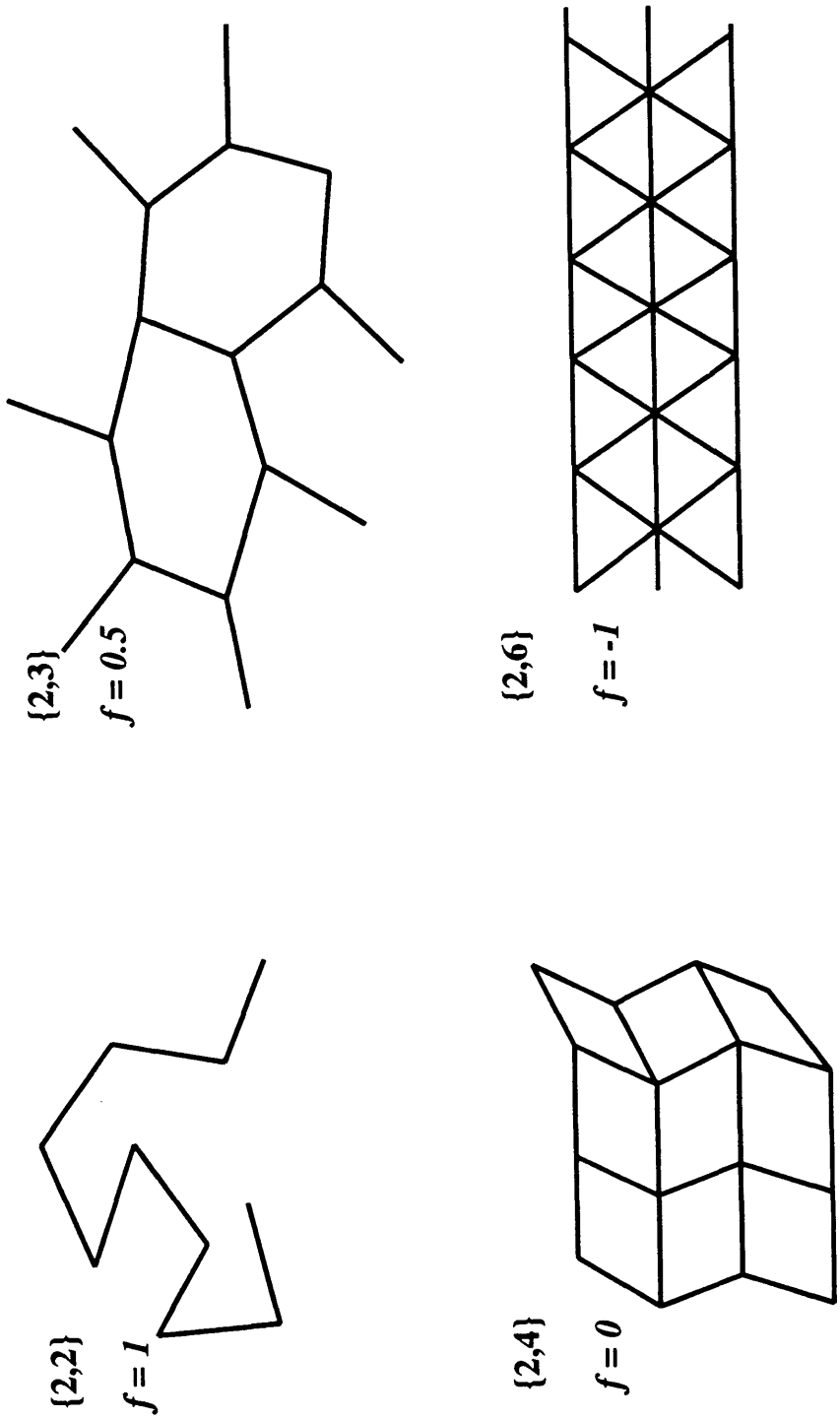

Figure 3-12: Two dimensional (d = 2) networks constructed using 1-D rods ($\delta = 1$, V = 2), with the corresponding connectivities and structural freedoms as indicated.

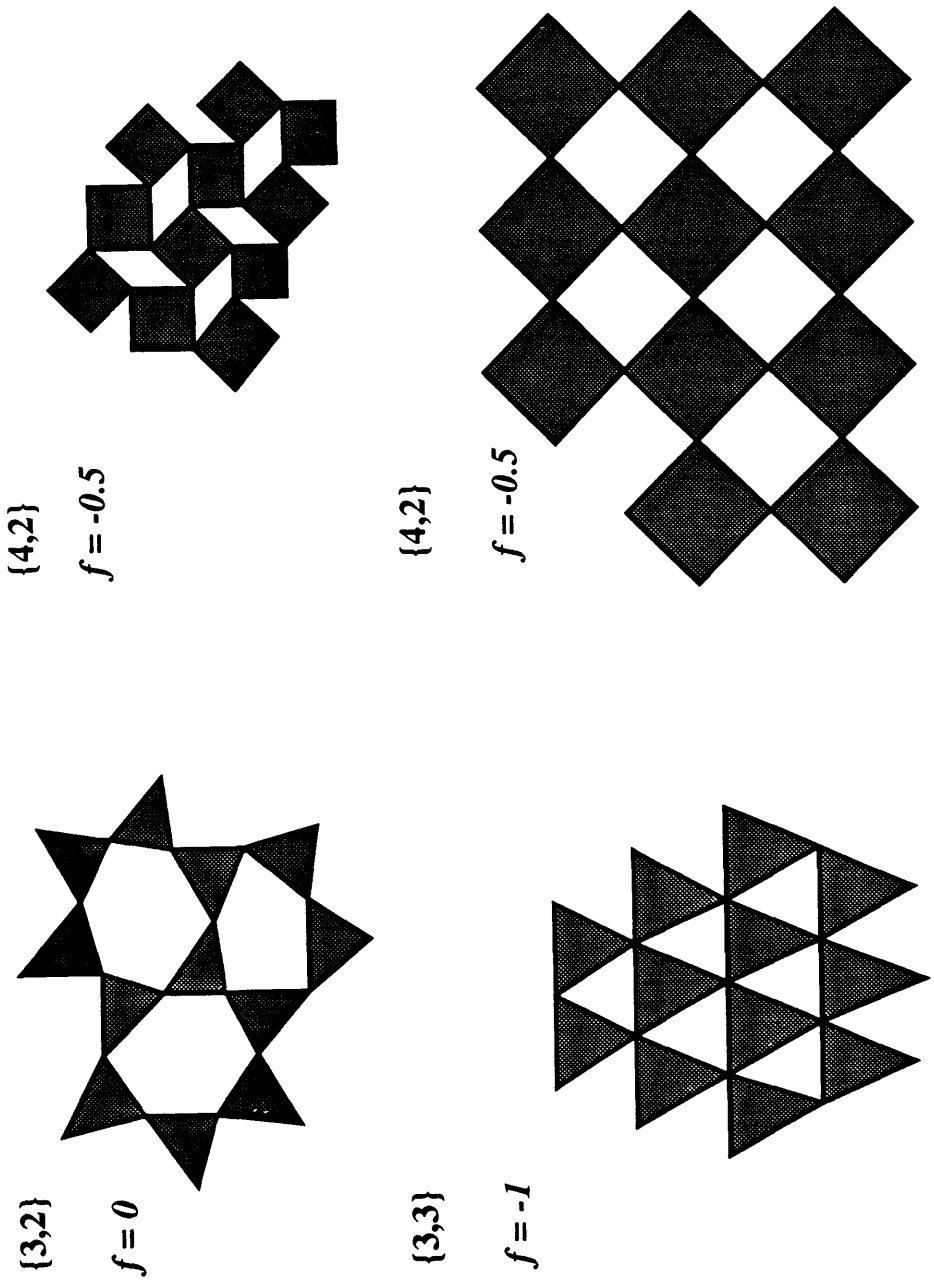

Figure 3-13: Two dimensional (d = 2) networks constructed using 2-D triangular polytopes (δ = 2, V = 3) and 2-D square polytopes (δ = 2, V = 4), with the corresponding connectivities and structural freedoms indicated.

3.4 Real Structures and Topology

In order to understand topology and connectivity in real structures, we first look at some common crystal structure types and evaluate their connectivity and structural freedom.

Rock Salt Structure: The highly ionic MX rocksalt structure of NaCl and MgO shown in Fig. 3-14 involves [MX_6] octahedra of cations around anions (or *vice versa* for this symmetry). Furthermore, there are six octahedra sharing a single vertex and all of the edges of all the octahedra are shared with other octahedra. This results in a {6,6} structural connectivity, and equation 3.4 gives the structural freedom value of f = -10.0. Octahedra in the fully edge-shared rocksalt structure are seriously overconstrained and likely never to be found in an unalloyed aperiodic arrangement.

Rutile Structure: Rutile, (TiO_2), involves a tetragonal lattice cell and has [TiO_6] octahedra of O anions around Ti cations. However, not all edges are shared. In fact the vertices alternate edge- and corner-sharing to build up the network, see Fig. 3-15. Corners are shared along [$1\bar{1}0$] directions parallel to the crystallographic c axis and edges along [110] axis, again parallel to the crystallographic c axis. This brings the structural connectivity to {6,3} and the value of structural freedom to f = -4.33; though a bit less than that for rocksalt structure, the system is still overconstrained.

Perovskite Structure: This structure involves fully corner-sharing octahedra as in ReO_3 structure, (a structure that is adopted by the glass-former AlF_3, and of which perovskites, for example, $CaTiO_3$ are a stuffed derivative), resulting in {6,2} connectivity and f = -1. Fig. 3-16 shows the $CaTiO_3$ structure. For ReO_3 (and AlF_3) structure, the Ca cation site would be unoccupied. In $CaTiO_3$, there is also another polyhedron, more complex than an octahedron, a [CaO_{12}] twelve-coordinated truncated cube, which shares all of its edges with the [TiO_6] octahedral network, hence increasing connectivity; its existence probably lowers $f < -1.0$, though it is not known which of the two polyhedral networks would be considered the dominating polytope.

ROCKSALT

NaCl

Edge-Sharing [$NaCl_6$] Octahedra

V = 6 C = 6 {6,6} *f* = -10

Number of Constraints >> Degrees of Freedom

OVERCONSTRAINED

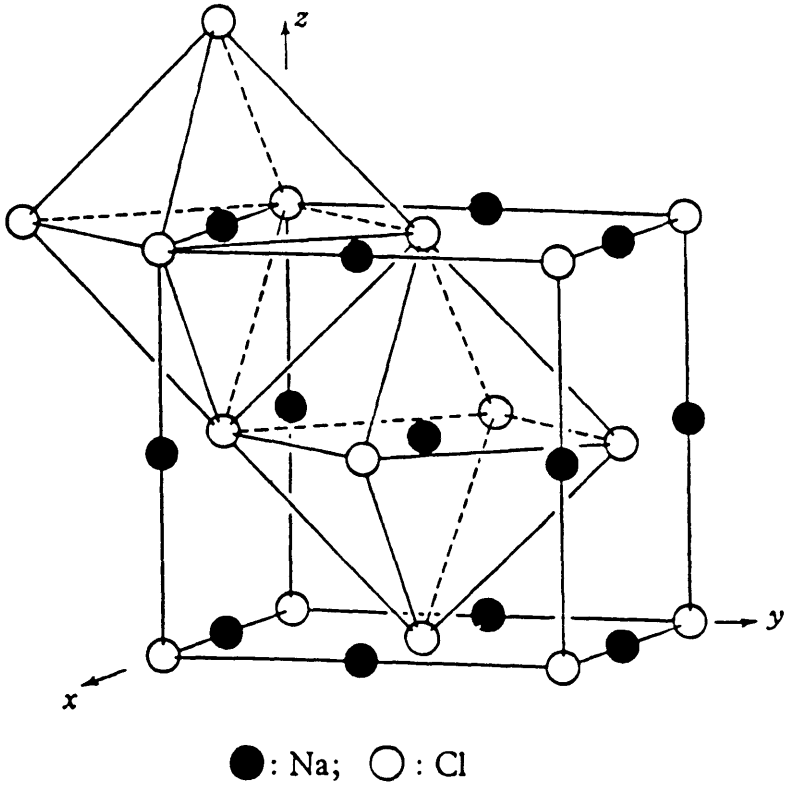

Figure 3-14: Rocksalt structure of NaCl, showing edge-sharing octahedra and other topological parameters.

RUTILE

TiO_2

Edge- & Corner-Sharing [TiO_6] Octahedra

V = 6 C = 3 {6,3} f = -4.33

Number of Constraints >> Degrees of Freedom

OVERCONSTRAINED

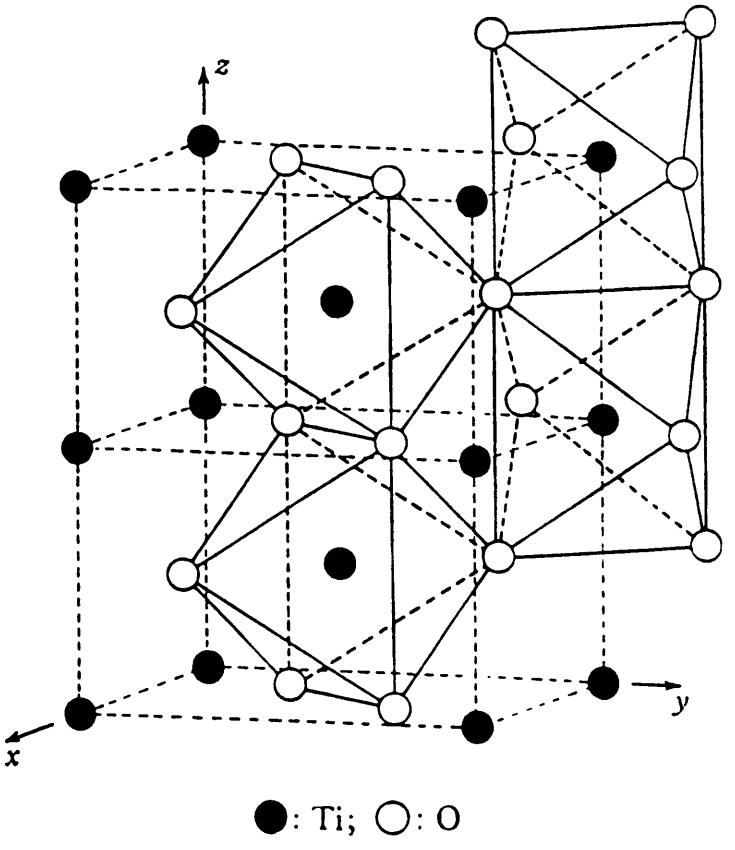

Figure 3-15: Rutile structure of TiO_2, showing corner- and edge-sharing octahedra and other topological parameters.

PEROVSKITE

$CaTiO_3$

corner-Sharing [TiO_6] Octahedra

V = 6 C = 2 {6,2} $f \leq$ -1

Number of Constraints > Degrees of Freedom

OVERCONSTRAINED

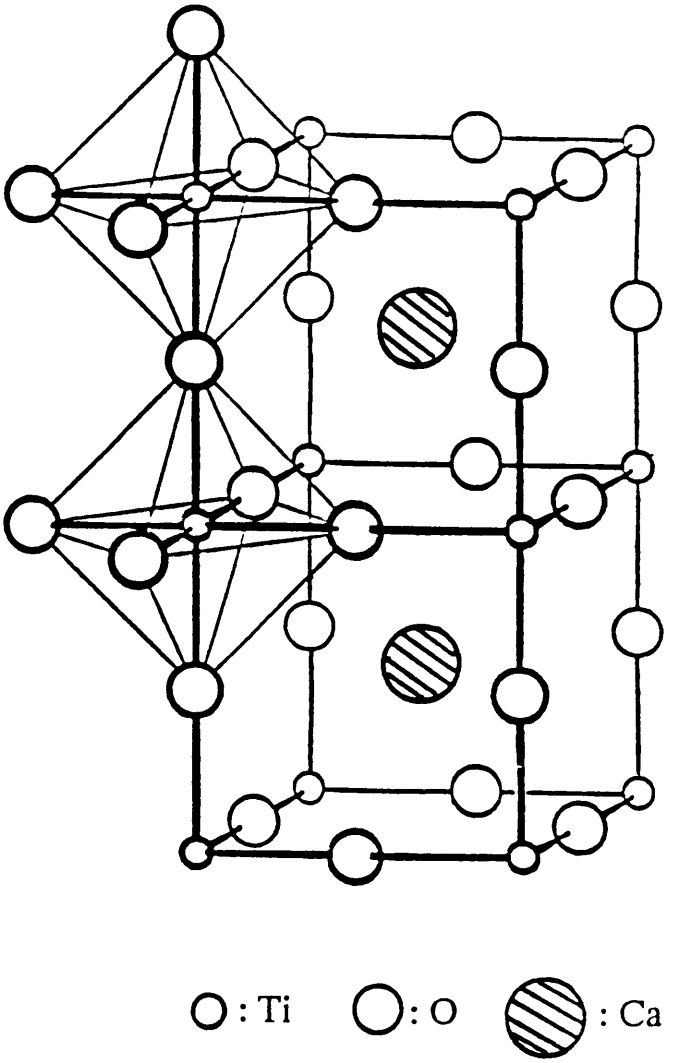

Figure 3-16: Perovskite structure of $CaTiO_3$, showing corner-sharing octahedra and other topological parameters. f for purely corner-sharing octahedra = -1, but with stuffed Ca ions there is a face-sharing with [CaO_{12}] truncated cube, and f is < -1.

Silica Network: Silica (SiO_2) is a glass former, and exists in a large number of structural arrangements, in glassy, metamict and six crystalline polymorphs. All forms of silicas, except stishovite, and also all of framework silicates, are based exclusively on the full corner-sharing of [SiO_4] tetrahedra (or substituted tetrahedra). Such tetrahedral arrangements are *marginally*-constrained ($f = 0$) and exhibit a {4,2} connectivity. Fig. 3-17 shows one such polymorph, the β-cristobalite structure, displaying the connectivity.

Fig. 3-18 is a schematic representation in three-dimensions of the common structural polytopes: triangles (δ =2, V = 3, as in B_2O_3), tetrahedra (δ =3, V = 4, as in SiO_2, $AlPO_4$, P_2O_5, SiC, Si_3N_4) and octahedra (δ =3, V = 6, as in MgO, AlF_3, $CaTiO_3$, TiO_2). The structure of B_2O_3, a facile glass former, based on a {3,2} arrangement of triangles, is even less constrained in three dimensions (f= +1.0) than in two dimensions. Analogous to [SiO_4], [PO_4] tetrahedra in P_2O_5 and many other phosphates share vertices; however, only three out of their four vertices are shared and the structures are therefore underconnected ($f \approx +0.4$). However, edge- and face-sharing of polyhedra (polytopes) introduce serious structural constraints. As an example, TiO_2 (in the rutile structure, discussed above) features partial edge-sharing of the otherwise corner-sharing tetrahedra, with a large reduction in structural freedom (f = -4.33). Table 3.1 lists the structure type, the type of polyhedra sharing, the structural connectivity and the corresponding structural freedom which were determined for a wide range of ceramic materials. The range of the value of f for $ZrSiO_4$ and $CaSiO_3$ are for the two sets of polyhedra sharing respectively.

SILICA/SILICATE NETWORK

SiO_2, β-Cristobalite

corner-Sharing [SiO_4] Tetrahedra

V = 4 **C = 2** **{4,2}** $f = 0$

Number of Constraints = Degrees of Freedom

MARGINALLY CONSTRAINED

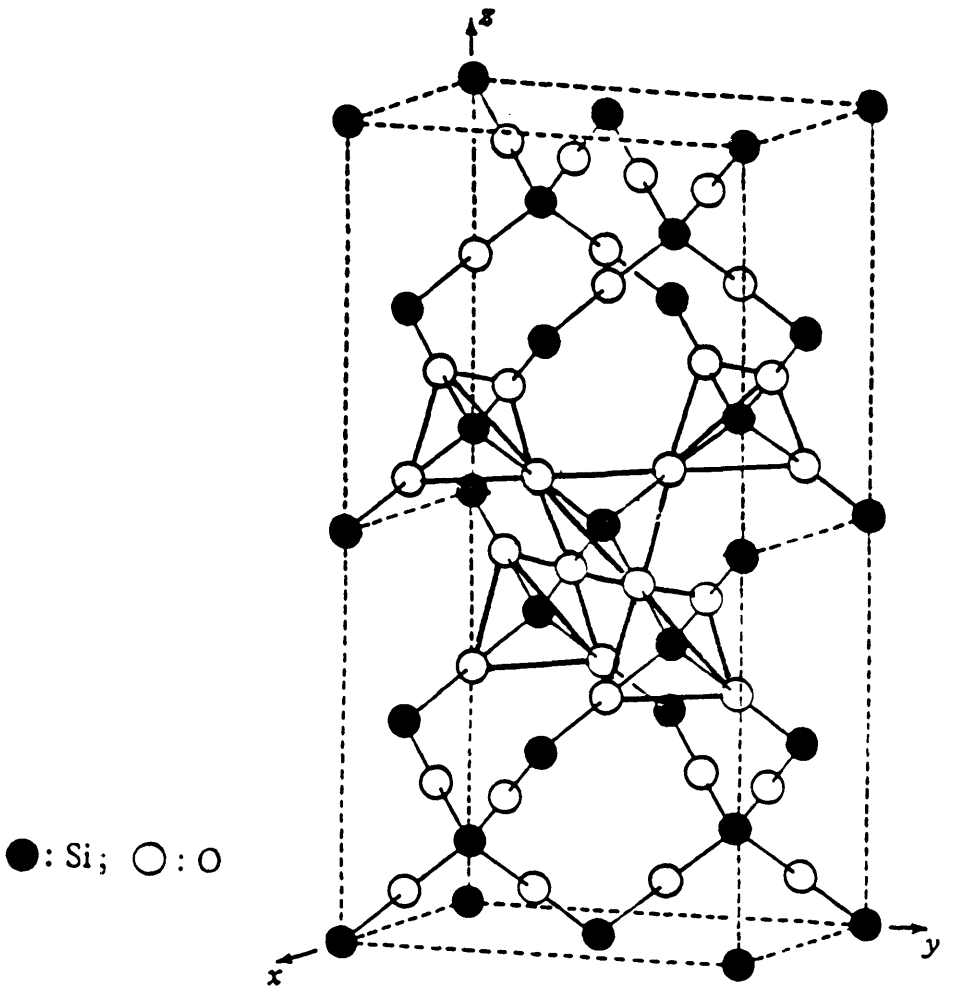

Figure 3-17: Silica network β-Cristobalite displaying full corner-sharing [SiO_4] tetrahedra and other topological parameters.

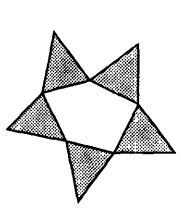

B_2O_3

{3, 2}

f = +1.0

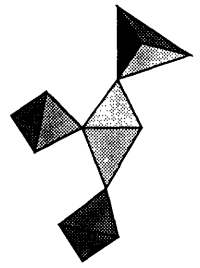

P_2O_5

{4, 1.75}

f = 0.38

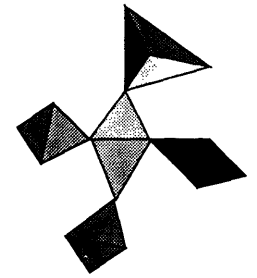

SiO_2

{4, 2}

f = 0

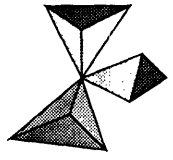

Si_3N_4

{4, 3}

f = -1.5

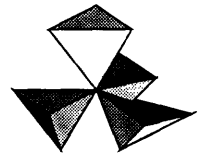

SiC

{4, 4}

f = -3.0

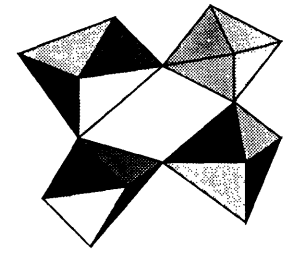

ReO_3 ($CaTiO_3$)

{6, 2}

f = -1.0

Figure 3-18: Corner-sharing triangle, tetrahedron and octahedron polytope connectivities in six network structure types.

Table 3.1: Coordination, connectivity, and structural freedom for several structures.

Structure	**Polyhedra : Sharing**	**{V,C}**	f
MgO	Octahedra : Edges	{6,6}	-10.0
α-Al_2O_3	Octahedra : Edges, Faces	{6,4}	-6.25
TiO_2	Octahedra: corners, edges	{6,3}	-4.33
SiC	Tetrahedra : Corners	{4,4}	-3.0
Si_3N_4	Tetrahedra : Corners	{4,3}	-1.5
$CaTiO_3$	~Octahedra : Corners	{6,2}	< -1.0
ReO_3	Octahedra : Corners	{6,2}	-1.0
$ZrSiO_4$	Dodecahedra : Edges; Tetrahedra : Edges		$-3.0 < f < -1.0$
$CaSiO_3$	Octahedra : Edges; Tetrahedra : Corners		$-1.33 < f < -1.0$
SiO_2	Tetrahedra : Corners	{4,2}	0
c.p. metals	rods:ends	{2,6}	0
P_2O_5	Tetrahedra : Corners	{4,1.75}	+0.38
Si	Rods : Ends	{2,4}	+1.0
B_2O_3	Triangles : Corners	{3,2}	+1.0

Chapter 4

Results and Discussion

4.1 Electron Microscopy

4.1.1 Imaging Metamict Phosphates using STEM

For ion-implanted lead phosphates (glasses in particular), which are diffraction amorphous, diffraction (Bragg) contrast imaging is not a possibility; imaging (in cross-section) under zero-loss bright and annular dark field STEM modes is expected to give better (phase) contrast than conventional TEM in its imaging modes [102]. This is attributed to the difficulty in focusing the inelastically scattered electrons (not energy-filtered) due to chromatic aberration in the lenses of a conventional TEM. Fig. 4-1 and Fig. 4-2 show the bright-field and dark-field zero-loss STEM cross-section images, respectively, of P^+ ion-irradiated (100 kV ion accelerating voltage, ion fluence of $2\times10^{20}/m^2$) lead metaphosphate glass. The metamict layer is ~225 nm deep and appears to be phase-separated into darker and lighter regions. However, the entire metamict layer was found to be diffraction amorphous, as expected. Using micro-diffraction on the STEM, with a 1.5 nm spot size, the phase-separated darker and lighter regions were both confirmed to be diffraction amorphous. However, the electron microprobe analysis of the darker regions (in bright-field mode) using X-ray energy dispersive spectroscopy (XEDS) showed them to be richer in Pb. Such phase-separated metamict states are expected to have significantly different phos-

phate group linkages.

Fig. 4-3 shows a bright field cross-section STEM image, also in zero-loss imaging mode, for the lead pyrophosphate glass also P^+ ion-irradiated using 100 kV ion accelerating voltage to a fluence of $2\times10^{20}/m^2$. Fig. 4-4 is its corresponding annular dark-field image. This metamict phosphate also shows phase separation into darker and lighter regions. It exhibits similar diffraction characteristics to that of the metamict metaphosphate glass; however, the morphology of the phase separated regions is 'globule-like' rather than 'channel-like'. Lead pyrophosphate single crystals, implanted to the same high fluence P^+ dose, showed similar morphological phase separation as for the glass composition (see Fig. 4-5). The metamict layers for both the metamict lead pyrophosphates (glass and single crystals) were ~200nm deep, in surprisingly good agreement with the end of the range value calculated by TRIM. The slightly shallower metamict region for the pyrophosphate composition as compared to the metaphosphate one is expected, owing to the slightly denser pyrophosphate material.

For the lower P^+ fluence of $10^{19}/m^2$, the phase separation in the metamict layer for the single crystal is no longer apparent, as revealed by the cross-section zero-loss STEM images in Fig. 4-6 and Fig. 4-7. Although, the highest P^+ implant dose ($2\times10^{20}/m^2$) corresponds to a change in P composition at the implant profile peak of less than 1%, the local chemical inhomogeneities of the phase-separated metamict layer can be attributed to large differences in scattering cross-sections between the incoming ion and the Pb, P, or O in the multicomponent host material [68]. A small local variation in the chemical composition, and the requirement of charge balance between cations and anions, might act as the driving force for the creation of phase separated regions after a certain critical dosage of incoming ions.

Fig. 4-5 also displays the degree of difficulty in preparing the cross-section TEM samples of the highly micaceous $Pb_2P_2O_7$ single crystal. The metamict layer shown

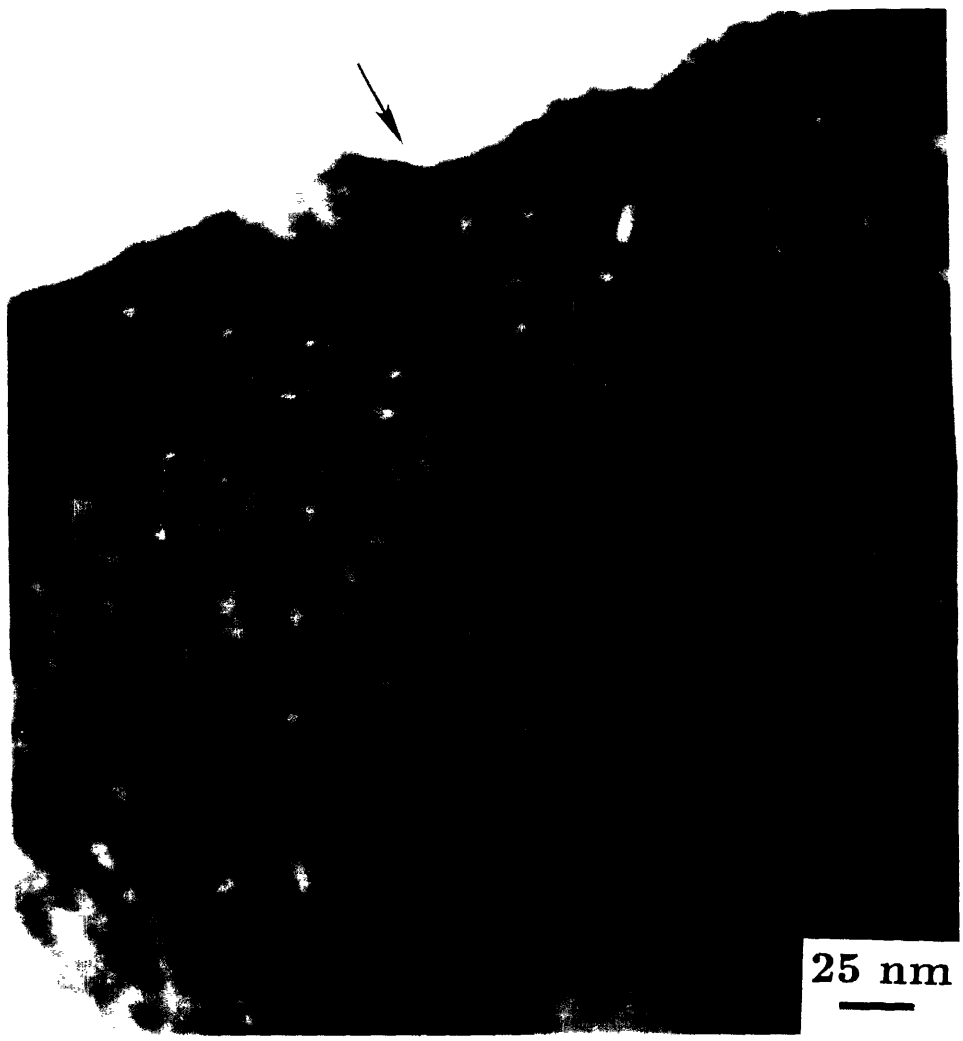

Figure 4-1: Bright-field zero-loss STEM cross-section image of $PbO{\cdot}P_2O_5$ glass which was P^+ ion-irradiated at 100 kV accelerating voltage to a fluence of $2{\times}10^{20}/m^2$. The arrow indicates the direction of incoming ion beam.

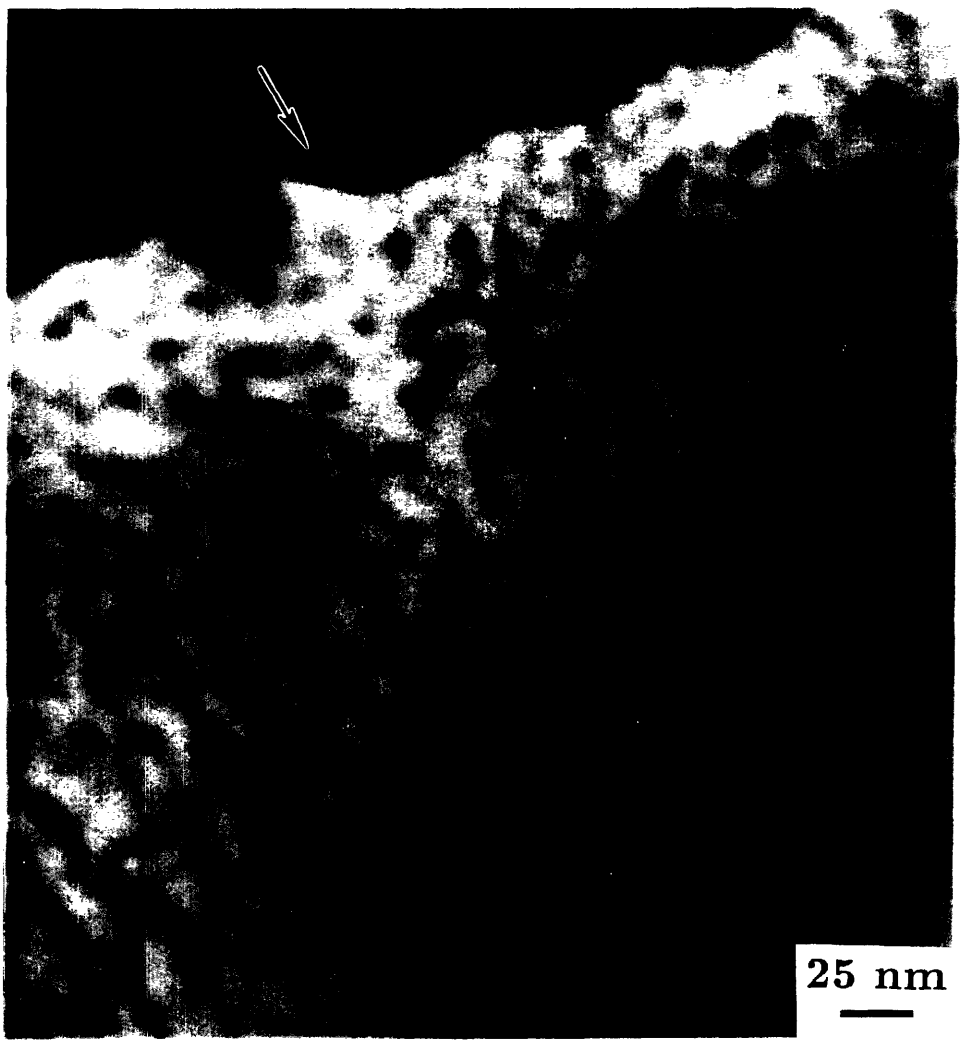

Figure 4-2: Corresponding annular dark-field zero-loss STEM cross-section image of $PbO{\cdot}P_2O_5$ glass which was P^+ ion-irradiated at 100 kV accelerating voltage to a fluence of $2{\times}10^{20}/m^2$. The arrow indicates the direction of incoming ion beam.

Figure 4-3: Bright-field zero-loss STEM cross-section image of $Pb_2P_2O_7$ glass which was P^+ ion-irradiated at 100 kV accelerating voltage to a fluence of $2\times10^{20}/m^2$. The arrow indicates the direction of incoming ion beam.

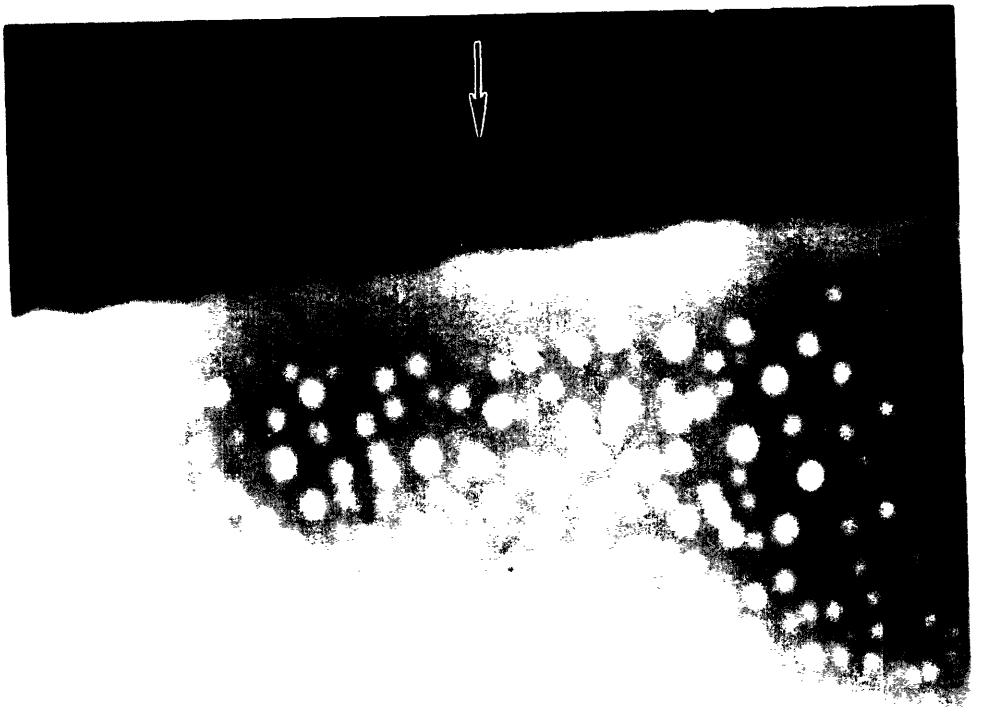

Figure 4-4: Corresponding annular dark-field zero-loss STEM cross-section image of $Pb_2P_2O_7$ glass which was P^+ ion-irradiated at 100 kV accelerating voltage to a fluence of $2\times10^{20}/m^2$. The arrow indicates the direction of incoming ion beam.

Figure 4-5: Bright-field zero-loss STEM cross-section image of $Pb_2P_2O_7$ single crystal which was P^+ ion-irradiated at 100 kV accelerating voltage to a fluence of $2\times10^{20}/m^2$. The arrow indicates the direction of incoming ion beam.

in this figure is nearly cleaved off. The preparation difficulty increases with increasing ion irradiation fluence as the expansion of the metamict material into the denser crystalline matrix gives rise to additional stresses. Preparation of such TEM transparent (<100 nm thick) samples must therefore be done very carefully. Such samples survived only one session in the microscope; the stresses involved in loading and unloading the sample into the STEM/TEM specimen holders were sufficiently damaging to preclude its being used a second time.

4.1.2 High Resolution Electron Microscopy

Ion-Induced Metamictization

While imaging in the STEM mode gives useful information regarding (phase) contrast within the metamict layer, it does not have the capability to look at the interface between the metamict layer and the pristine single crystal under high resolution, to provide direct access to crystal-structure details and irregularities. For this very purpose, HRTEM was used to look at such interfaces to see how the metamict layer interfaces with the pristine single crystals.

Fig. 4-8, Fig. 4-9 and Fig. 4-10 are cross-section HRTEM images of $Pb_2P_2O_7$ single crystals implanted to increasing P^+ fluences. For moderate and lower P^+ fluences ($< 5 \times 10^{19}/m^2$), the interface between the metamict layer and the pristine single crystal is diffuse, for about the last 10-15 nm before the end of range (~200 nm deep). However, for a critical dose of P^+ of $5 \times 10^{19}/m^2$ and higher, the interface is almost one atom plane sharp (see Fig. 4-10) and occurs at the very end of the range, i.e. ~200 nm deep into the material. This observation is also consistent with the result for O^+ ions implanted at an accelerating voltage of 55 kV. Fig. 4-11 and Fig. 4-12 show cross-section HRTEM images of $Pb_2P_2O_7$ single crystals for the oxygen implantations. The critical O^+ ion dose for such a sharp interface is, however, $10^{20}/m^2$. This slightly higher value for this critical dosage is likely due to the lighter oxygen ion, even though the end of the range (~200 nm) and the damage peak (~75

Figure 4-6: Bright-field zero-loss STEM cross-section image of $Pb_2P_2O_7$ single crystal which was P^+ ion-irradiated at 100 kV accelerating voltage to a fluence of $10^{19}/m^2$. The arrow indicates the direction of incoming ion beam.

Figure 4-7: Annular dark-field zero-loss STEM cross-section image of $Pb_2P_2O_7$ single crystal, printed as a mirror image of previous Fig., which was P^+ ion-irradiated at 100 kV accelerating voltage to a fluence of $10^{19}/m^2$. The arrow indicates the direction of incoming ion beam.

nm) were maintained the same for both the ion species implanted.

Such sharp interfaces at the end of the range region for ion irradiated ceramics have not been reported in the literature, owing perhaps to lack of HRTEM studies of cross-section samples ion-irradiated to a range of doses. However, this phenomenon is as yet unexplained. One explanation could be that the sufficiently positive structural freedom adopted by single-crystal $Pb_2P_2O_7$ (see Chap. 3) allows for sufficient rearrangement of the phosphate network up to certain critical damage levels, but beyond such a critical value, the structure cannot tolerate any further loss of constraints, and epitaxial regrowth occurs. In addition, the crystallization front (epitaxial) is expected to be much sharper than the amorphization front (due to implanted ion statistics), the sharpness of this interface suggests an epitaxial regrowth. It is yet to be explained as to why this regrowth should stop near end of the range of the implanted ions.

Fig. 4-10 reveals another anomaly: $\sim$10 nm dark spherical regions in the micrograph. Looking at them in the pristine single crystal area, the lattice structure in both the directions appear rather continuous right through these dark regions suggesting that this might either be an ion-beam thinning (TEM sample preparation) surface artifact or some precipitate, perhaps on the surface of this sample. However, in the metamict part, at least one of these 'blobs' has lattice fringes which (perhaps coincidently) match the Pb [110] fringes. XEDS evidence suggests that the darker regions were richer in Pb content. This indicates that phase-decomposition into Pb-rich regions occurred perhaps during the initial crystal growth itself. Since none of the other cross-section HRTEM micrographs, for either lower or higher fluence implantations, with either P^+ and O^+ shows such contrast, the phenomenon is relegated to an anomaly occurring during crystal growth.

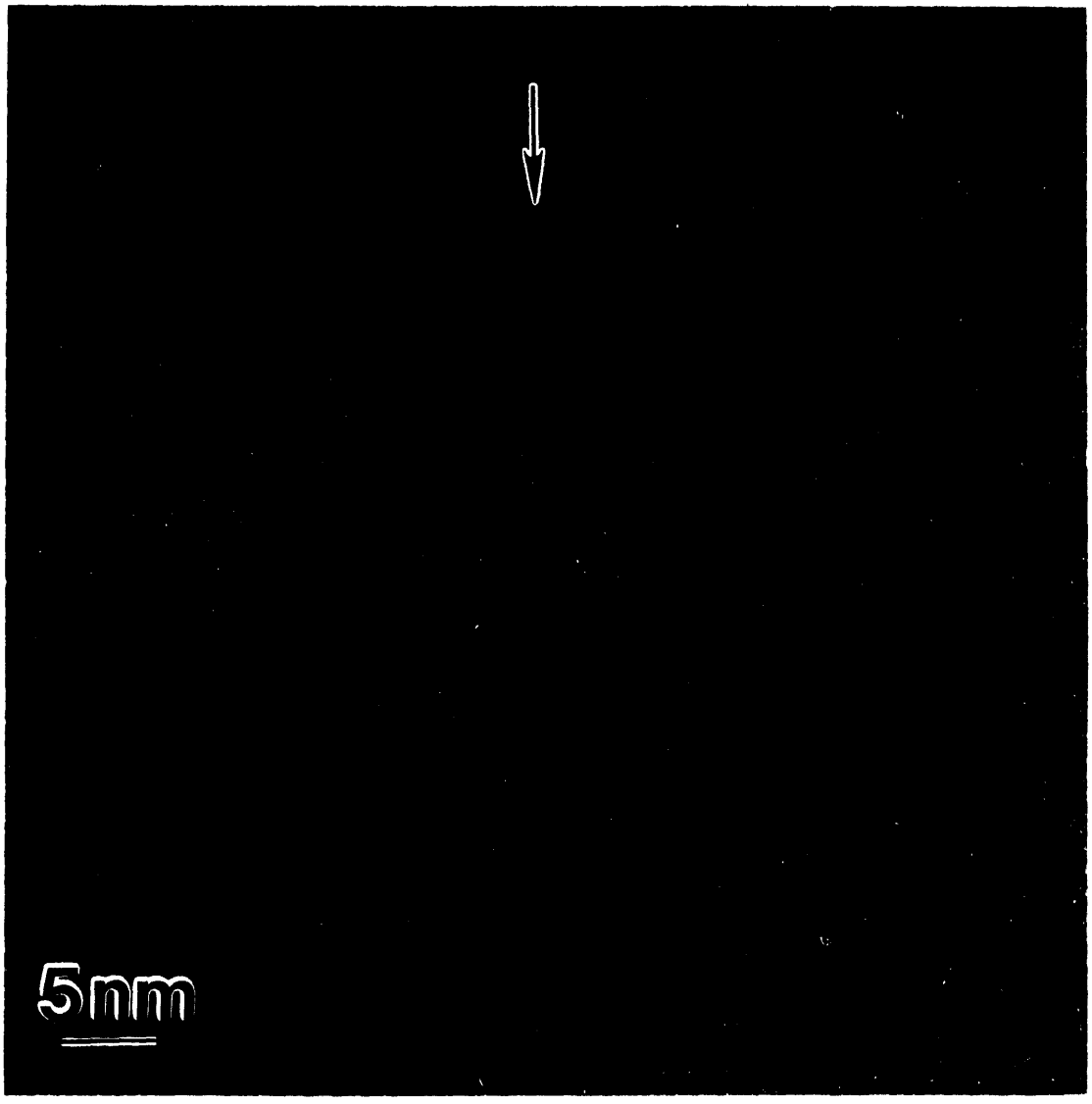

Figure 4-8: HRTEM cross-section image of $Pb_2P_2O_7$ single crystal which was P^+ ion-irradiated at 100 kV accelerating voltage to a fluence of $5\times10^{17}/m^2$. The arrow indicates the direction of incoming ion beam.

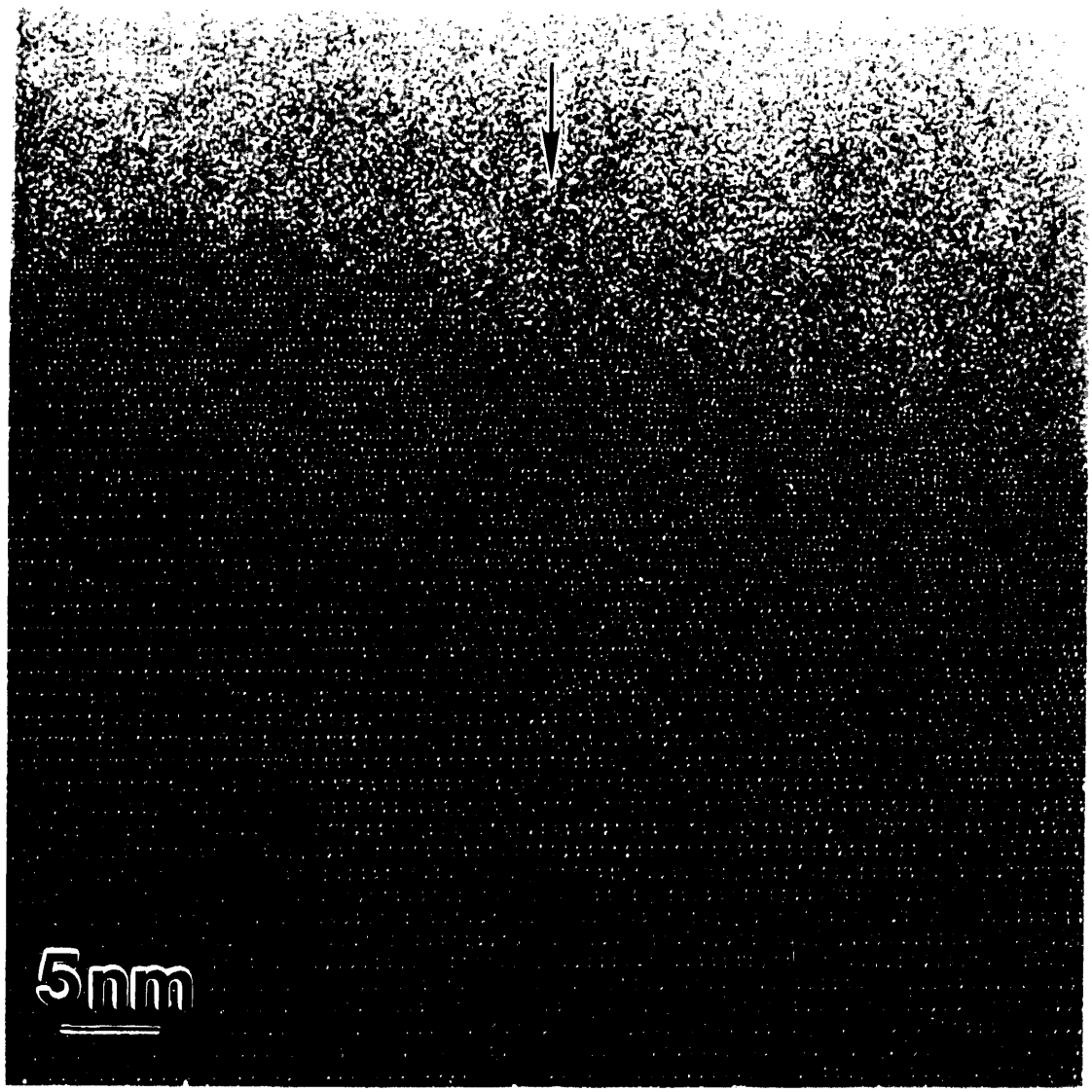

Figure 4-9: HRTEM cross-section image of $Pb_2P_2O_7$ single crystal which was P^+ ion-irradiated at 100 kV accelerating voltage to a fluence of $10^{18}/m^2$. The arrow indicates the direction of incoming ion beam

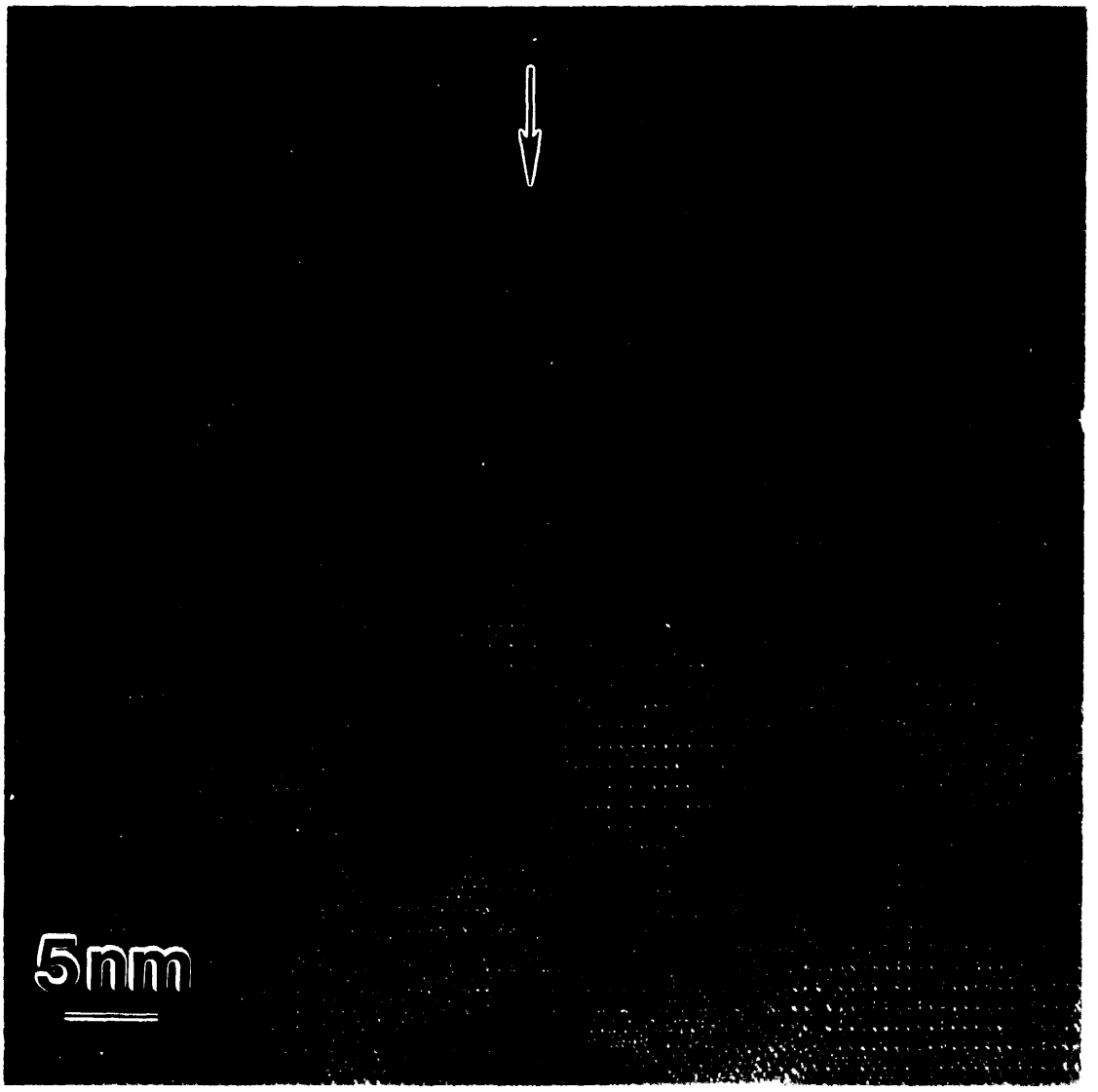

Figure 4-10: HRTEM cross-section image of $Pb_2P_2O_7$ single crystal which was P^+ ion-irradiated at 100 kV accelerating voltage to a fluence of $5\times10^{19}/m^2$. The arrow indicates the direction of incoming ion beam.

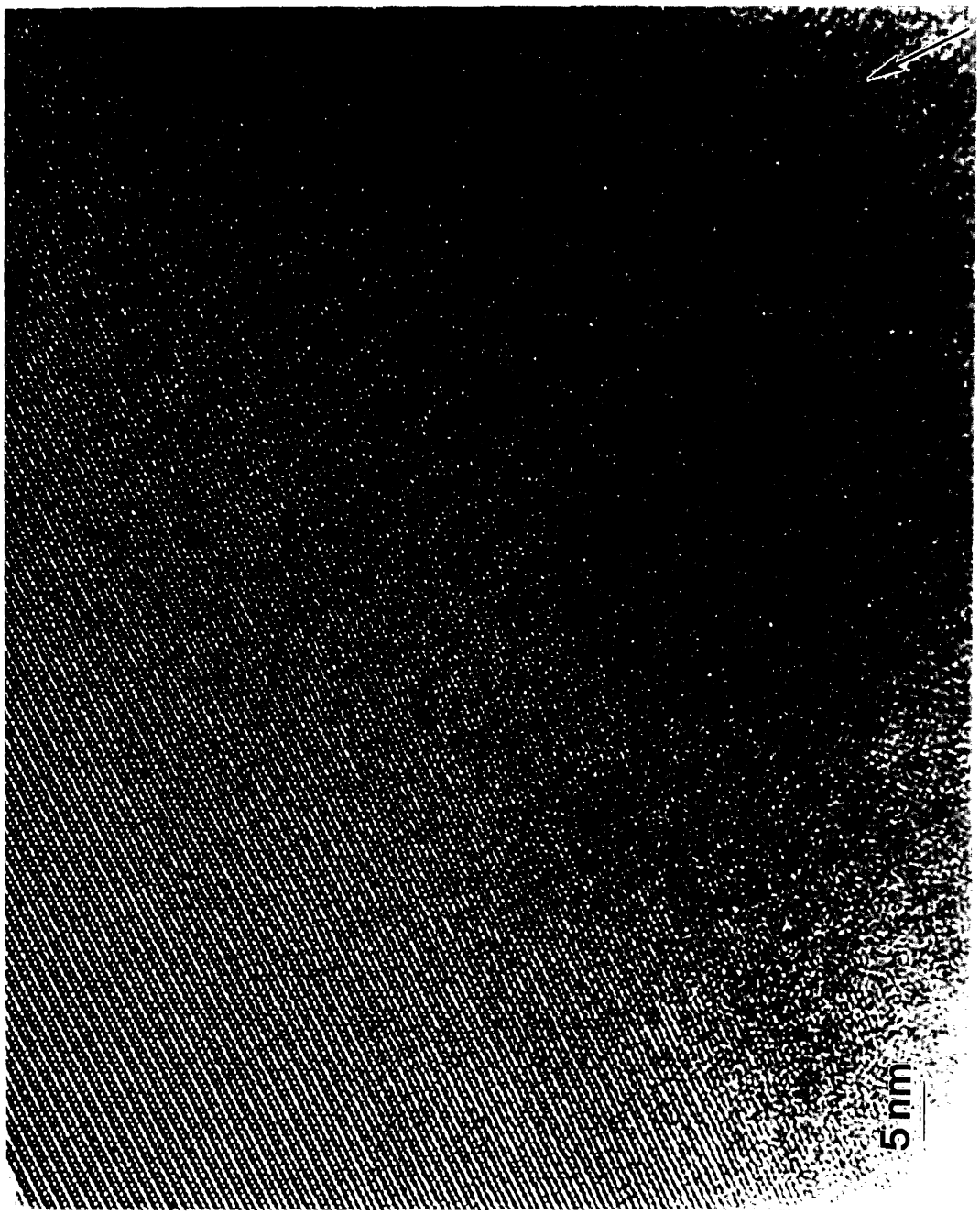

Figure 4-11: HRTEM cross-section image of $Pb_2P_2O_7$ single crystal which was O^+ ion-irradiated at 55 kV accelerating voltage to a fluence of $10^{18}/m^2$. The arrow indicates the direction of incoming ion beam.

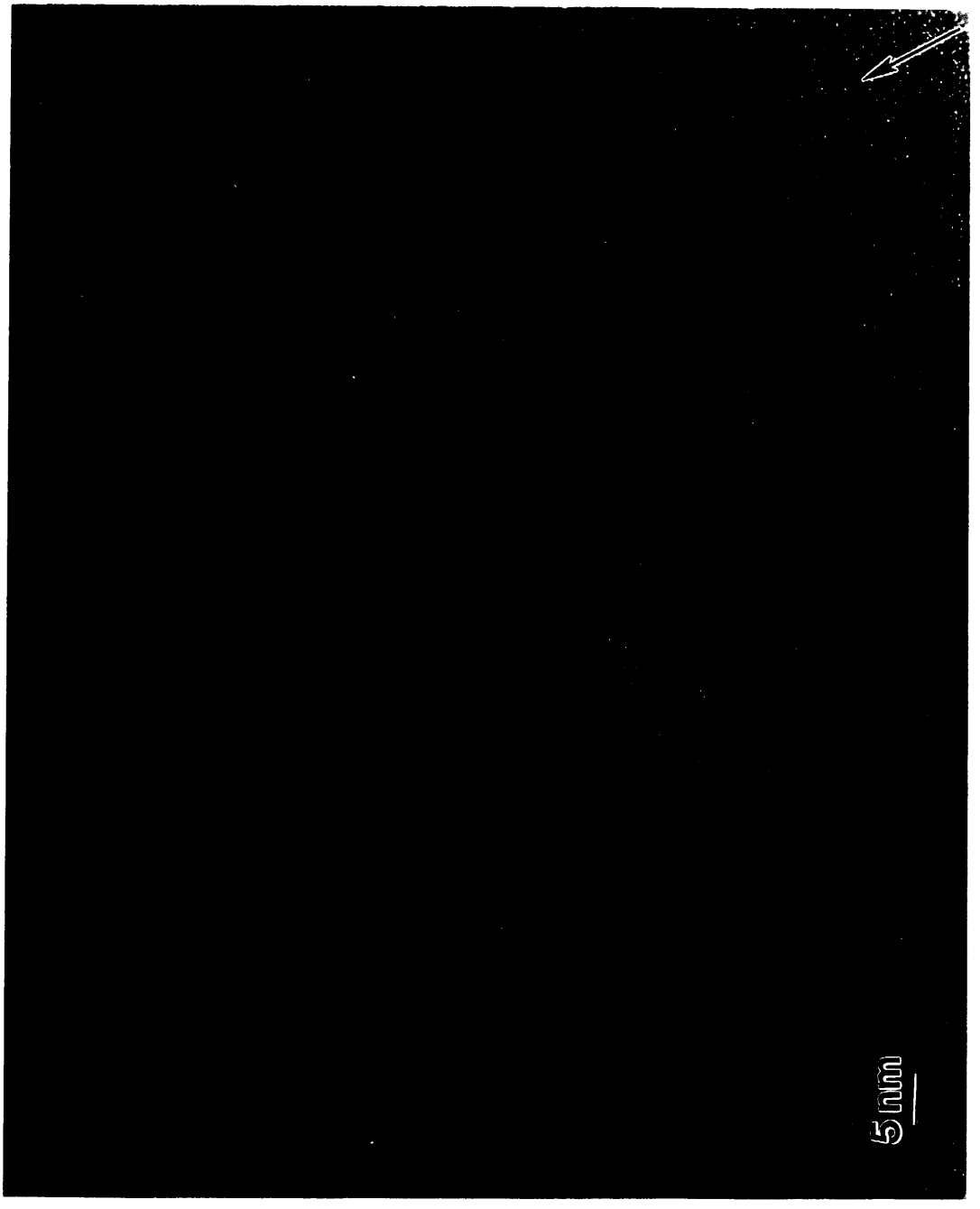

Figure 4-12: HRTEM cross-section image of $Pb_2P_2O_7$ single crystal which was O^+ ion-irradiated at 55 kV accelerating voltage to a fluence of $10^{20}/m^2$. The arrow indicates the direction of incoming ion beam.

Electron-Induced Metamictization (Radiolysis)

Lead pyrophosphate single crystals were found to be beam-stable under 200 kV TEM electrons, and no change in the structure was seen, even after two hours of continuous exposure to an intensely focused electron beam in high-resolution mode, corresponding to an electron fluence $> 10^{27} e/\mathrm{m}^2$ and an ionizing dose $> 10^{14}$ Gy. Fig. 4-13 shows the HRTEM micrograph after such a heavy electron irradiation. This negative result was surprising, since at least one mineral orthophosphate, monazite (mainly $CePO_4$), has been reported to be beam-sensitive in the TEM [103]-[106]. It firmly establishes that crystalline lead pyrophosphate does not undergo degradation by a radiolytic mechanism and leaves ballistic displacement by ions (or neutrons) as the only metamictization routes.

Berlinite ($AlPO_4$), however, amorphizes rather easily under conventional 200 kV TEM electron irradiation [108]. Fig. 4-14 shows a sequence of the growth of an amorphous region around a focused electron beam. A similar result was also observed by Bordes and Ewing [108]. Fig. 4-15 is a set of electron diffraction patterns showing the gradual disappearance of Bragg spots and the appearance of a diffuse halo; finally, the material turns diffraction-amorphous, with the diffuse halo region representing its diffraction (with the concurrent absence of any crystalline spots). Bordes and Ewing [108] reported a value of the critical electron dosage for amorphization as $3 \times 10^{14}/\mathrm{m}^2$. This value, seems unrealistically low and is perhaps a calculation error. We estimated this critical dose to be $\sim 2 \times 10^{23}/\mathrm{m}^2$. The set of figures, Fig. 4-16, 4-17, 4-18 and 4-19, is a sequence of HRTEM micrographs recording structural changes at high resolution. An amorphous front sweeps rapidly (radially) from the focused electron beam and homogeneous amorphization occurs, without any evidence of nucleation and growth of amorphous nuclei (which eventually lead to global metamictization in the case of quartz [109, 25]). The fact that we were able to get a high resolution TEM image for berlinite suggests that the value of the critical electron dose suggested in [108] cannot be correct, as it would not provide sufficient number of electrons (Poisson statistics)

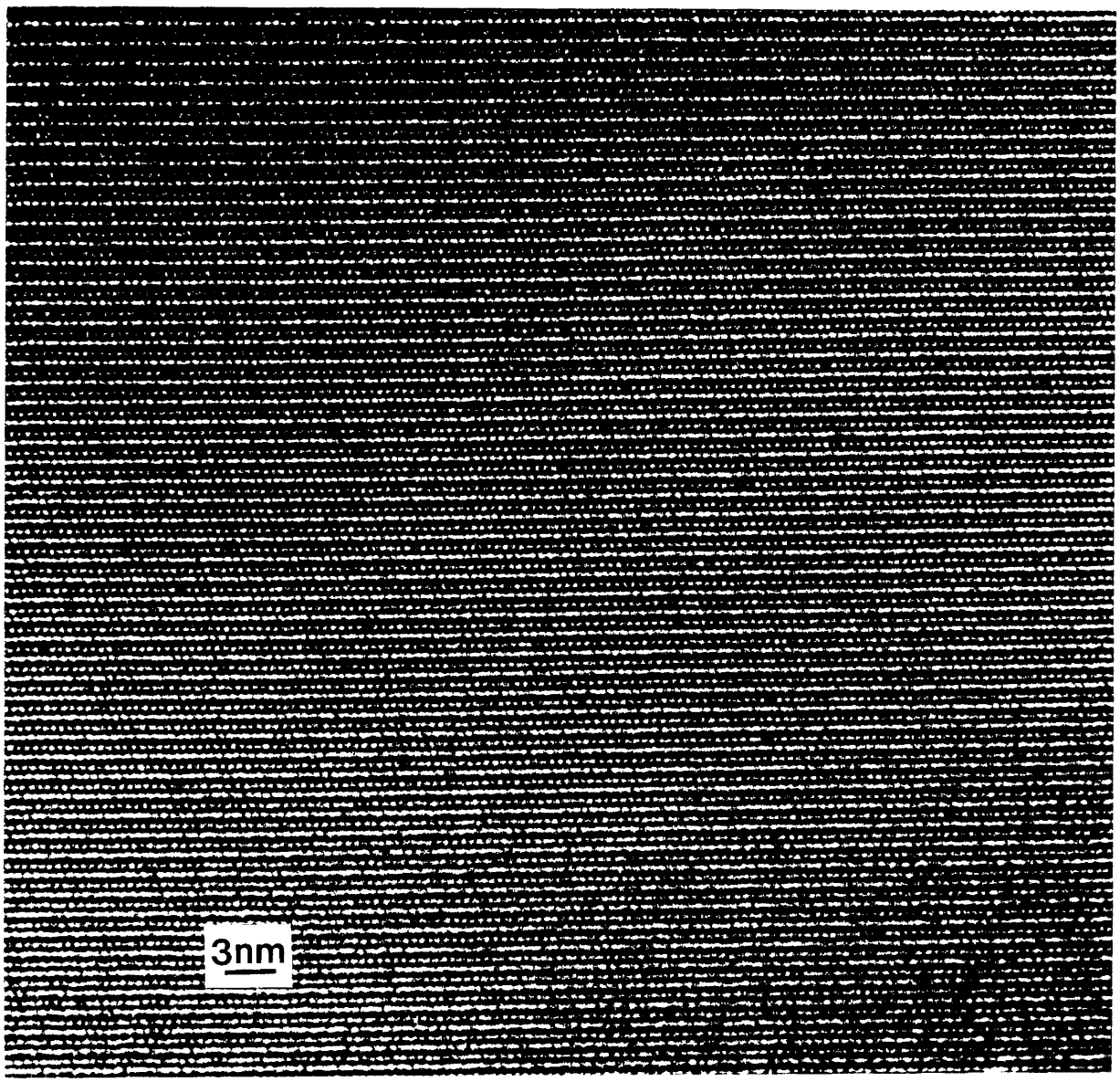

Figure 4-13: HRTEM image of $Pb_2P_2O_7$ single crystal which was electron-beam irradiated at 200 kV to a fluence $> 10^{27} e/m^2$.

to resolve a structure image. The critical electron dose for amorphization of berlinite is about 50 times lower than that reported for quartz [25].

Topologically, lead pyrophosphate single crystals are underconnected, whereas berlinite network consists of fully-connected tetrahedra. Berlinite is in fact isostructural to quartz, so it is not surprising that it undergoes metamictization under electron irradiation. The fact that these two materials are chemically different and yet show a similar response to radiolytic displacements suggests the importance of topology and structure in determining the susceptibility of the material to amorphizing under irradiation.

4.1.3 HRTEM Image Processing: Digital Diffractometry

Diffractograms were obtained by computing the power spectra of the digitized HTREM cross-section images (1024×1024 resolution), as described in chapter 2. When the HRTEM image appears fully crystalline, the corresponding power spectrum shows very sharp Bragg peaks, which is an indication of discrete distribution of spatial frequencies in the original image. A uniform background indicates that the content of irregular noise in the background is minimal [25]. However, when the crystalline image begins to degrade, it is apparent in the calculated power spectrum of the image; the higher order Bragg peaks fade in intensity, and a diffuse background appears as background signal. This is demonstrated in Fig. 4-21 and Fig. 4-22 where the 'diffuse' interface between the metamict layer and the pristine crystal was selected from the HRTEM cross-section image of $Pb_2P_2O_7$ single crystal irradiated with P^+ ions to a fluence of $5\times10^{17}/m^2$ (Fig. 4-20). This fading of the Bragg reflections can be qualitatively understood by a simple two-cell model [26] as described in chapter 2.

The power spectra, Fig. 4-24, from the metamict state, Fig. 4-23, is uniform and completely aperiodic. The diffractogram essentially reproduces the TEM's contrast transfer function (CTF) which is being sampled nearly randomly. Fig. 4-22, neverthe-

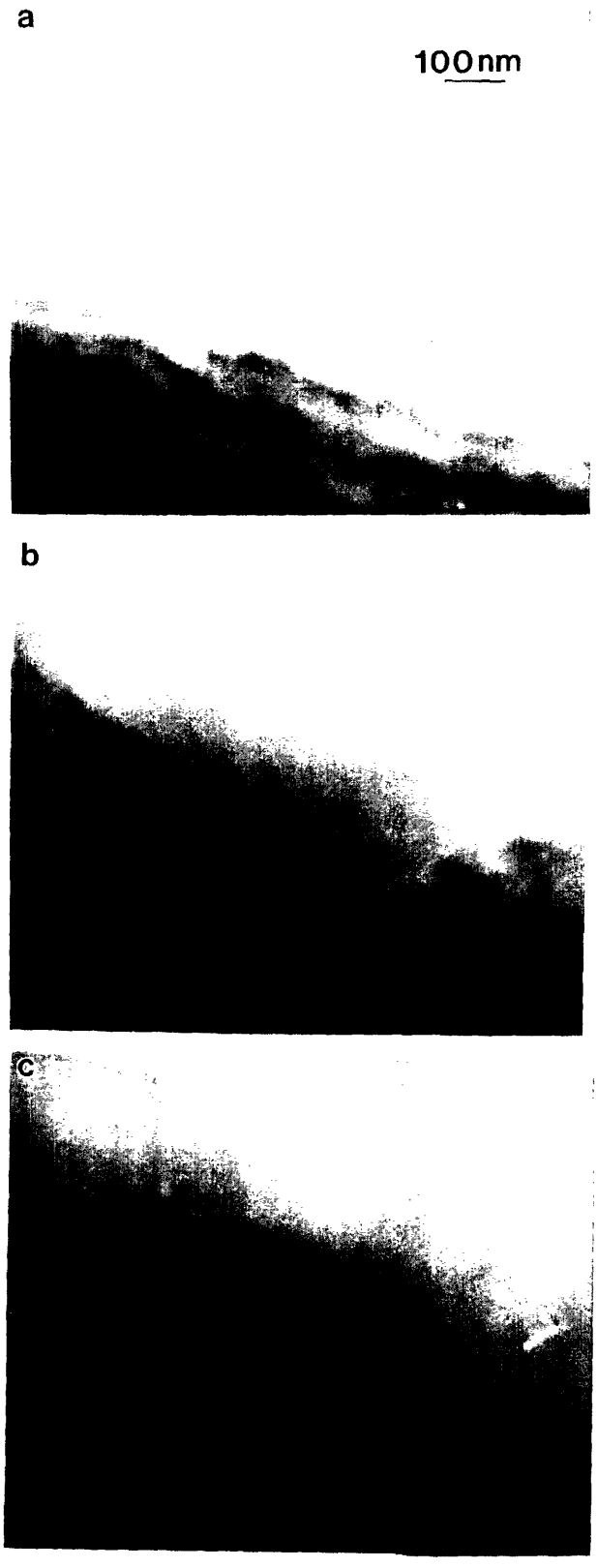

Figure 4-14: Expansion of amorphized $AlPO_4$ into crystalline material with 200 keV electrons.

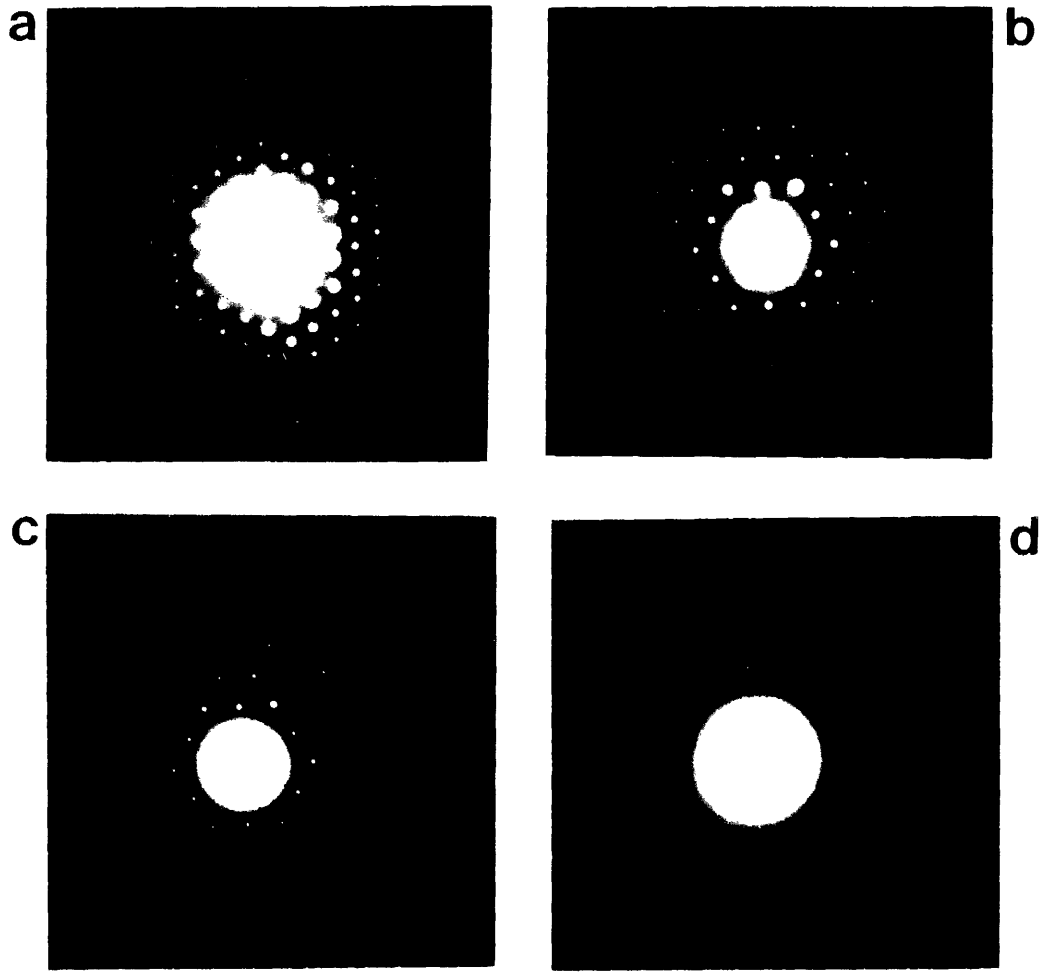

Figure 4-15: Amorphization of $AlPO_4$ with 200 keV electrons. (d) corresponds to $\sim 2 \times 10^{23}$ e/m^2 fluence.

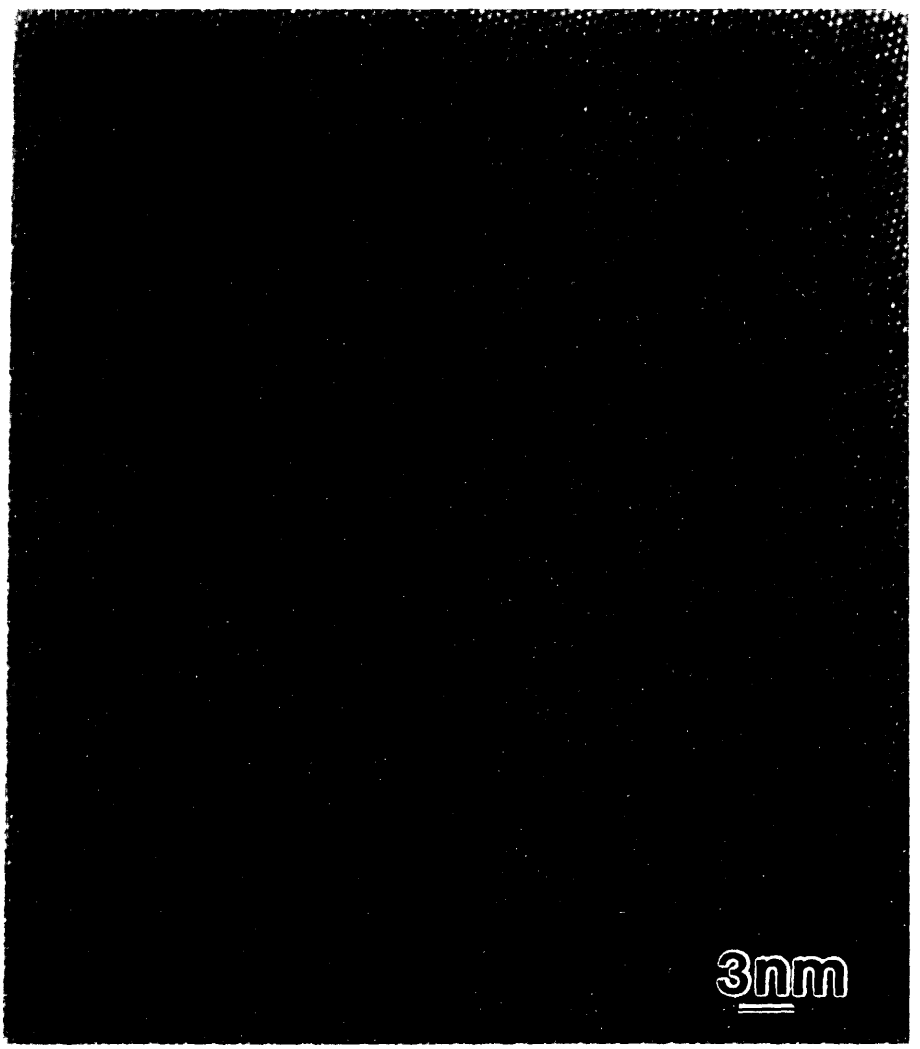

Figure 4-16: High resolution structure image of almost unirradiated $AlPO_4$.

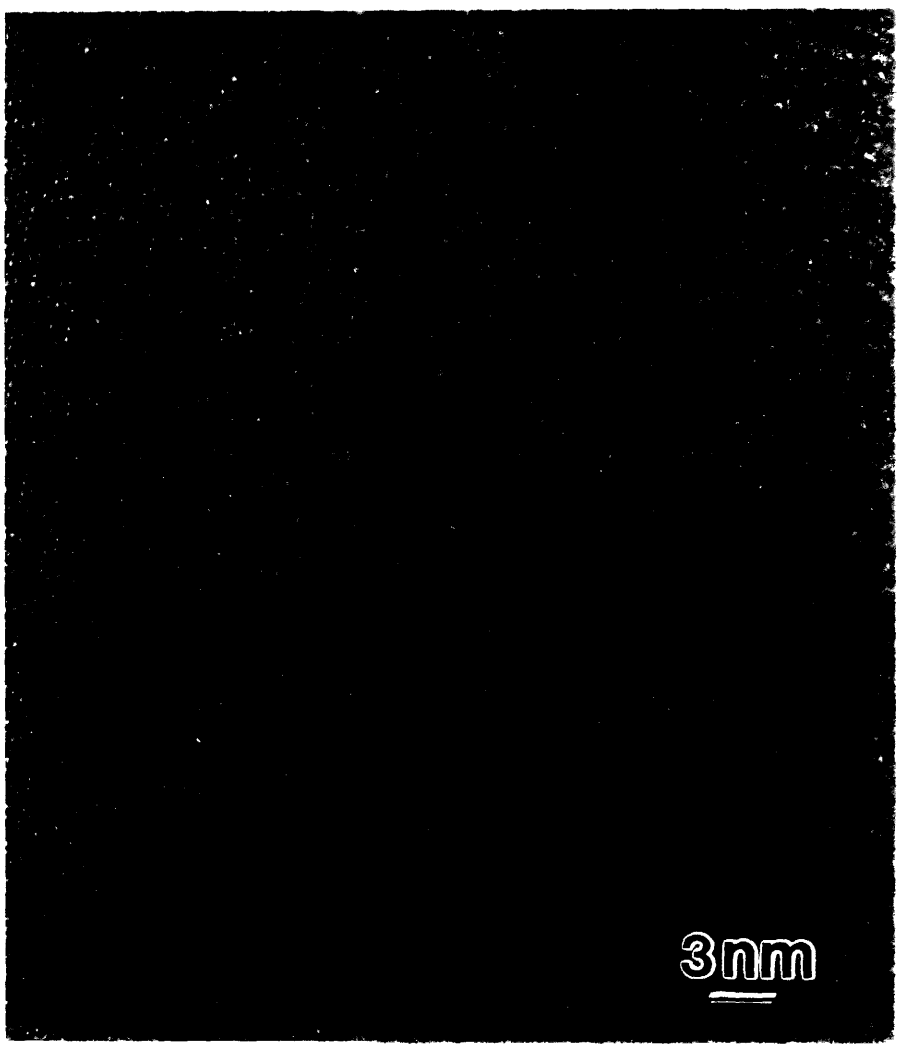

Figure 4-17: Initial structure image degradation during amorphization of $AlPO_4$ with 200 keV electrons. An amorphous front is sweeping from the right.

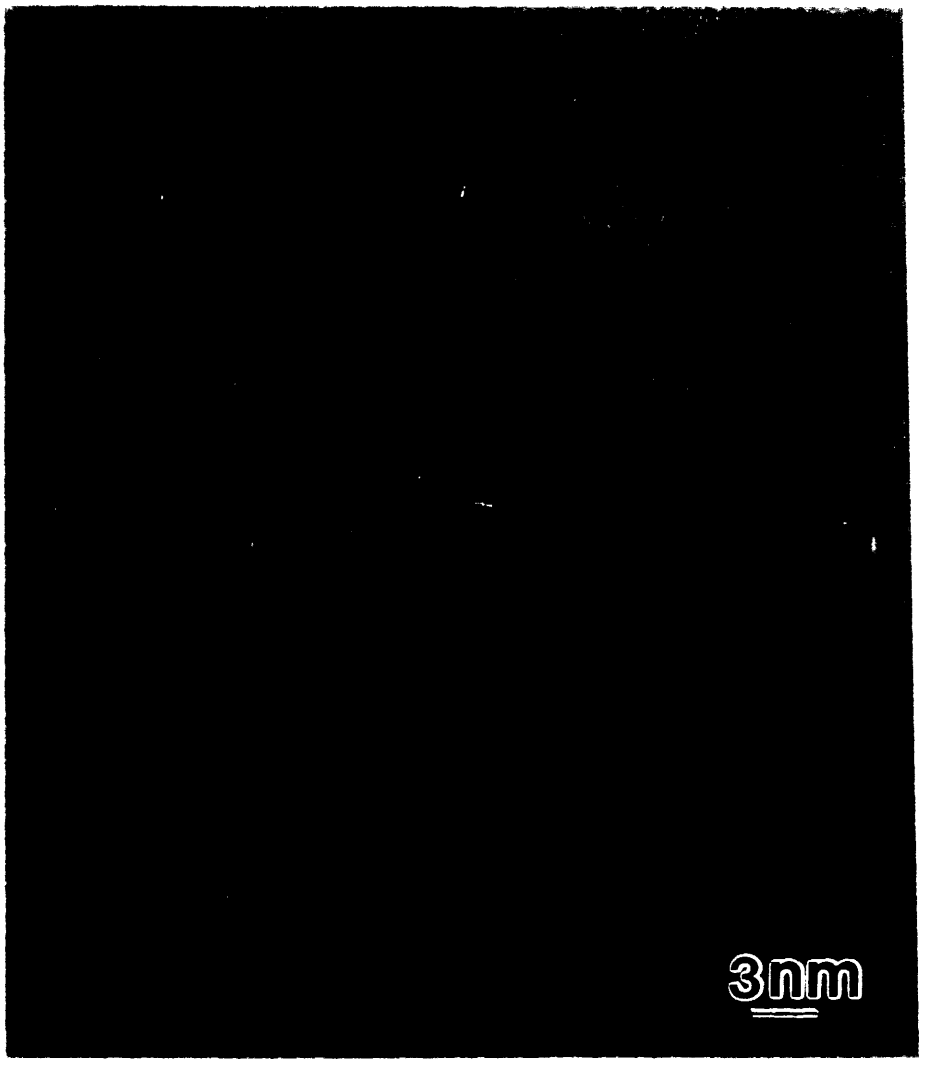

Figure 4-18: Initial structure image degradation during amorphization of $AlPO_4$ with 200 keV electrons showing incomplete amorphization.

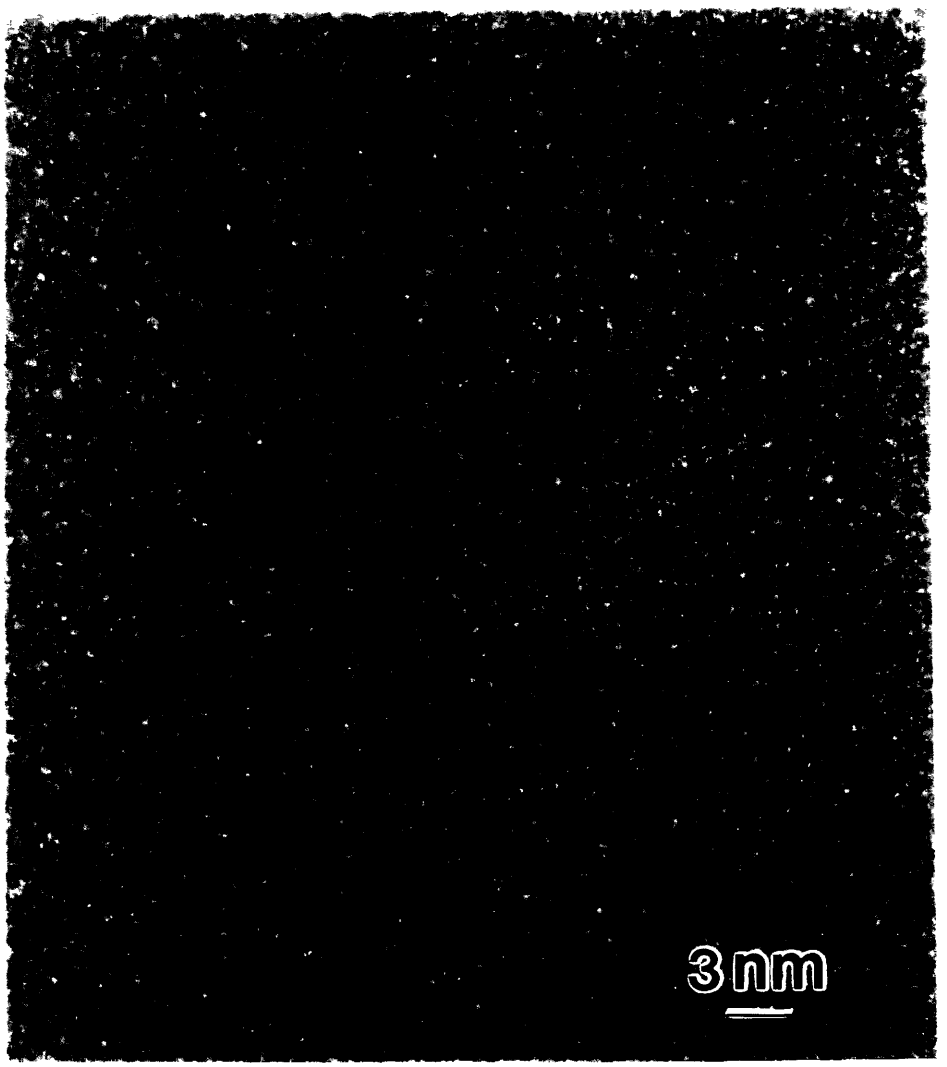

Figure 4-19: Completion of structure image degradation during amorphization of $AlPO_4$ with 200 keV electrons after $\sim 2 \times 10^{23}$ e/m^2.

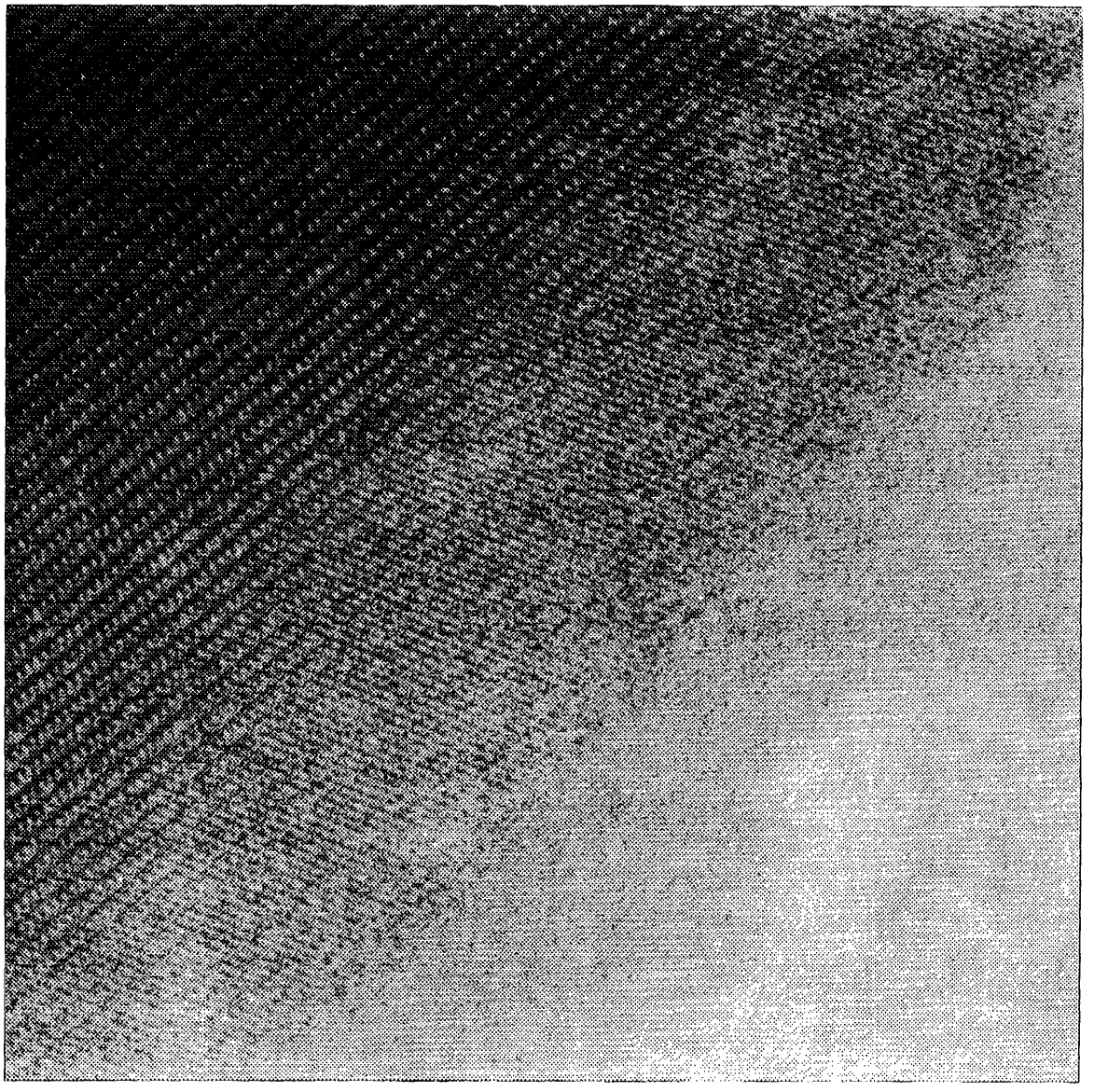

Figure 4-20: Digitized cross-section HRTEM image of $Pb_2P_2O_7$ single crystal irradiated with P^+ ions to a fluence of $5\times10^{17}/m^2$ with 1024×1024 resolution.

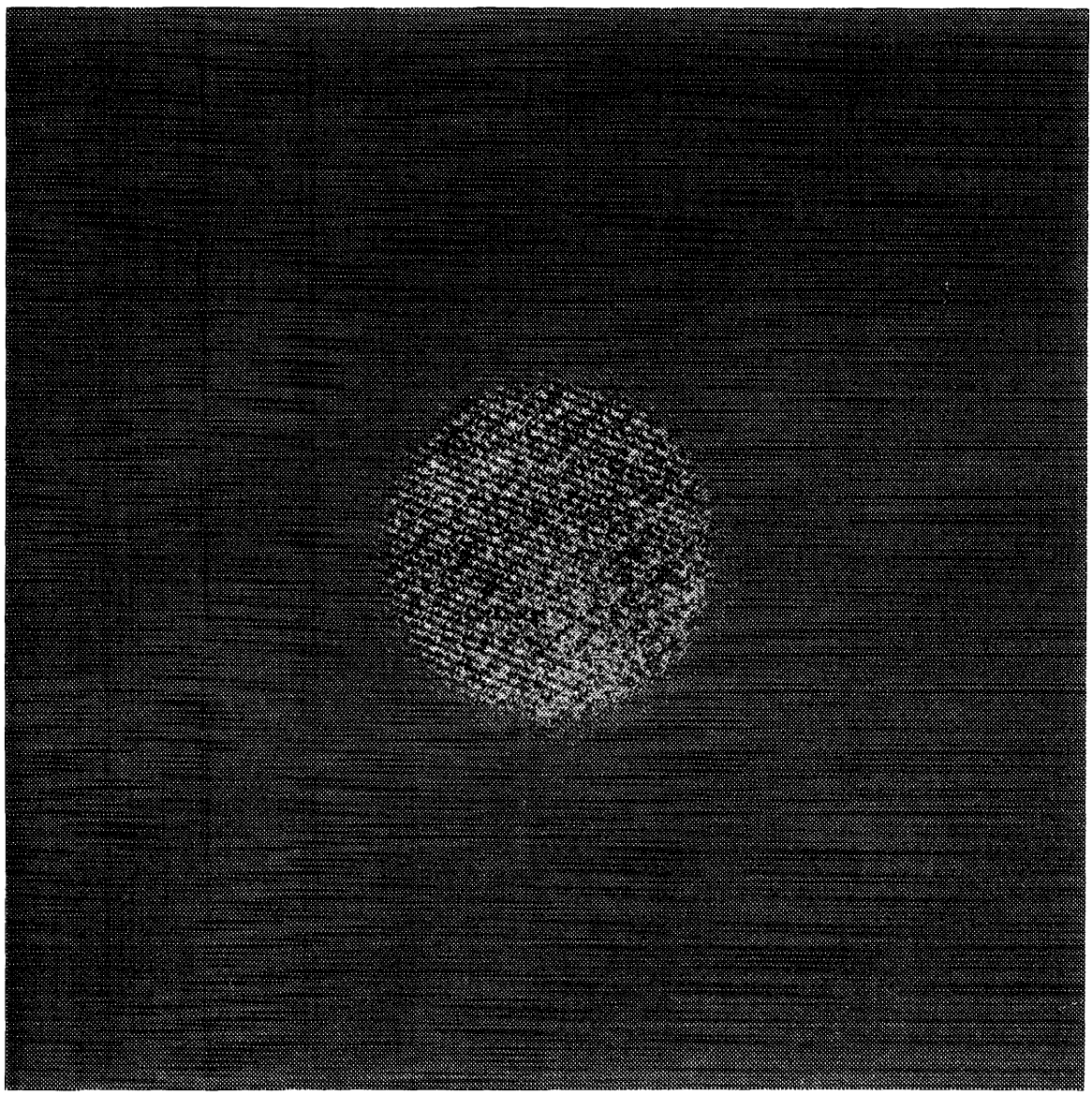

Figure 4-21: Interface between the pristine single crystal and the metamict layer selected from digitized cross-section HRTEM image of $Pb_2P_2O_7$ single crystal irradiated with P^+ ions to a fluence of $5\times10^{17}/m^2$.

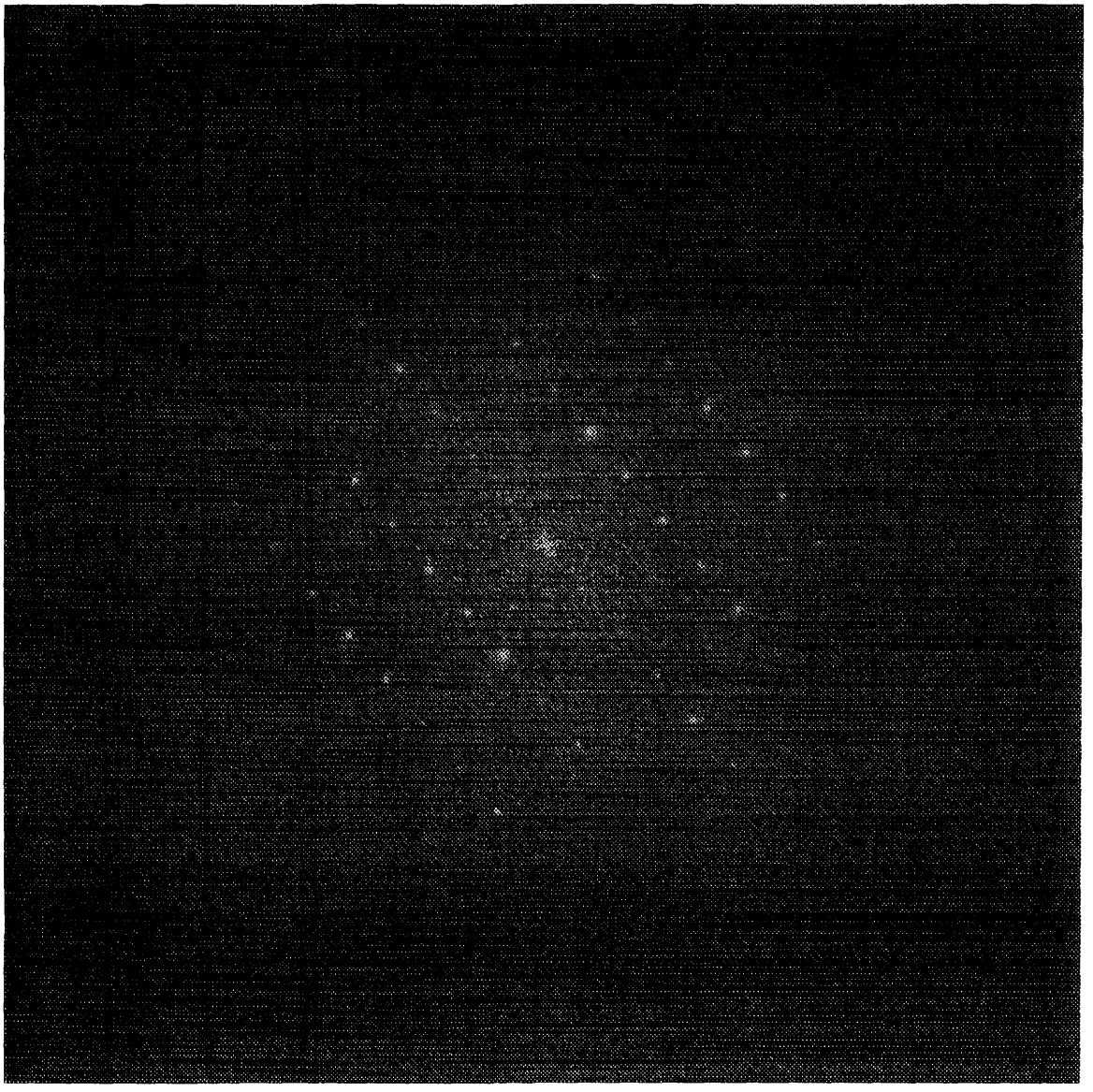

Figure 4-22: Digital diffractogram of the interface between the pristine single crystal and the metamict layer selected from digitized cross-section HRTEM image of $Pb_2P_2O_7$ single crystal irradiated with P^+ ions to a fluence of $5\times10^{17}/m^2$.

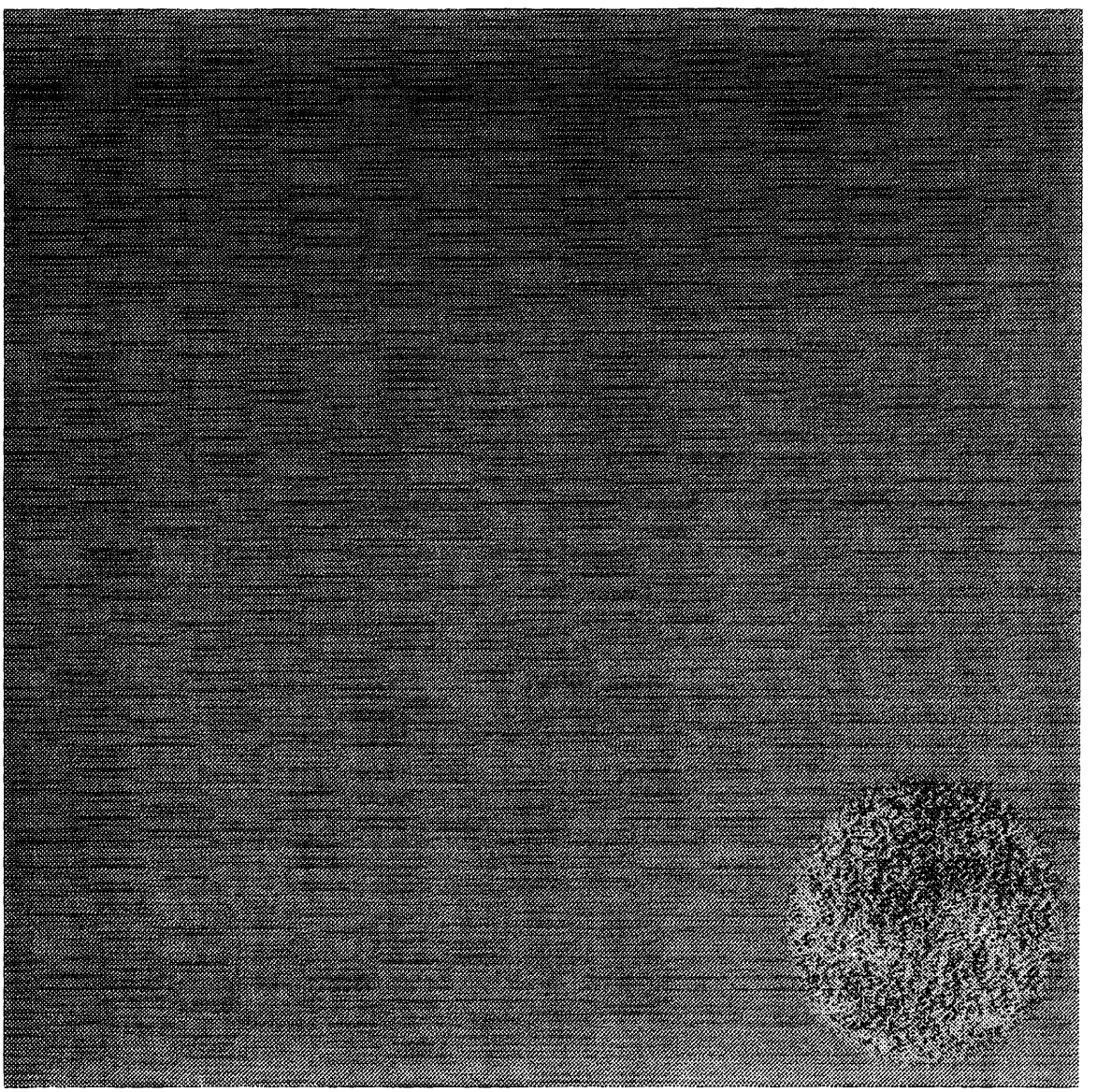

Figure 4-23: Small area from the metamict layer selected from digitized cross-section HRTEM image of $Pb_2P_2O_7$ single crystal irradiated with P^+ ions to a fluence of $5 \times 10^{17}/m^2$.

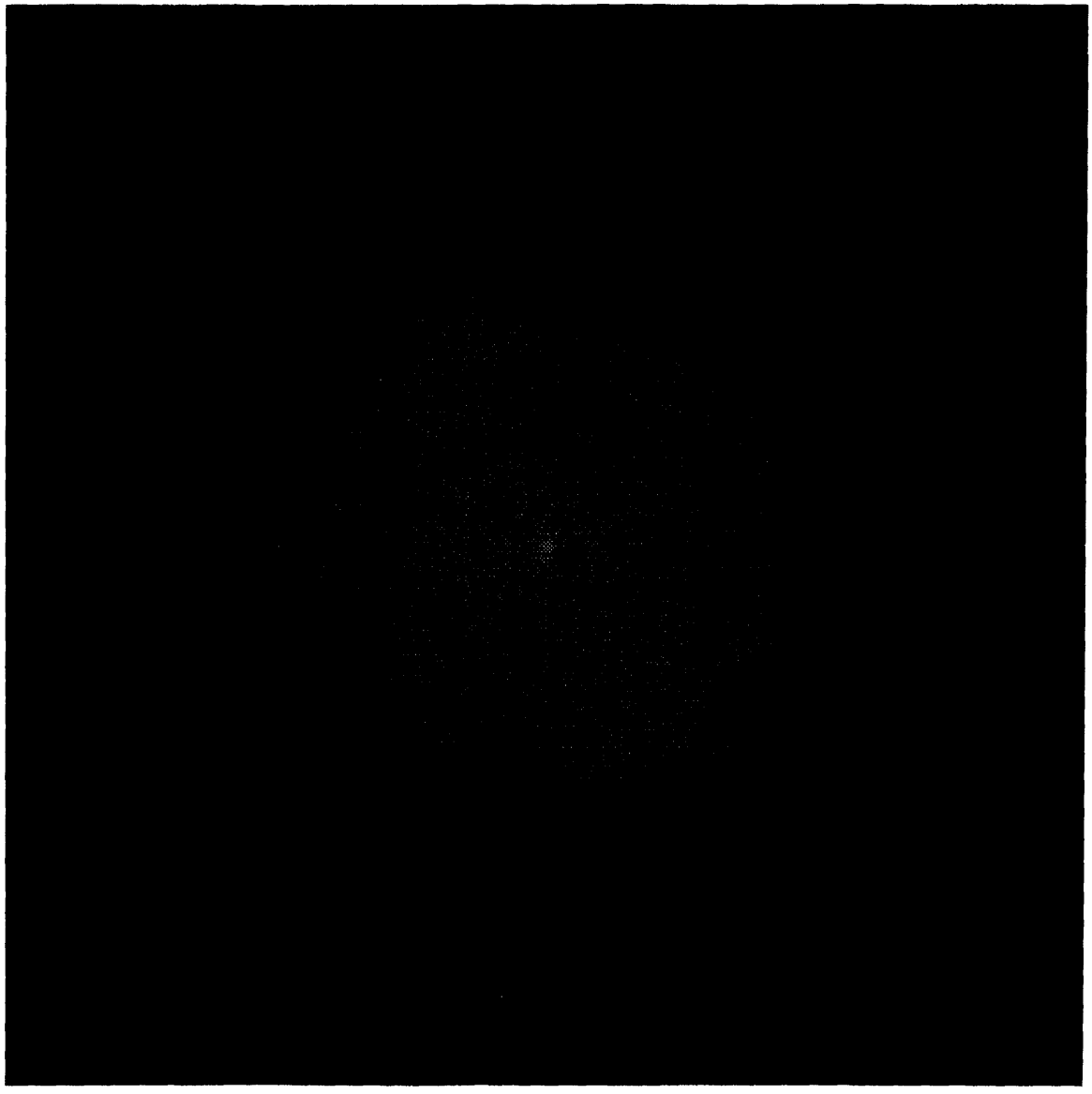

Figure 4-24: Digital diffractogram of the metamict region selected from digitized cross-section HRTEM image of $Pb_2P_2O_7$ single crystal irradiated with P^+ ions to a fluence of $5\times10^{17}/m^2$.

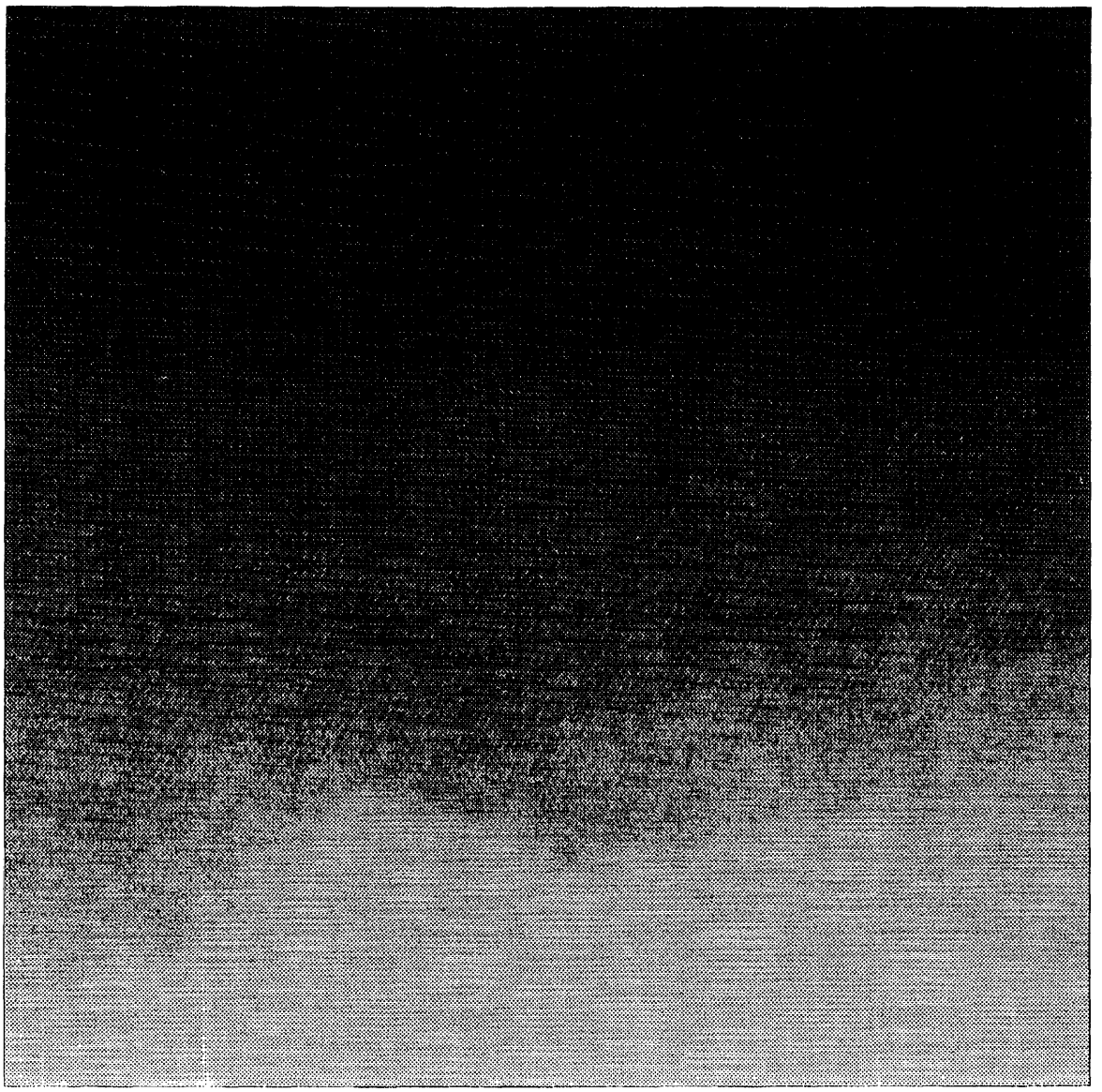

Figure 4-25: Digitized cross-section HRTEM image of $Pb_2P_2O_7$ single crystal irradiated with P^+ ions to a fluence of $1\times10^{18}/m^2$ with 1024×1024 resolution.

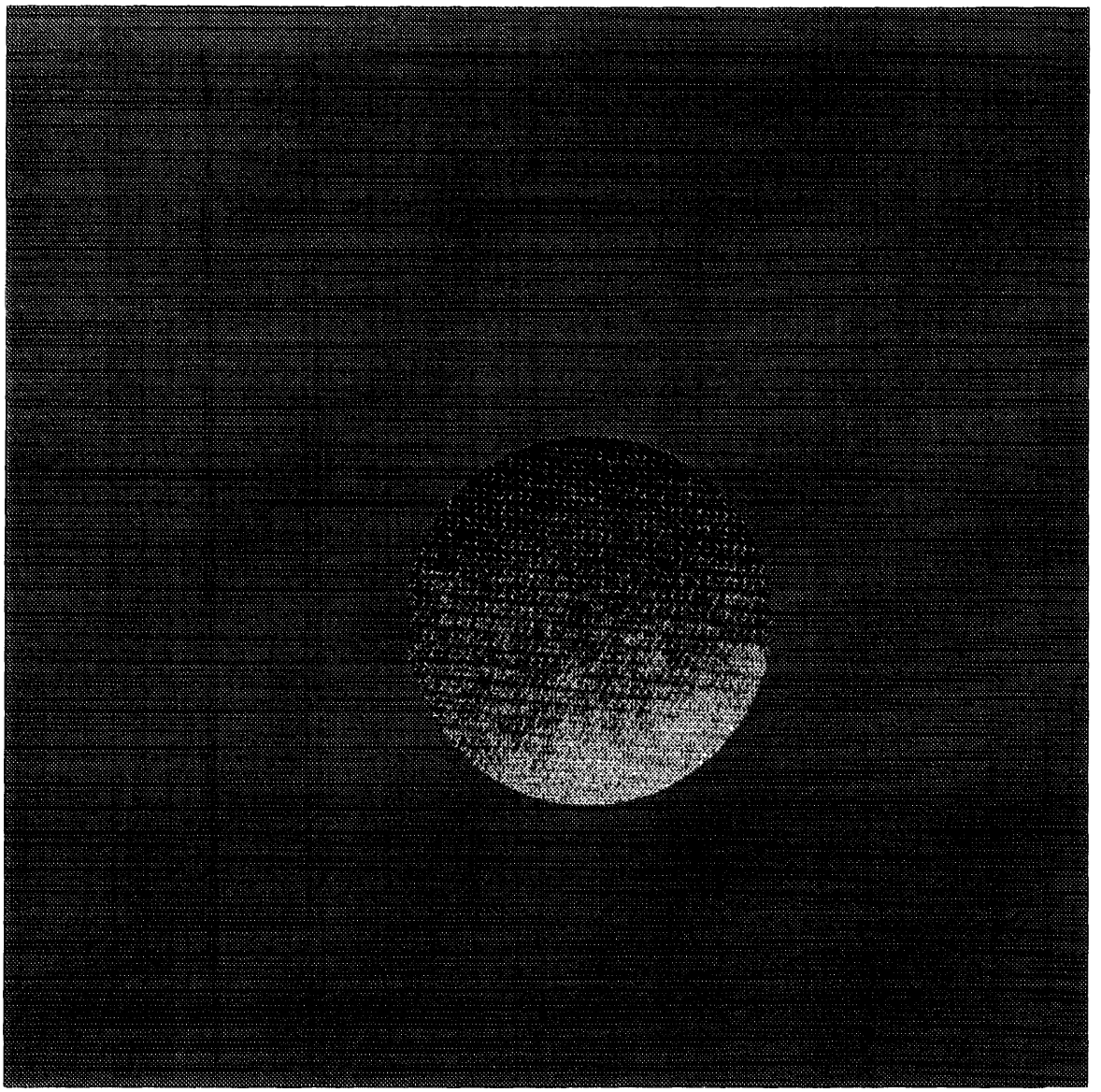

Figure 4-26: Interface between the pristine single crystal and the metamict layer selected from digitized cross-section HRTEM image of $Pb_2P_2O_7$ single crystal irradiated with P^+ ions to a fluence of $1\times10^{18}/m^2$.

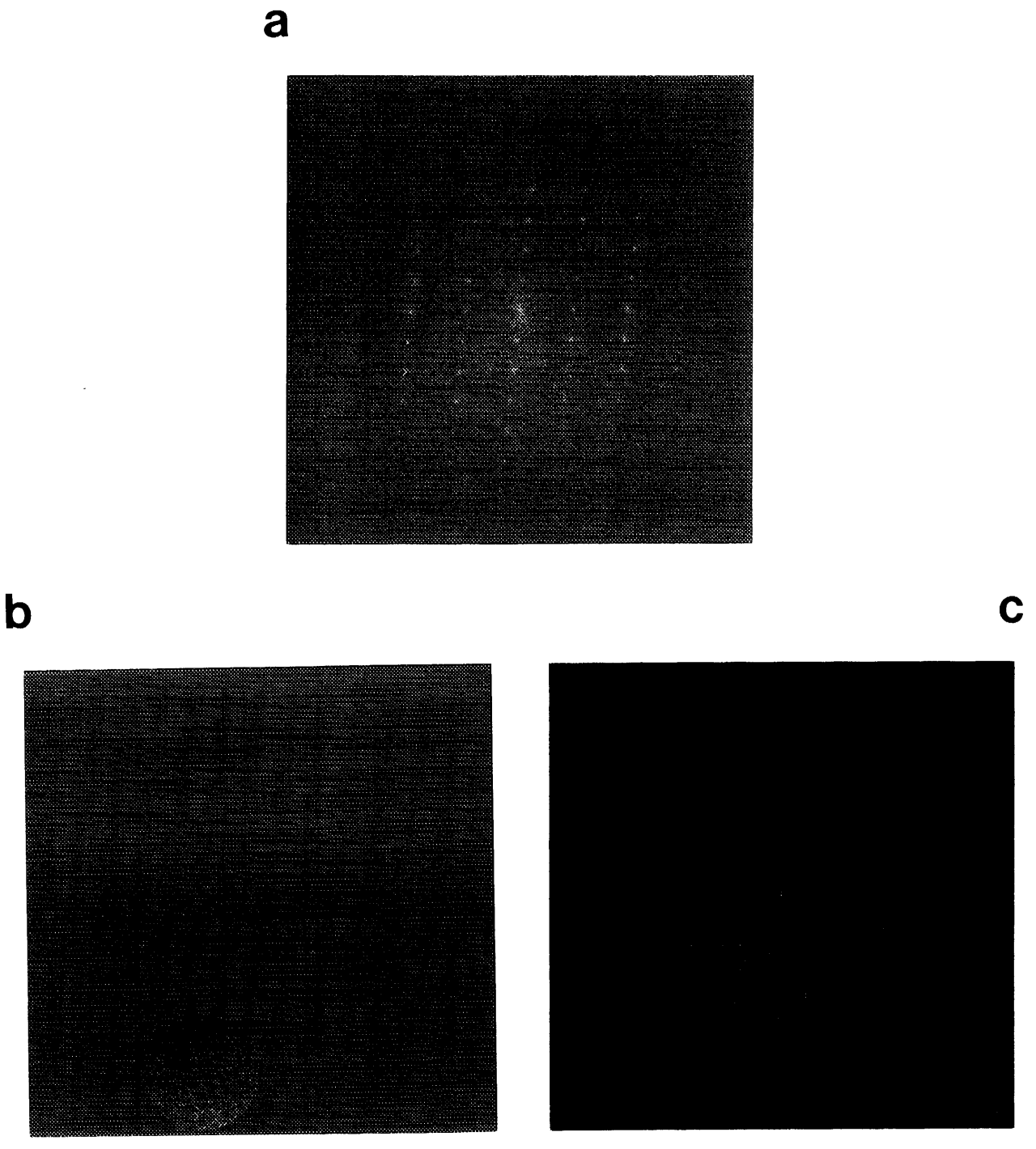

Figure 4-27: (a) Digital diffractogram of the interface between the pristine single crystal and the metamict layer. (b) Small area from the metamict layer and (c) digital diffractogram of (b). Irradiation fluence of P^+ ions was $1\times10^{18}/m^2$.

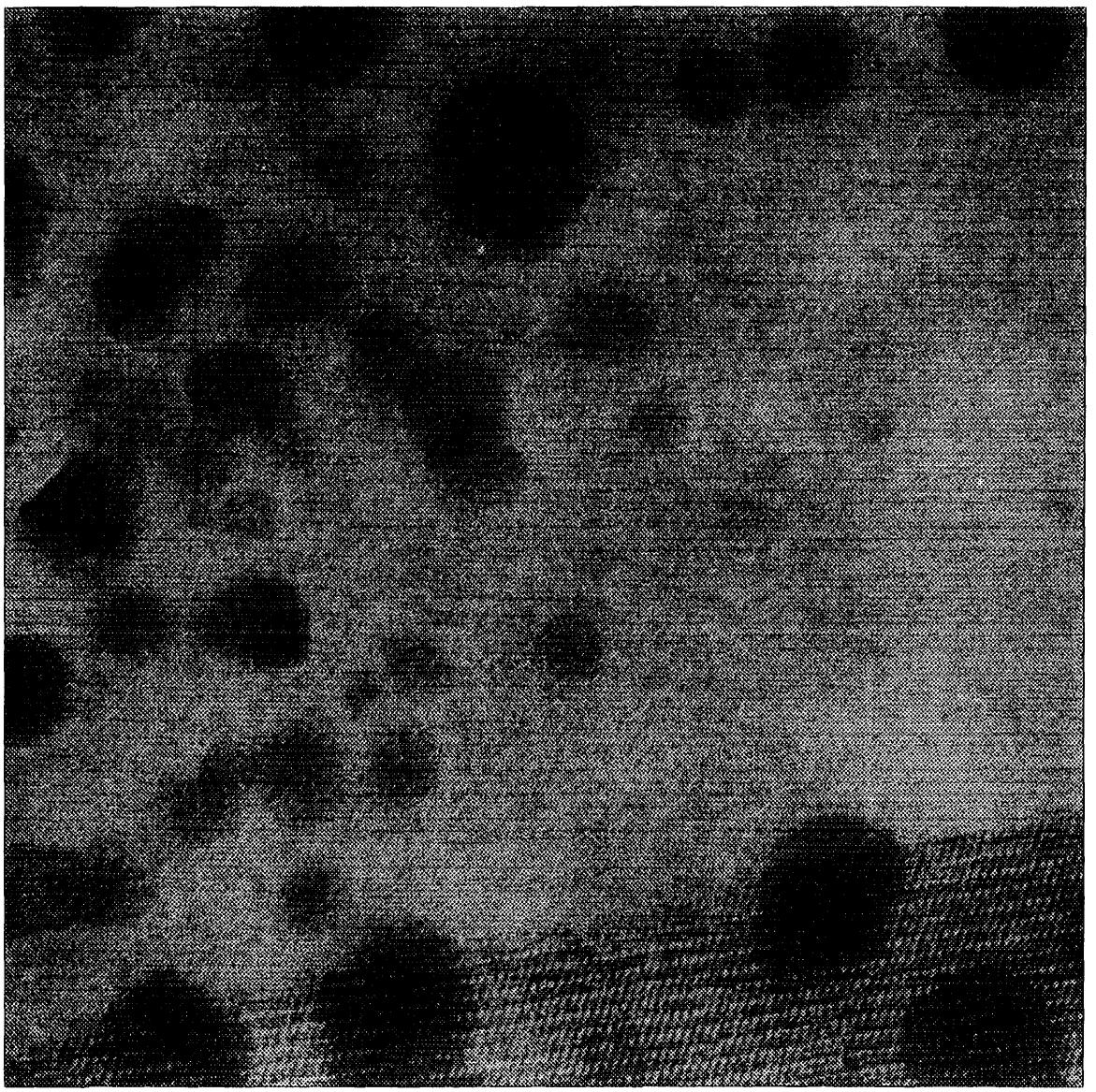

Figure 4-28: Digitized cross-section HRTEM image of $Pb_2P_2O_7$ single crystal irradiated with P^+ ions to a fluence of $5\times10^{19}/m^2$ with 1024×1024 resolution.

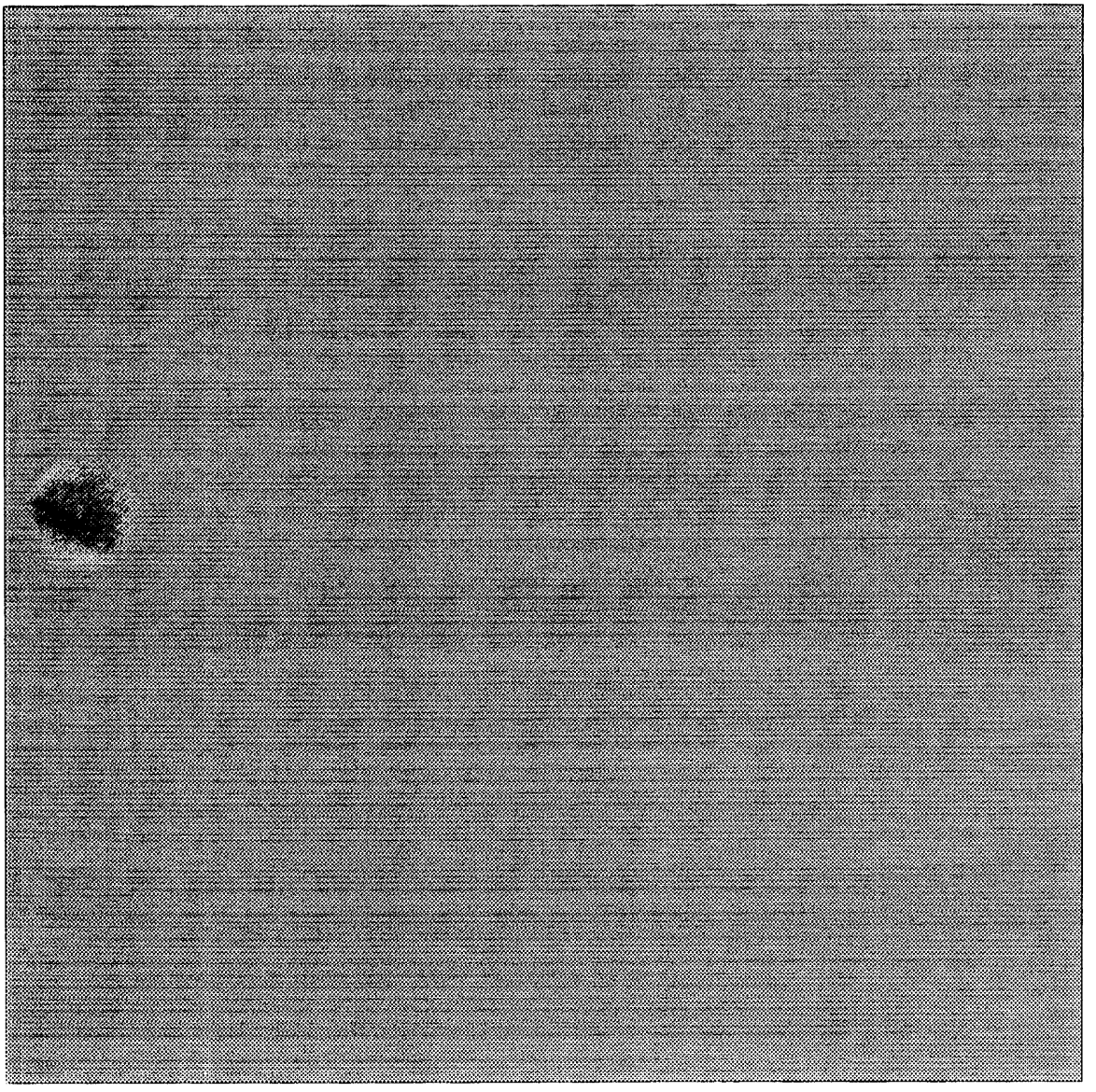

Figure 4-29: Small area from the metamict layer selected from digitized cross-section HRTEM image of $Pb_2P_2O_7$ single crystal irradiated with P^+ ions to a fluence of $5\times10^{19}/m^2$.

Figure 4-30: Digital diffractogram of the metamict region selected from digitized cross-section HRTEM image of $Pb_2P_2O_7$ single crystal irradiated with P^+ ions to a fluence of $5\times10^{19}/m^2$ showing Bragg reflections corresponding to [110] Pb and also the amorphous diffuse background.

less, does not show any 'new' or anomalous Bragg reflections, indicating that metamictization has occurred without crystallization of any intermediate phases. Similar results were also seen for $Pb_2P_2O_7$ single crystal irradiated with P^+ ions to a fluence of $1\times10^{18}/m^2$, Figs. 4-25 through 4-27.

For the metamict state achieved by the irradiating the $Pb_2P_2O_7$ single crystals to a fluence of $5\times10^{19}P^+/m^2$, where a very sharp interface develops between the metamict layer and the pristine single crystal occurs (discussed earlier in the chapter), the anomaly (darker regions) was further analyzed using digital diffractometry. Fig. 4-29 was selected from the digitized image Fig. 4-28 and the computed diffractogram shown in Fig. 4-30 gives the Bragg reflections corresponding to [110] Pb superimposed over the amorphous diffuse background. However, diffractograms from any other such 'dark' regions selected from Fig. 4-28 did not result in these reflections. The absence of such Bragg reflections could also occur if the Pb fringes were not in focus for the other dark regions in the metamict zone. This result confirms our earlier conclusion that the origin of these dark regions lies mainly in sample preparations during single crystal growth (excess Pb content) and perhaps also due to surface modifications during ion-beam thinning. The second cause is less likely, however, as no other P^+ irradiated single crystals (all prepared from different batches during crystal growth) displayed these features.

4.1.4 Energy-Filtered Electron Diffraction (Electron Amorphography)

Energy-filtered electron diffraction patterns for glassy and metamict phosphates were collected in selected-area diffraction mode, as described in Chap. 2. Fig. 4-31 shows scattered intensity data along a radial direction obtained by performing a line scan of the two-dimensional energy-filtered diffraction data for three thermally quenched and annealed lead phosphate glasses with increasing lead content. The first sharp

peak, known as the first sharp diffraction peak (FSDP), occurs at $\sim$ 3.56 nm^{-1} for the lead metaphosphate glass, at $\sim$ 3.71 nm^{-1} for lead pyrophosphate glass and at $\sim$ 3.85 nm^{-1} for an intermediate $1.4PbO{\cdot}P_2O_5$ glass, corresponding to a real-space correlation distance of $\sim$ 0.28 nm, $\sim$ 0.27nm and $\sim$ 0.26 nm respectively. FSDPs are a characteristic of all thermally quenched and annealed glasses and glass systems and are believed to be the signature of medium range order in glasses [110, 111]. However, for P^+ ion-implanted lead phosphate glasses and lead pyrophosphate crystals, the intensity of FSDP is severely diminished [112], see Fig. 4-32 and 4-33. Such modifications in FSDP are indicative of changes in atomic arrangements in the medium range [112, 130].

More recently, Elliott [113]-[115] has ascribed the origin of the FSDP in the structure factor of glasses to a chemical-order pre-peak associated with the ordering of interstitial voids around the cation-centered clusters in the structure. He insists that the FSDP intensity of a covalent glass (chalcogenide) decreases markedly upon addition of network modifying atoms (alkali elements), which occupy the largest of interstitial voids in the frame-work structure. Although, a $2{\times}10^{20}/m^2$ P^+ implant dose corresponds to a change in P composition at the implant profile peak to less than 1%, the addition is perhaps sufficient to change significantly the medium-range order.

This is confirmed by looking at the reconstructed RDFs for $Pb_2P_2O_7$ single crystals ion-irradiated to the increasing P^+ dose depicted in Fig. 4-34, and for the unimplanted and implanted glasses shown in Fig. 4-35 and Fig. 4-36. For all the metamict phosphates studied, and for the unimplanted glasses, the short-range order (position of the first peak in the RDF, which represents the P-O correlations in the $[PO_4]$ tetrahedron) is preserved and occurs at 0.157 nm. This distance is in fair agreement with with the P-O correlations reported for lime phosphate glasses by Biscoe *et al.* [18], who report it to be 0.157 nm and by Wingall *et al.* [19], who report it to be 0.16 nm. However, for the higher dose of P^+ ion implantation ($2x10^{20}/m^2$), the near-

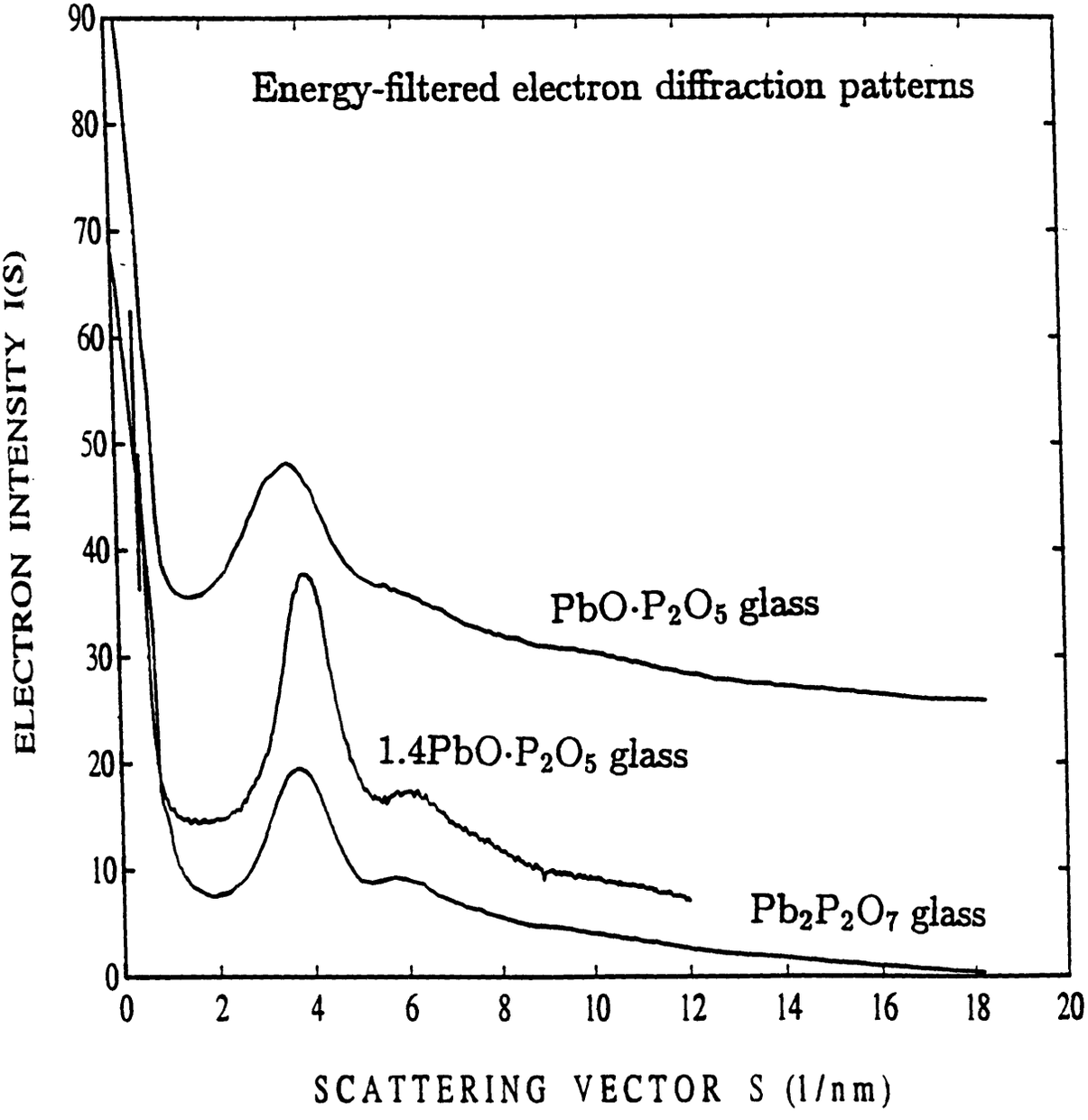

Figure 4-31: Energy-filtered electron diffraction line scan data for three lead phosphate glasses.

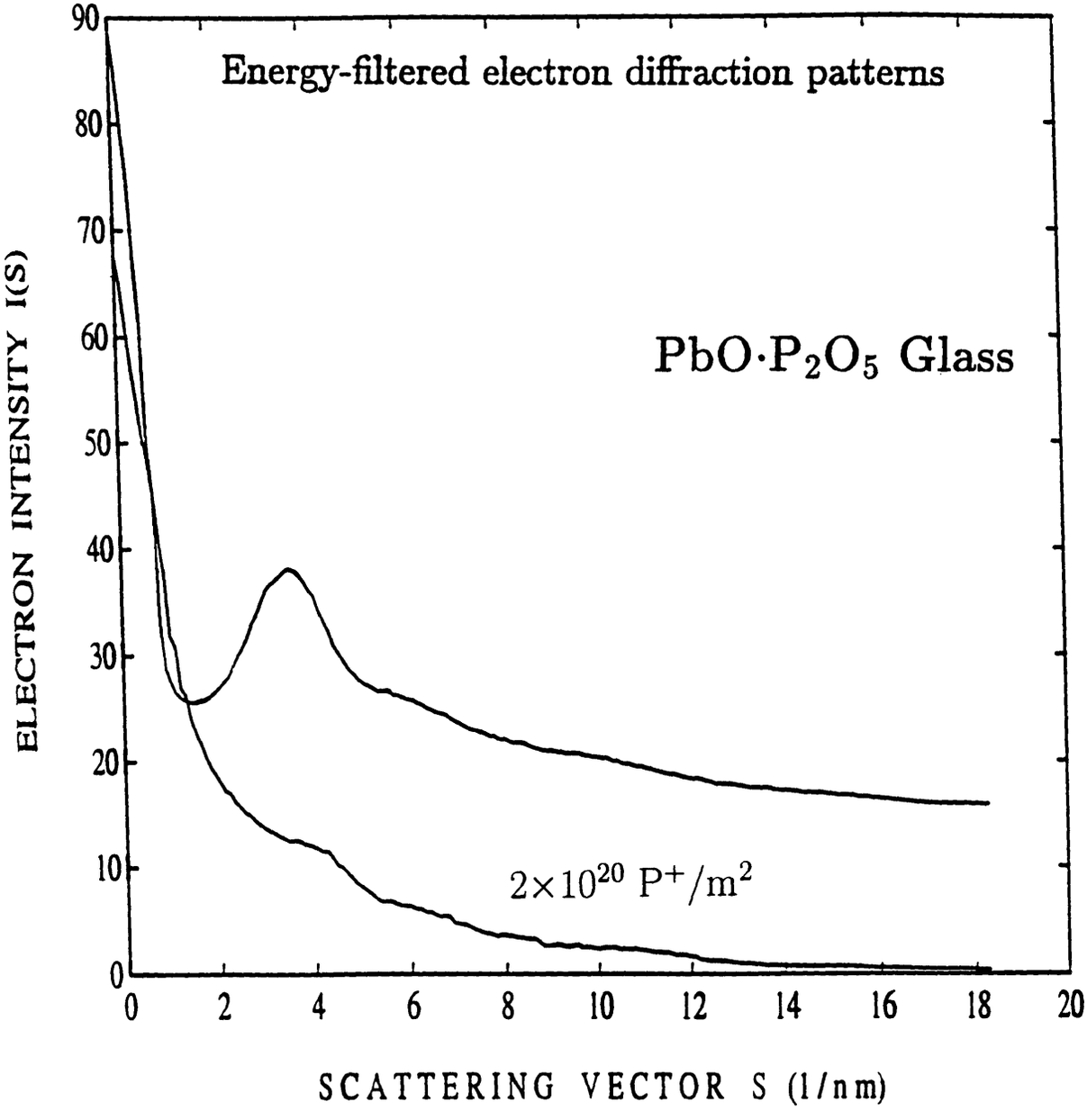

Figure 4-32: Energy-filtered electron diffraction line scan data for the $PbO{\cdot}P_2O_5$ glass and P^+ ion-irradiated $PbO{\cdot}P_2O_5$ glass with ion-fluence of $2{\times}10^{20}/m^2$.

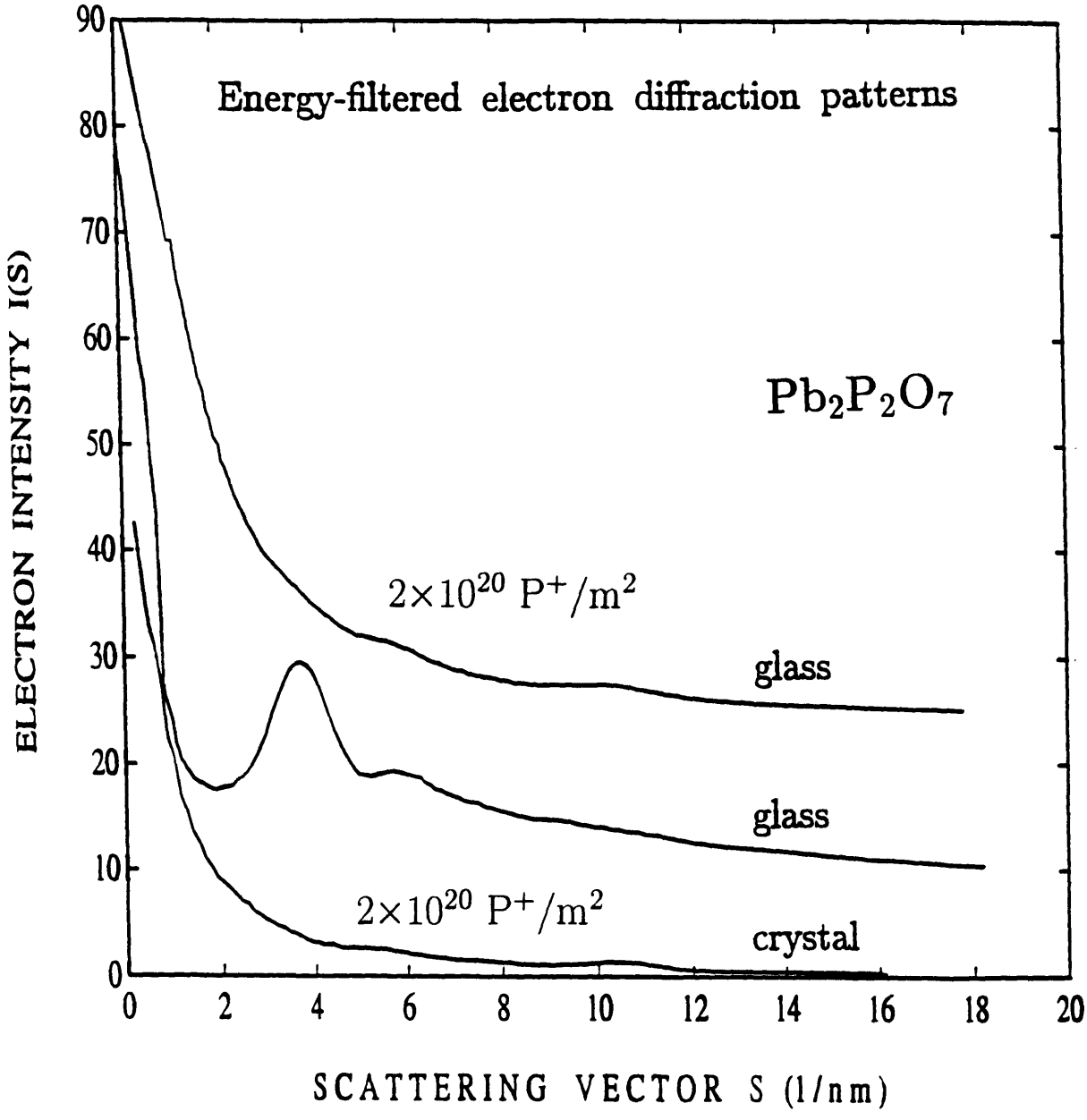

Figure 4-33: Energy-filtered electron diffraction line scan data for the $Pb_2P_2O_7$ P^+ ion-irradiated glass, $Pb_2P_2O_7$ glass and $Pb_2P_2O_7$ single crystal. The ion fluence of P^+ was $2\times10^{20}/m^2$.

medium-range order (0.2-0.5 nm correlations) is altered, indicated by a significant shift in the position of the second peak, which seems more like an envelope of the second and third peaks in the RDFs for lower-dose irradiations. Such an alteration of near-medium-range order (at high fluence) suggests that the metamict state so obtained is more 'disordered' than the conventionally prepared (thermally-quenched) glasses. Also, for the same high fluence, the metamict states generated from the lead pyrophosphate glasses and single crystals differ significantly at near-medium-range and medium-range. Again, significant changes for these metamict states generated by such heavy ion-irradiation were manifest in the phase-separated regions (discussed earlier in this chapter) that occurred. Although the scale of such phase-separated regions were around the 2 nm range, it is not yet fully understood how the phase separation would result in significant changes to the 0.2-0.5 nm atom-atom correlations.

4.2 High-Performance Liquid Chromatography

High-performance liquid chromatography experiments were performed for the metamict lead phosphates to explore the degree of polymerization in these materials, which can provide information complementary to the atomic correlations embodied in the RDFs. Fig. 4-37 and Fig. 4-38 show the chromatograms for P^+ implanted $Pb_2P_2O_7$ single crystals and glasses respectively and Fig. 4-39 that for O^+ implanted $Pb_2P_2O_7$ glasses. A general conclusion that can be readily drawn is the fact that the degree of polymerization increases with the increasing ion fluence, as indicated by the increase in the peak heights of P_4 and higher order $[PO_4]$ tetrahedral chains. This polymerization can be viewed as a change in the medium-range order which is manifested as a change (increase) in the peak heights of the longer chains.

A more detailed analysis is given by Sales and coworkers [68], which we will follow to explain the structural differences in these metamict phosphates in lieu of chromatography data. Parks and Van Wazer [116], using Flory's theory [117] to describe the polymerization in phosphate glasses, predict that the weight fraction

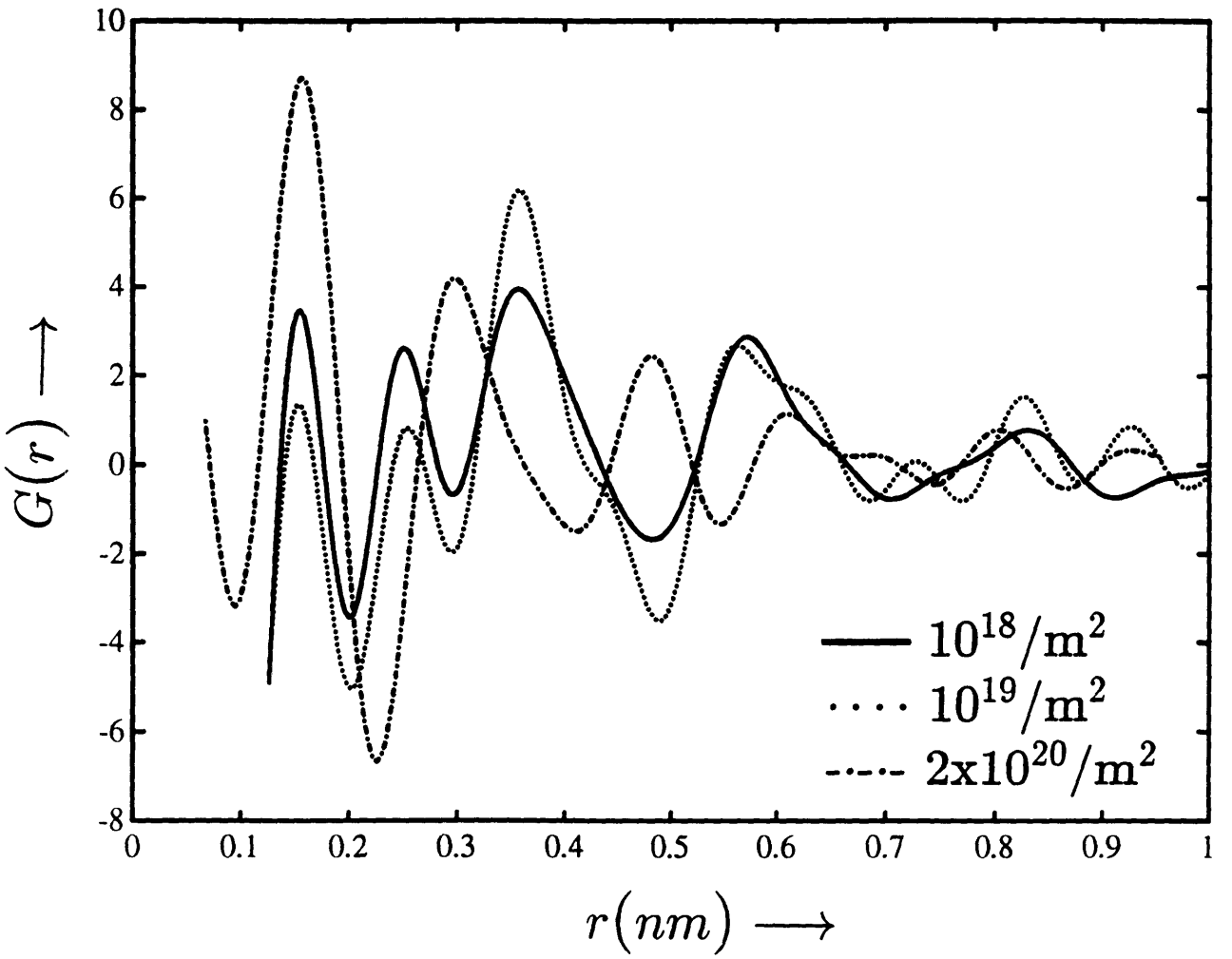

Figure 4-34: Reconstructed RDFs for three different P^+ fluences for lead pyrophosphate single crystals.

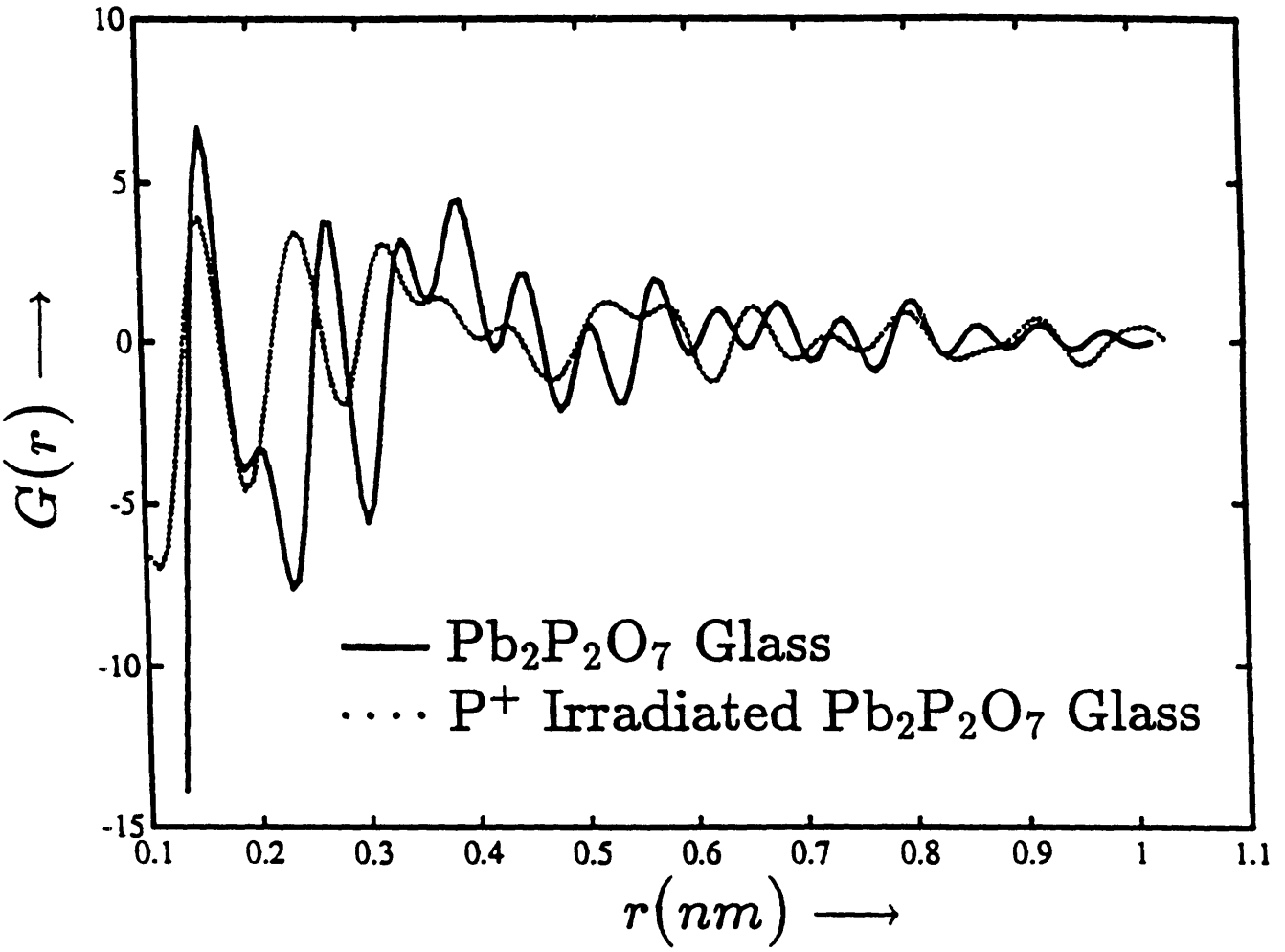

Figure 4-35: Comparision of reconstructed RDFs for unirradiated and P^+ irradiated lead pyrophosphate glass. The P^+ irradiation fluence was $2\times10^{20}/m^2$.

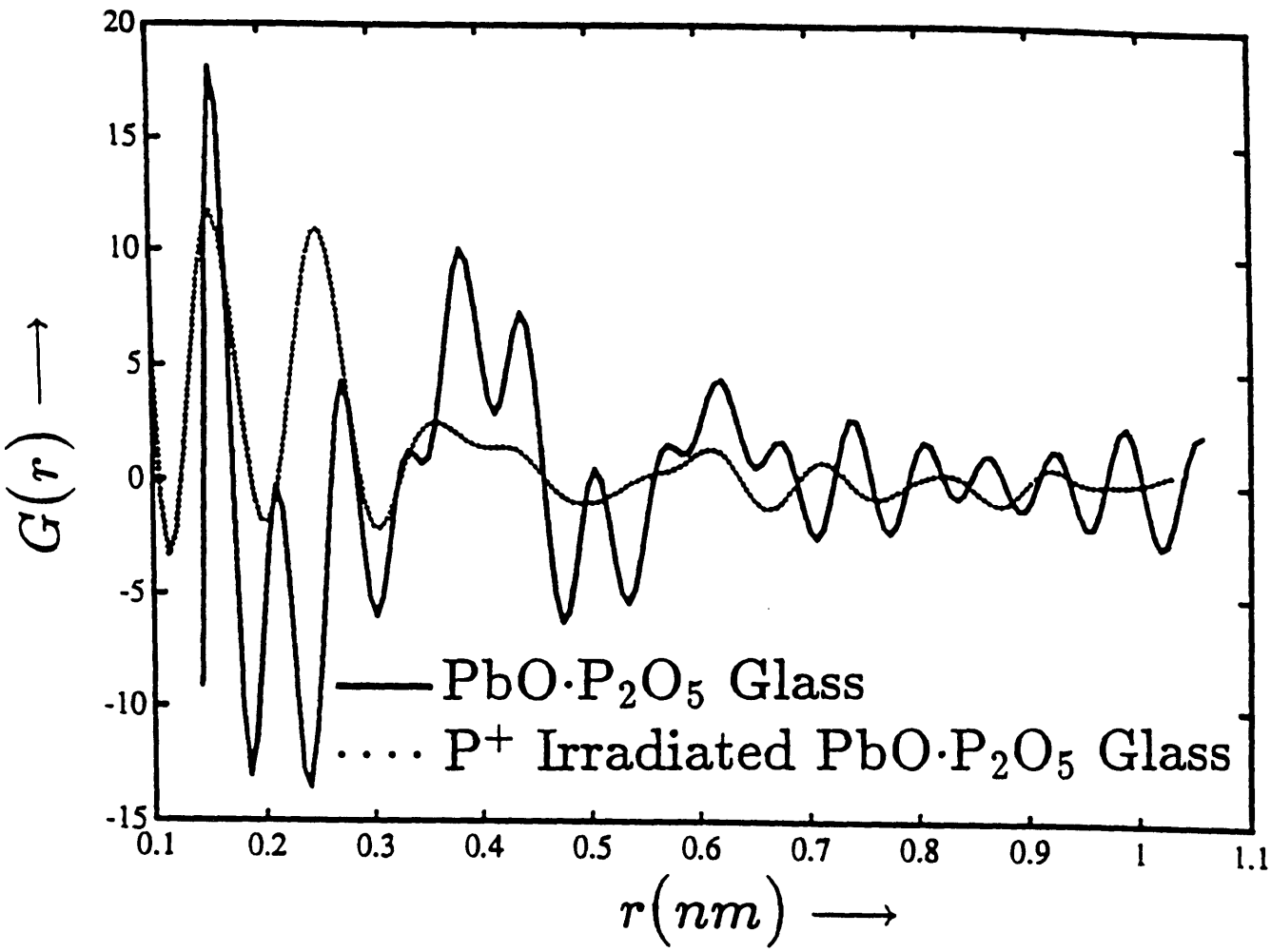

Figure 4-36: Comparision of reconstructed RDFs for unirradiated and P^+ irradiated lead metaphosphate glass. The P^+ irradiation fluence was $2\times10^{20}/m^2$.

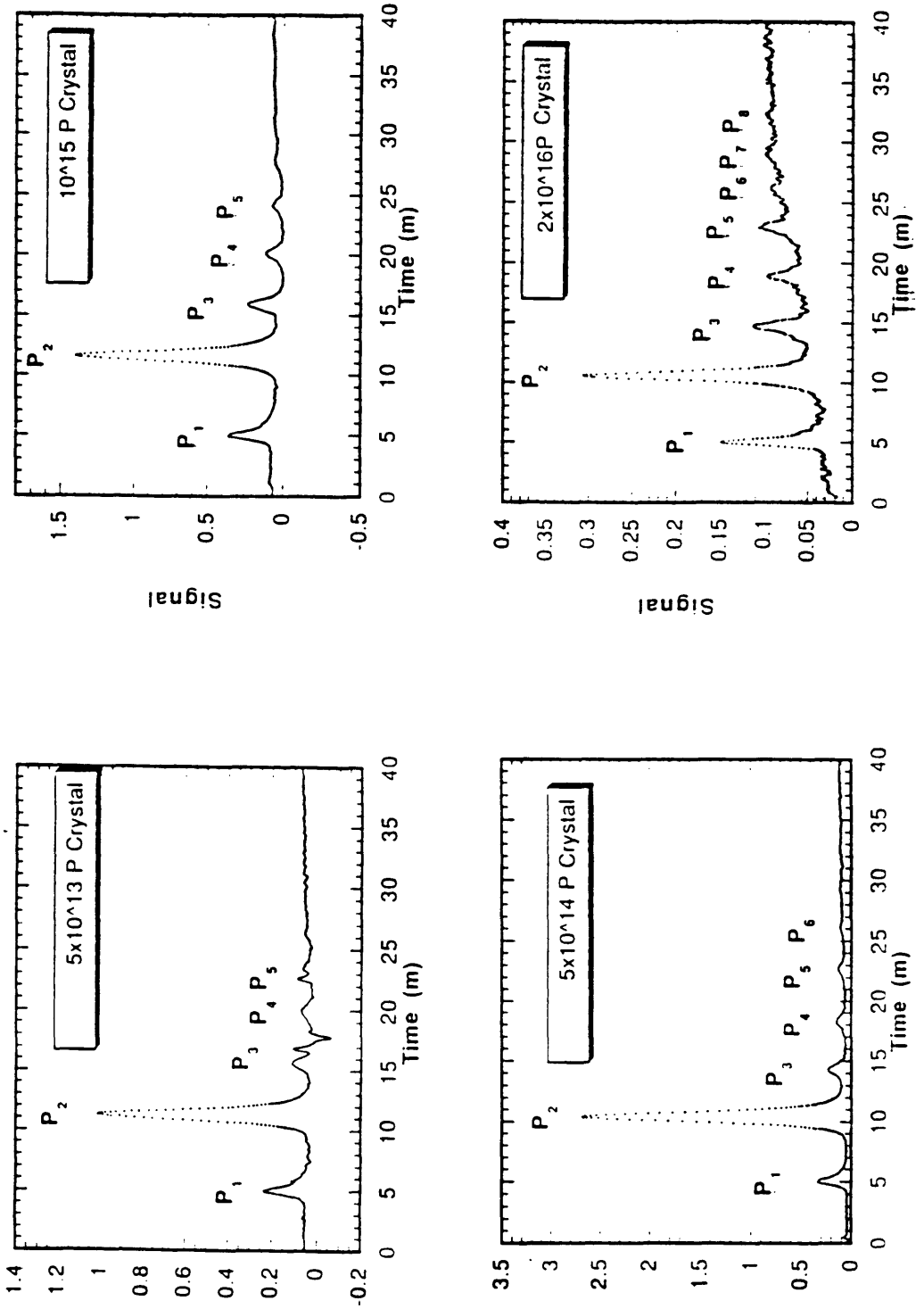

Figure 4-37: HPLC chromatograms for P^+ ion-irradiated $Pb_2P_2O_7$ single crystals. Note that the ion-fluence indicated is in $\#/cm^2$.

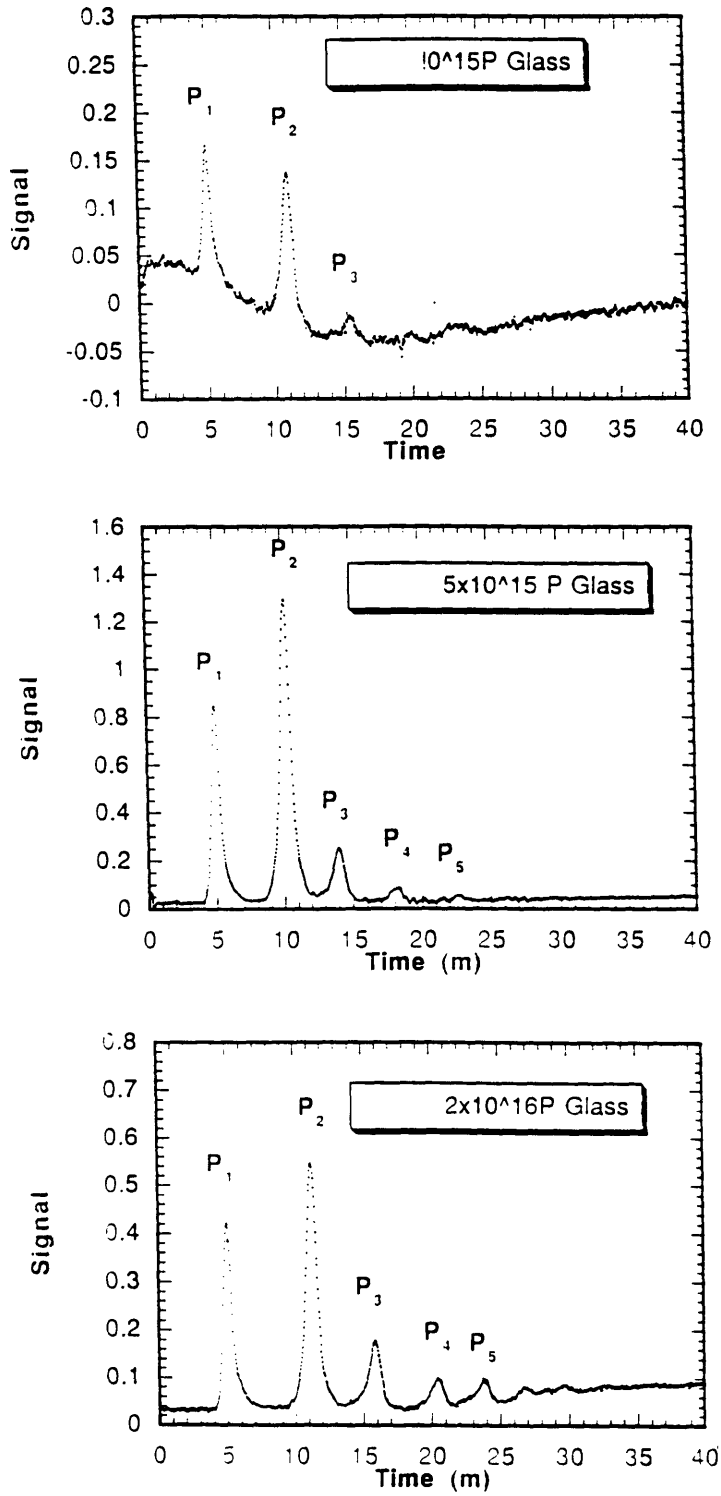

Figure 4-38: HPLC chromatograms for P^+ ion-irradiated $Pb_2P_2O_7$ glasses. Note that the ion-fluence indicated is in $\#/cm^2$.

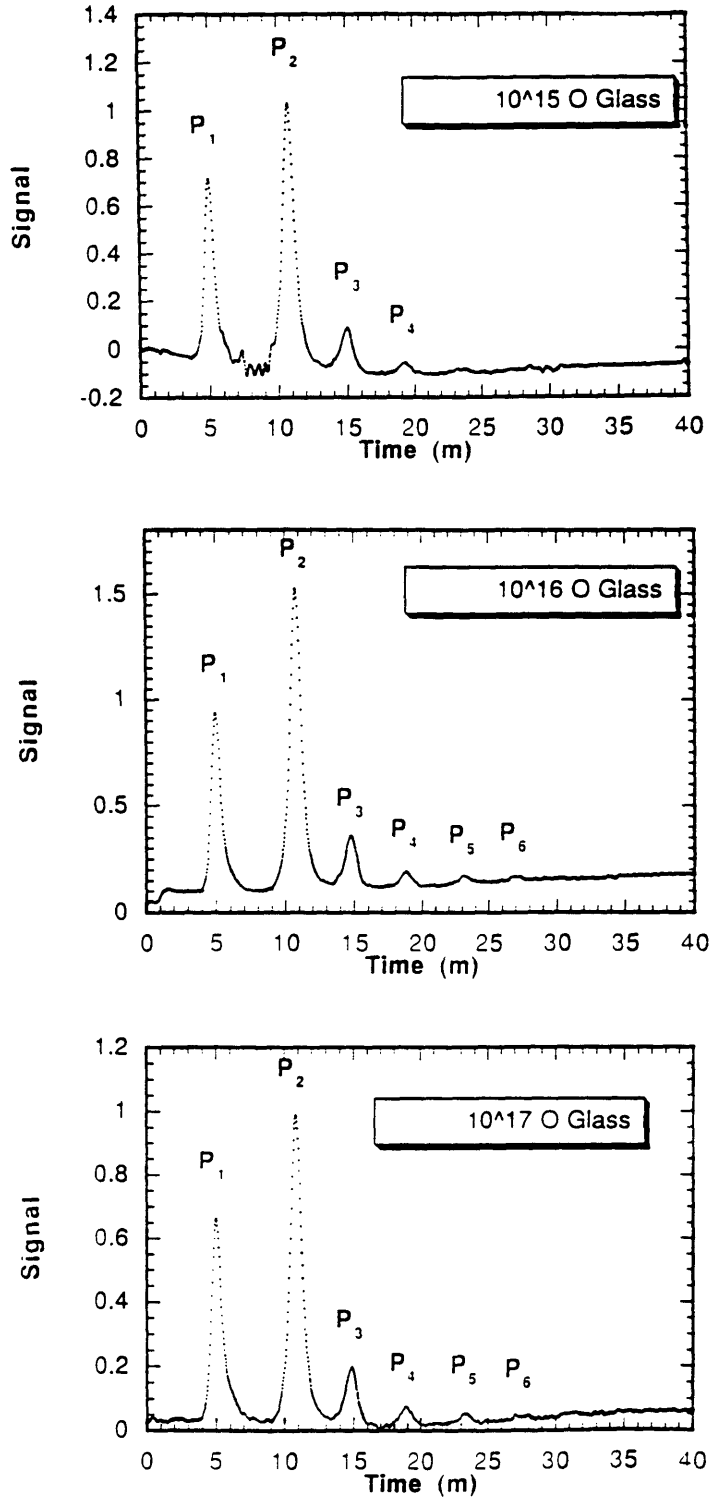

Figure 4-39: HPLC chromatograms for O^+ ion-irradiated $Pb_2P_2O_7$ glasses. Note that the ion-fluence indicated is in ions/cm^2.

$w(n)$ of total phosphorus contained in various chains is given by

$$w(n) = (\frac{n}{n'(n'-1)}) \times (\frac{n'-1}{n'-2})^{n-2} \times (1 - f_o) \tag{4.1}$$

for $n = 2, 3, 4 \cdots$ and $n' \geq 2$, where n is the chain length, n' is the average length of chains and f_o is the weight fraction of phosphorus present as orthophosphate, i.e. the amount of phosphorus in the first peak of the chromatogram representing total phosphorus present in isolated $[PO_4]$ tetrahedra. Earlier work using HPLC by Sales and coworkers [118, 119] on conventionally prepared lead iron phosphate glasses showed excellent agreement of the polymerization of the glasses as predicted by equation 4.1. Sales *et al.* [68] later showed that though this agreement is excellent for conventionally prepared lead pyrophosphate glass, O^{2+} ion-implanted lead pyrophosphate single crystals did not, however, show good agreement with equation 4.1. Their result is reproduced in Fig. 4-40.

In comparing equation 4.1 to the results of a chromatogram, the parameters f_o and n' were calculated directly from the chromatogram. The predicted concentrations of other chains (equation 4.1) were then fixed with no adjustable parameters. For lead pyrophosphate glass, the measured values of f_o and n' were 0.06 and 2.40 respectively. The values of f_o and n' for P^+ ion-irradiated metamict states (from Fig. 4-37) are 0.1276 & 2.255, 0.0847 & 2.125, 0.1452 & 2.324 and 0.2098 & 2.615 respectively. Tables 4.1 to 4.4 tabulate the measured percent weight fractions ($W'(n)$) of the various $[PO_4]$ chains in these metamict crystals. $W(n)$ is simply $100 \times w(n)$. Also, the difference between the measured weight fraction and that predicted by equation 4.1 is represented by $< W >$ which is calculated as

$$< W(n) >= [\frac{W'(n) - W(n)}{W'(n)}]^2. \tag{4.2}$$

The above analysis shows that for moderate doses $< W(2) >$ is small, i.e. the glass of the measured chain length (of the metamict crystal) will have the pyrophosphate group (a chain of two $[PO_4]$ tetrahedra) very similar to that of the metamict crystal,

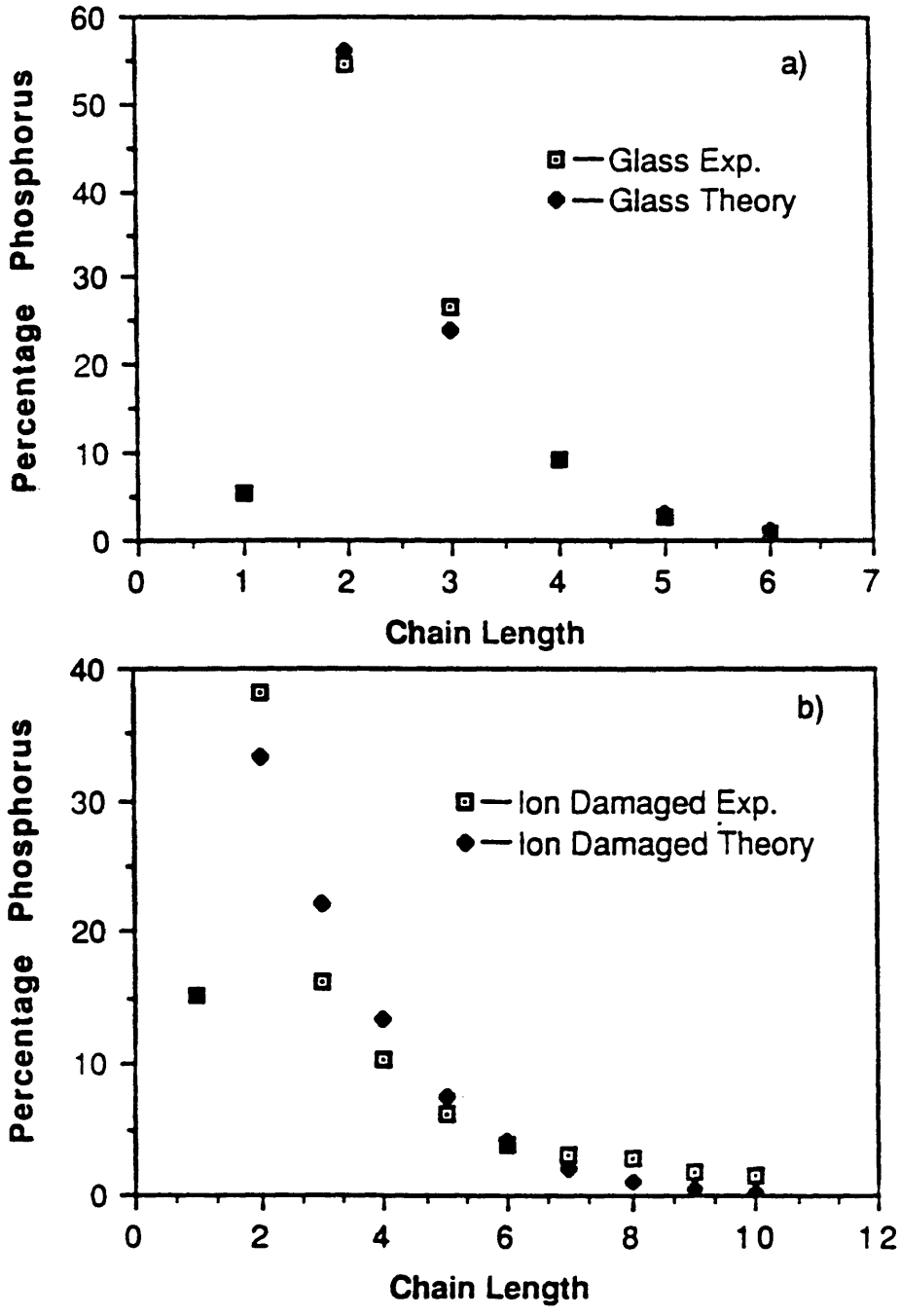

Figure 4-40: Comparison between predictions of the model of Parks and Van Wazer of phosphate chain length distribution and HPLC results from: (a) lead pyrophosphate glass, and (b) metamict lead pyrophosphate single crystal produced by O^{2+} ion-irradiation to a fluence of $10^{21}/m^2$ at an accelerating voltage of 55 keV/ion.

Table 4.1: Measured values of percent weight fractions of the various $[PO_4]$ chains in metamict $Pb_2P_2O_7$ crystals. P^+ dose was $5\times10^{17}/m^2$.

n	$W'(n)$	$W(n)$	$< W(n) >$
2	65.96	61.62	4.33×10^{-3}
3	10.64	18.80	0.5882
4	4.25	5.09	0.0391
5	6.38	1.30	0.6502

Table 4.2: Measured values of percent weight fractions of the various $[PO_4]$ chains in metamict $Pb_2P_2O_7$ crystals. P^+ dose was $5\times10^{18}/m^2$.

n	$W'(n)$	$W(n)$	$< W(n) >$
2	80.51	76.57	2.39×10^{-3}
3	10.64	12.76	0.0397
4	2.54	1.89	0.0655
5	2.21	0.26	0.7698
6	1.06	0.03	0.9442

Table 4.3: Measured values of percent weight fractions of the various $[PO_4]$ chains in metamict $Pb_2P_2O_7$ crystals. P^+ dose was $1\times10^{19}/m^2$.

n	$W'(n)$	$W(n)$	$< W(n) >$
2	62.24	55.58	0.0114
3	10.37	20.39	0.9336
4	6.22	6.65	4.78×10^{-3}
5	3.53	2.03	0.1806
6	2.07	0.60	0.5043
7	1.04	0.17	0.8365

Table 4.4: Measured values of percent weight fractions of the various [PO_4] chains in metamict $Pb_2P_2O_7$ crystals. P^+ dose was $2\times10^{20}/m^2$.

n	$W'(n)$	$W(n)$	$< W(n) >$
2	47.55	37.41	0.0455
3	9.79	21.37	1.3991
4	6.99	10.86	0.3065
5	6.99	5.17	0.0678
6	2.80	2.36	0.0245
7	2.80	1.05	0.3906
8	2.10	0.46	0.6099

but for the highest dose $< W(2) >$ is much larger, indicating that this metamict crystal will be very different from a conventionally prepared glass of similar average chain length. The same is true for the values of $< W(3) >$. These results are complementary to the results from EFED analysis in that even near-medium range is very different for metamict crystals achieved by high fluence ion irradiation. Similar analyses for the P^+ and O^+ ion-irradiated lead pyrophosphate glasses could not be made using equation 4.1, mainly because for all of these metamict materials (except for $2\times10^{20}P^+/m^2$ case) the average chain length was calculated to be less than 2. This anomalous result is attributed to the fact that the metamict glass (ion-irradiated) reacts with moisture in air to form excess orthophosphate group. A higher measured value of f_o would therefore lead to erroneous measurement of n'. Interestingly, metamict crystals (ion-irradiated) are several orders of magnitude more resistant to reaction with moisture [120]. Although all these metamict samples were stored in a dry box (relative humidity $< 2\%$), exposure to moisture while shipping and handling of these materials was inevitable.

Fig. 4-41 summarizes schematically the various phenomena occurring with increasing P^+ ion irradiation dosage into lead pyrophosphate single crystals. All the phenomena that are indicated on this 'phenomenological diagram' have been observed and established for the first time, although it is expected that after a certain high

fluence of the irradiating ion, phase-separation can occur in a ceramic material. Also, the medium-range-order of all the metamict ceramics can be expected to be different for each of the metamict states, but this conclusion has been systematically established for the first time as was seen in the earlier section (4.1.4) where the RDFs of these materials were discussed.

4.3 Topology and Structural Freedom

Critical energy densities deposited in the host material (substrate) expressed as eV/substrate atom (or keV/substrate atom) have been commonly used as a yardstick to measure the ease of amorphization induced by ion irradiation [121, 122]. This parameter, *viz*, the critical energy density per substrate atom, E_{DA}, expressed in the units of eV/substrate atom, is calculated by the the following relationship,

$$E_{DA} = \frac{\phi_i \times F_D \times F.W.}{10^{-8} \times n_i \times \rho \times N_A} \tag{4.3}$$

where ϕ_i is the critical ion irradiation fluence in ions/cm^2 required to render the material diffraction amorphous, F_D is the the net energy per unit length (depth) deposited in nuclear interactions expressed as eV/Å/ion, $F.W.$ is the formula weight of the substrate atoms expressed in grams, n_i is the number of atoms in the formula unit, ρ is the bulk density of the substrate material expressed in grams/cm^3 and N_A is the Avogadro number. The value of F_D is taken as the maximum of the profile as a function of depth, which is in turn calculated from the output of TRIM-92 [123].

TRIM does not explicitly calculate the parameter defined as F_D. However, it can be determined using the energy loss quantities determined by TRIM [124, 125]. The energy loss quantities evaluated by TRIM are defined as follows:

E = ion energy loss to recoils (PKOs)

II = ion ionization energy loss

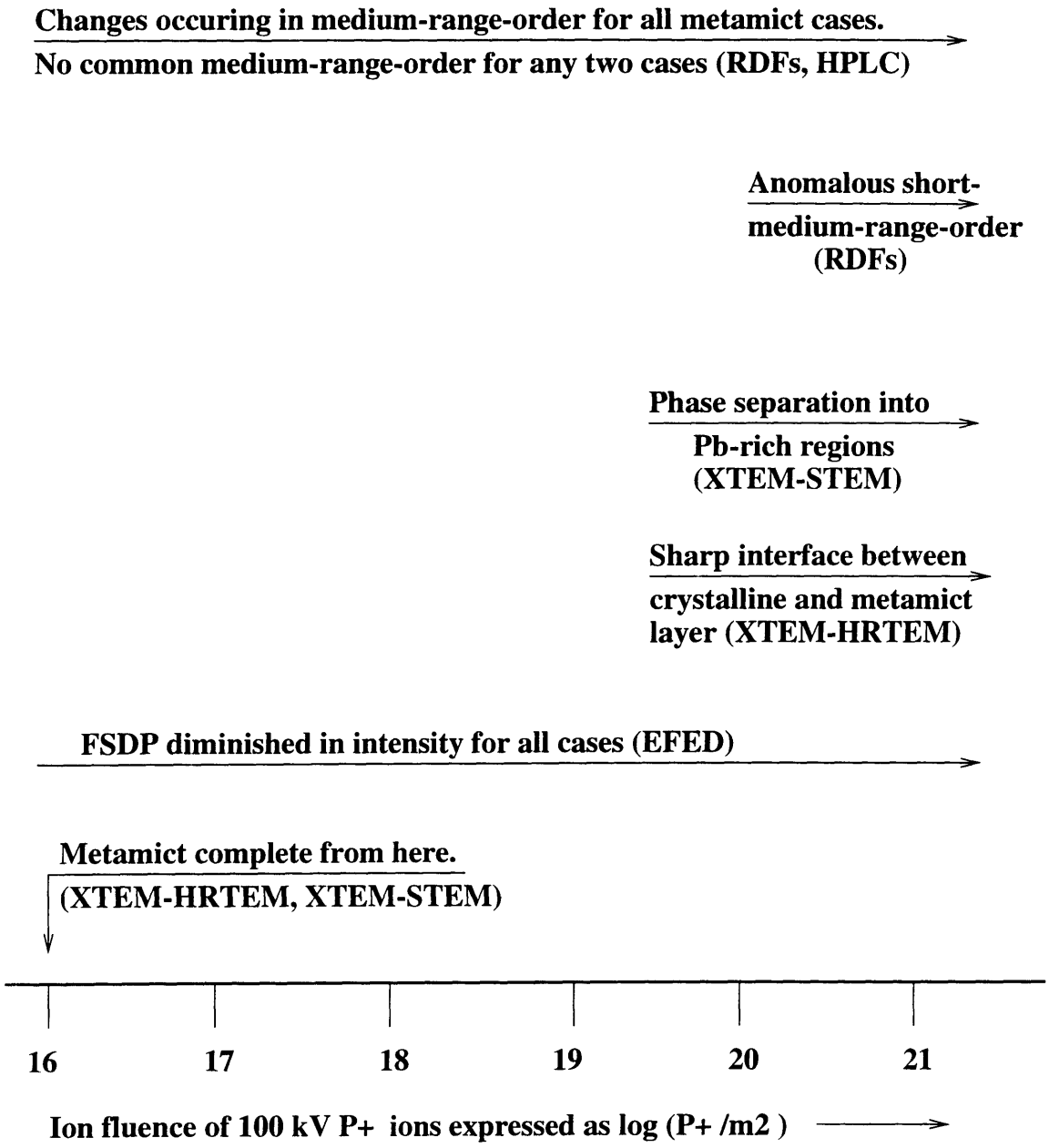

Figure 4-41: A phenomenological phase diagram showing schematically the various phenomena occurring upon increasing P^+ ion irradiation fluence into the lead pyrophosphate single crystals.

IR = recoil ionization energy loss

PI = ion energy loss to phonons

PR = recoil energy loss to phonons

F_D is the total of energy per unit length of *both* ions and recoils deposited in nuclear interactions, schematically shown in Fig. 4-42. Using TRIM-calculated quantities defined above, F_D is therefore evaluated for a given depth as,

$$F_D = E - IR + PI \tag{4.4}$$

As an example, Fig. 4-43 and 4-44 shows these profiles as a function of depth for a 1.5 MeV Kr-ion implantation into zircon.

Table 4.5 catalogues structural freedom and critical amorphization dose for structures comprising a wide range of amorphizability. A correlation is expected, because *excess* constraints in the form of structure connections must be systematically destroyed by irradiation in order to render the structure in another or arbitrary arrangement. The critical amorphization energy densities for (mostly) room temperature ion irradiations were calculated using data from ion-irradiations performed by our group and from those available in the literature. The critical ion fluence for amorphization, type and energy of the implanted ion, and other physical parameters were used to obtain the rates of displacement energy deposition as a function of depth using the TRIM-92 code [123].

Burnett and Page [121] have reported a value of 5090 eV/substrate atom for MgO and a range of values between 3400 and 6800 eV/substrate atom, for α-alumina. More recently, White *et al.* [126] reported a critical ion fluence for MgO of $8\times10^{20}/m^2$ Ti ions at 300kV, from which we calculate a similar value for the critical energy density of amorphization of 5340 eV/substrate atom. McHargue and coworkers [127] also amorphized α-alumina using 170 keV Zr^+ ions to a fluence of 4 $\times10^{16}/cm^2$, from which we calculated a value of 6645 eV/substrate atom which is also in agreement

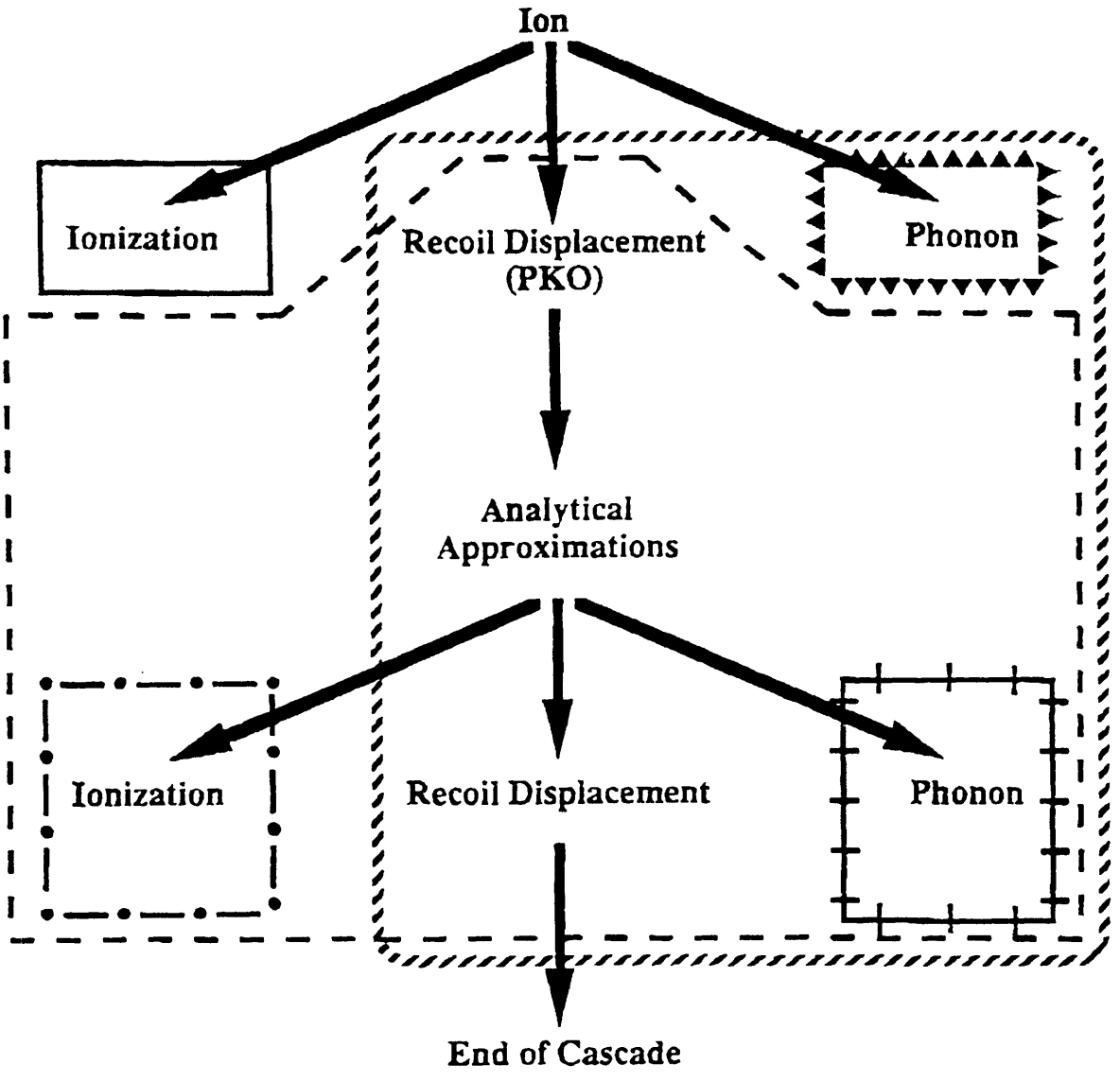

E = ion energy loss to recoils (PKOs)

II = ion ionization energy loss

IR = recoil ionization energy loss

PI = ion energy loss to phonons

PR = recoil energy loss to phonons

F_D = total ion and recoil energy loss to nuclear interactions

Figure 4-42: Schematic representation of energy loss quantities of interest in a binary collision cascade modeled by TRIM-92.

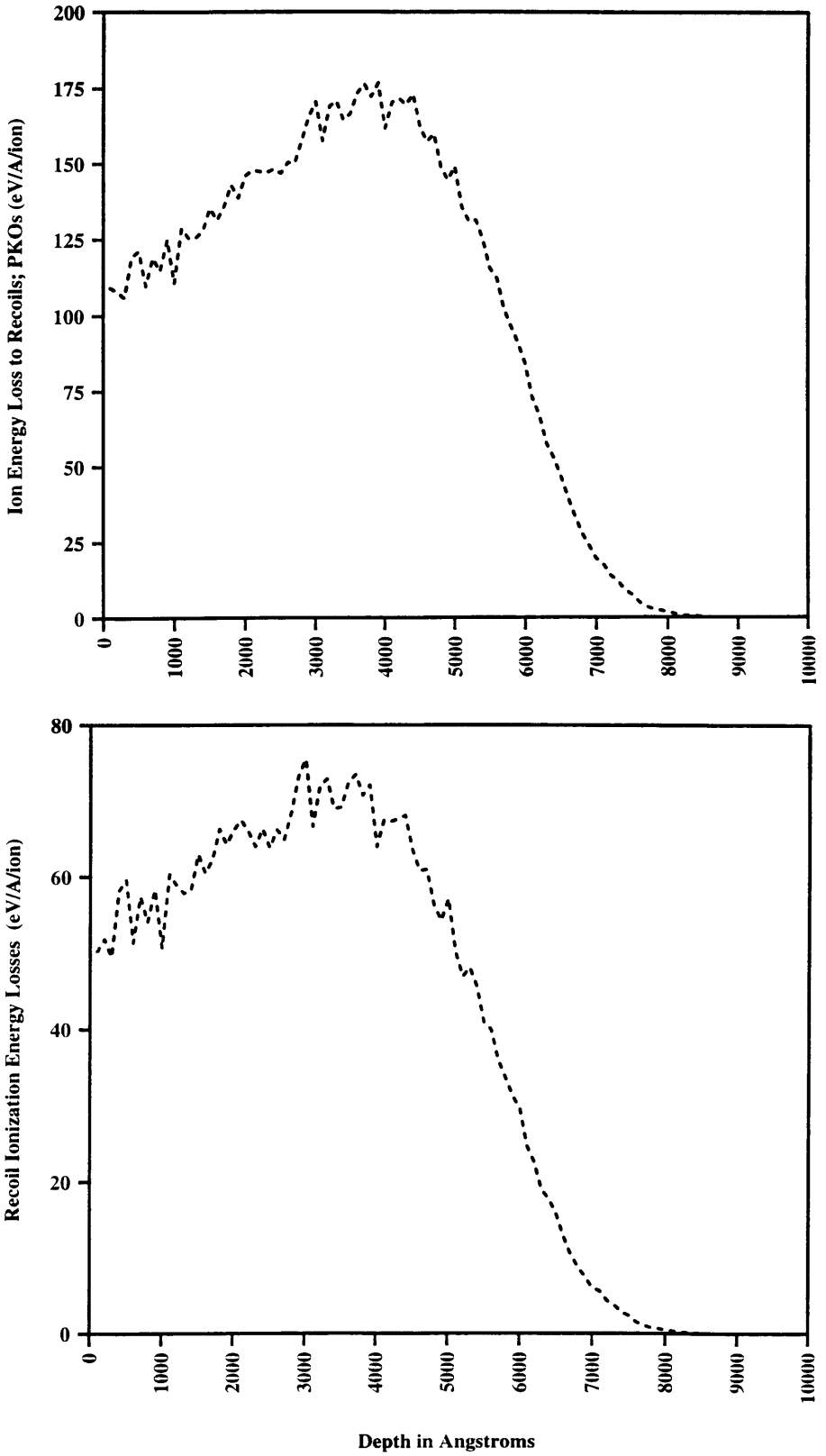

Figure 4-43: Energy loss profiles for 1.5 MeV Kr ion implantation into zircon. (a) Ion energy loss to recoils, E, (b) Recoil ionization energy loss, IR.

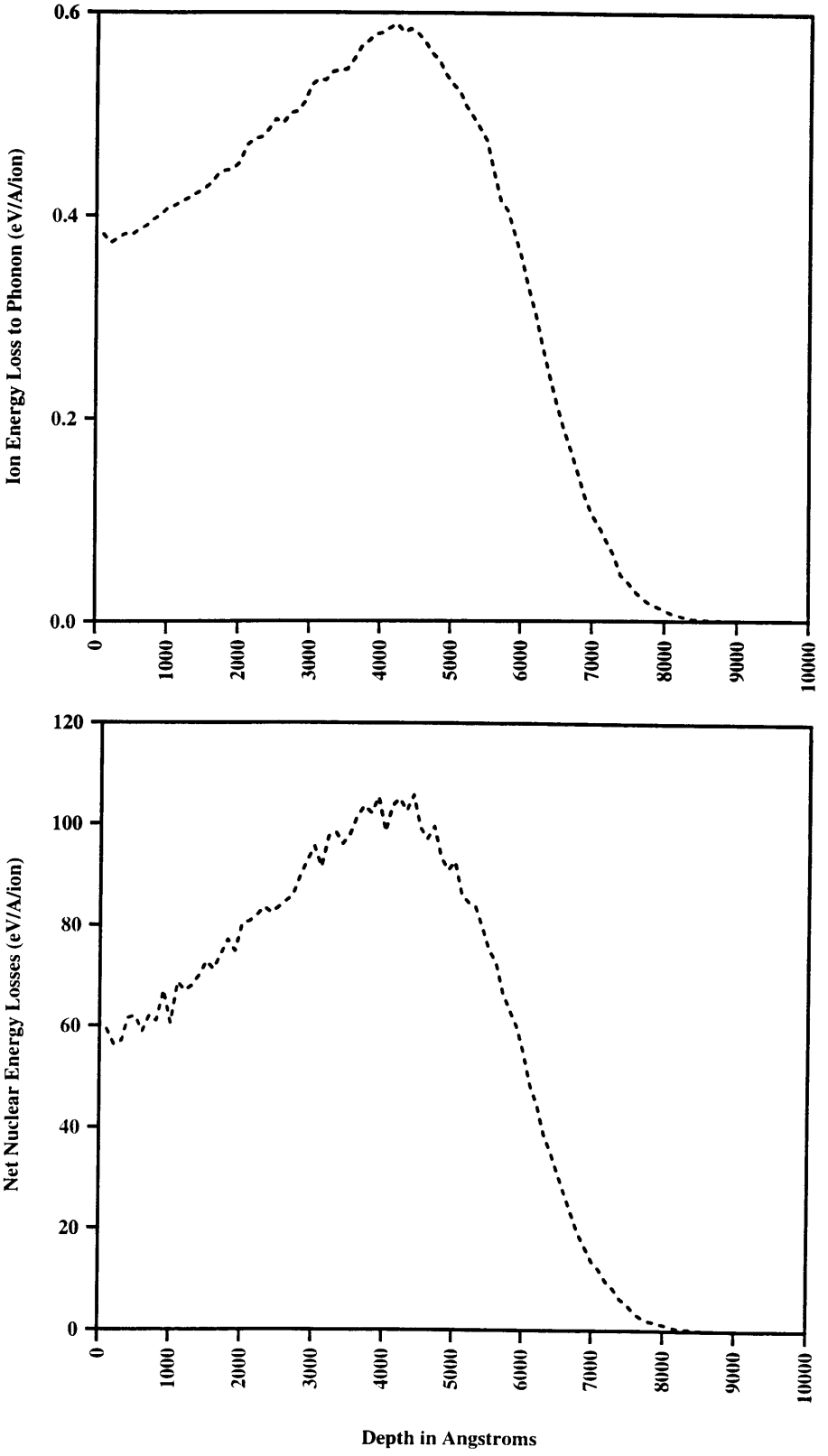

Figure 4-44: Energy loss profiles for 1.5 MeV Kr ion implantation into zircon. (a) Ion energy loss to phonons, PI, (b) Net nuclear energy losses, IR.

Table 4.5: Coordination, connectivity, structural freedom and amorphizability for some network structures. Italicized entries based on atom-centered polytopes which are not coordination polyhedra, see text. * Not measured.

Structure	**Polyhedra : Sharing**	**{V,C}**	f	E_{DA} **(eV/atom)**
MgO	Octahedra : Edges	{6,6}	-10.0	>5000
α-Al_2O_3	Octahedra : Edges, Faces	{6,4}	-6.25	3400-6800
SiC	Tetrahedra : Corners	{4,4}	-3.0	44
Si_3N_4	Tetrahedra : Corners	{4,3}	-1.5	> 700
$CaTiO_3$	~Octahedra : Corners	{6,2}	< -1.0	66
ReO_3	Octahedra : Corners	{6,2}	-1.0	*
SiC	*Tetrahedra : Corners*	*{4,2}*	< 0	*44*
$ZrSiO_4$	Dodecahedra : Edges; Tetrahedra : Edges		-3.0 < f < -1.0	36
$CaSiO_3$	Octahedra : Edges; Tetrahedra : Corners		-1.33 < f < -1.0	11
Si	*Tetrahedra : Corners*	*{4,2}*	< 0	*11*
SiO_2	Tetrahedra : Corners	{4,2}	0	7
$Pb_2P_2O_7$	~Tetrahedra : Corners	{4,1.75}	<+0.4	<0.5
P_2O_5	Tetrahedra : Corners	{4,1.75}	+0.38	*
Si	Rods : Ends	{2,4}	+1.0	11
B_2O_3	Triangles : Corners	{3,2}	+1.0	*

with Page's work [121]. Recently [128], SiC has been amorphized using 1.5 MeV Xe ions at a fluence of $12.55 \times 10^{18}/m^2$, from which we calculate a critical energy density of 44 eV/substrate atom. For zircon ($ZrSiO_4$), wollastonite ($CaSiO_3$) and quartz (SiO_2), the values of E_{DA} of 36.4, 10.55 and 7.25 eV/substrate atom respectively were calculated using data from recent work of Ewing and coworkers [129]. Other values for the critical energy densities were analogously determined from the literature [130, 131, 133, 134].

To a large extent, the critical energy deposited in atomic displacements matches with broad category shifts defined by connectivity. Also different ion species implanted at different energies at varied fluences gave very similar E_{DA} values for a given host (substrate) material. The underconnection of phosphate tetrahedra, for

example, shows up clearly in the extreme susceptibility of the lead pyrophosphate $Pb_2P_2O_7$ to amorphization [130]. Fig. 4-45 shows a stereo view of the crystal connectivity for lead pyrophosphate $Pb_2P_2O_7$. Even though there is some edge sharing with the 8- and 9-fold Pb-coordination polyhedra, corner-sharing of three-connected $[PO_4]$ tetrahedra evidently dominates. This low value of E_{DA} is consistent with both P^+ (room temperature) and O^+ (at 77 K) implantations. Also, Sales *et al.* found that Pb^{3+} implantations into $Pb_2P_2O_7$ single crystals at room temperature and at 77k gave exactly same degree of polymerization (discussed in previous section), suggesting that the implantation temperature is not particularly important for this case.

The correlation works even for smaller structural differences among silicates: the introduction of octahedra or higher polyhedra and edge-sharing in chain silicates (like wollastonite, $CaSiO_3$, and zircon, $ZrSiO_4$, [129]) clearly increases connectivity and decreases amorphizability.

There are a few anomalies: $CaTiO_3$ and other perovskites exhibit surprisingly small amorphization doses for strongly-ionic solids [131], which suggests that the large 8-coordinated alkali or alkaline-earth cation may be less important structurally than the corner-sharing octahedra. There is a precipitous increase in amorphization in going from silicas, in which $[SiO_4]$ tetrahedra are shared two to a vertex, to Si_3N_4, in which $[Si_3N_4]$ tetrahedra are shared three to a vertex (chapter 3). Recent cross-section TEM measurements [132], using ions of sufficiently high-energy that the implantation and damage peaks are well separated, suggest that silicon nitride may not be amorphizable at all at room temperature, earlier reports to the contrary [121] being likely due to chemical influence of implanted ions at high concentration.

The connectivity of Si can be described as {2,4}, but the description renders Si clearly out of place in Table 4.5 with respect to its amorphizability. The rigid tetrahedral bonding of Si makes it topologically more accurate to describe tetrahedra surrounding each Si atom, with unoccupied vertices at bond mid-points, exhibiting a {4,2} connectivity with $f = 0$ instead. The consequential requirement that the Si-vertex-Si angles must be 180° adds an additional constraint, so that f may be a

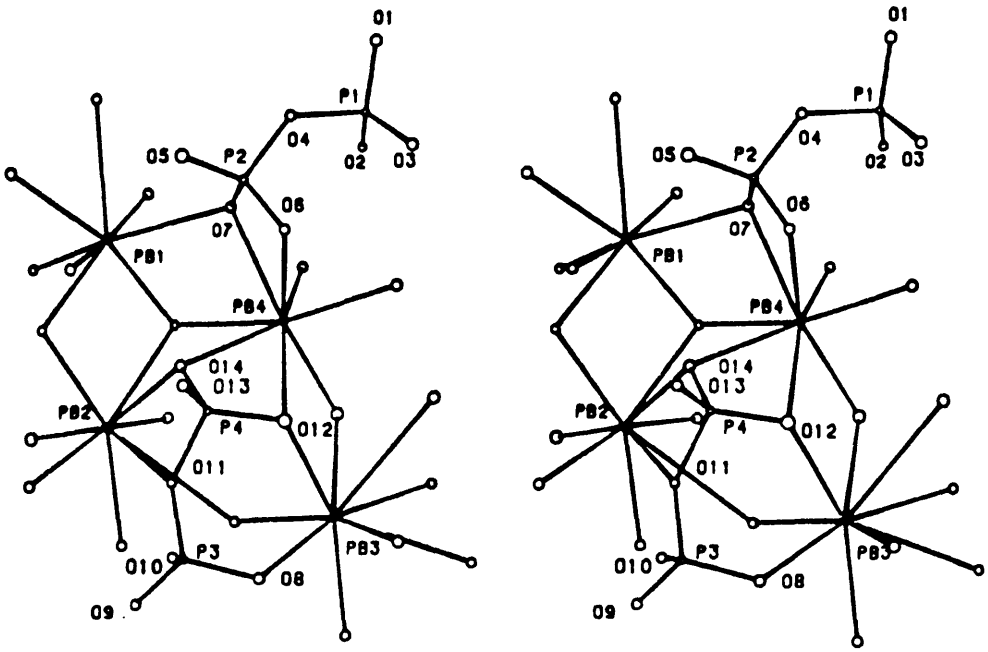

Figure 4-45: Stereo view of the crystal structure of $Pb_2P_2O_7$ crystals.

little < 0, as suggested by silicon's relative amorphizability with respect to silicas.

SiC, with four $[SiC_4]$ (or $[CSi_4]$) tetrahedra to a vertex (Fig. 2), is only somewhat more difficult to amorphize than silicas and is clearly out of place with respect to its apparent redundant connectivities. SiC may be anomalous because of the arbitrariness of assigning the centers of tetrahedra to C or Si atoms (the choice of tetrahedra is not unique) and the possibility of antisite disorder; the atom 'sites' of β-SiC are in fact those of Si, so it may be more appropriate to consider SiC (like GaAs [121]) in the same structural category as Si. From a mechanistic point of view, the redundancy in connectivity at a multiply-shared vertex (chapter 3) represents a liability, and displacement of a single vertex atom destroys *four* tetrahedra.

Chapter 5

Summary of Conclusions

The present study examined the evolution of metamictization in phosphate ceramics and glasses with particular reference to lead phosphates and aluminum orthophosphate. High-resolution electron microscopy, electron amorphography and high-performance liquid chromatography were used as characterization tools to study metamictization of these phosphate ceramics. Topological descriptions of the metamict states were made, and a criterion for topological disorder in metamict states and glasses was proposed.

Principal conclusions drawn from the study are as follows:

1. $Pb_2P_2O_7$ single crystals do not undergo radiolysis up to a fluence of $\sim 10^{27} e/m^2$.

2. $AlPO_4$ single crystals readily amorphize (by radiolysis) homogeneously under TEM electrons by an fluence $\sim 2 \times 10^{23} e/m^2$.

3. $Pb_2P_2O_7$ single crystals undergo metamictization at 100 keV P^+ and 55 Kev O^+ ion irradiation at ion fluence of $< 10^{17}/m^2$ at ambient temperatures and at 77 K respectively.

4. The thickness of the ion-beam induced metamict layers for all the $Pb_2P_2O_7$ compositions was $\sim$ 200 nm and $\sim$ 225 nm for $PbO{\cdot}P_2O_5$ composition.

5. Ion-beam induced metamict interfaces in single crystal $Pb_2P_2O_7$ are sharp above a critical ion fluence threshold of $5\times10^{19}/m^2$ and $1\times10^{20}/m^2$ for P^+ and O^+ implantations respectively.

6. Phase separation of Pb-rich regions occurs for P^+ ion-implanted lead phosphates at and above a fluence threshold of $5\times10^{19}/m^2$.

7. The first sharp diffraction peak (FSDP) intensity is diminished in all ion-implanted metamict lead phosphates.

8. High resolution TEM experiments reveal that amorphization proceeds homogeneously without nucleation of intermediate crystalline structures in ion-implanted lead pyrophosphate single crystals and electron-irradiated aluminum orthophosphate single crystals.

9. Short-range structure, described by the first peak in the reconstructed RDFs (representing the atom correlations in the $[PO_4]$ tetrahedra in the network structure, which occurs at 1.57 Å) is remarkably similar for all aperiodic lead-phosphates.

10. Results from the RDFs of lead phosphate glasses and metamict lead phosphates reveal that the medium-range structure depends on the mode of formation and the precursor.

11. RDFs of metamict lead phosphates show that high-fluence ion irradiation imparts anomalous short-medium-range structure.

12. HPLC results for metamict lead pyrophosphates reveal that higher order polymerization (chains longer than four $[PO_4]$ tetrahedra) increases with higher implanted ion fluence.

13. The process of amorphization, from a simplistic view point, can be thought of as the loss of long-range orientational and positional correlations, but more rigorously as the availability of sufficient structural freedom to accommodate alternative structures, while still maintaining its short-range correlations.

14. Topological (combinatorial) properties govern glass-formation, structural transformations and amorphization. Values of structural freedom $f > 0$ imply freedom to rearrange arbitrarily, while the values of $f < 0$ imply rigid crystalline options.

15. Topological considerations provide more relevant measure of ease of amorphization than empirical parameters such as melting point, ionicity, etc., and in this study have been proposed as a criterion for topological disorder in glasses and metamict materials.

Bibliography

[1] J. H. Gibbs and E. A. DiMarzio, 'Glass Trnasition and Glassy State', *J. Chem. Phys.*, **28**(3), (1958), 373.

[2] E. A. DiMarzio and J. H. Gibbs, 'Glass Temperature of Copolymers', *J. Poly. Sci.*, **XL**, (1959), 121.

[3] W. C. Broegger, Salmonsens Store Illustrede Konversationslexicon, **1**, (1893), 742. Abstract in *Z. Krist.*, **25**, (1896), 427.

[4] A. Hamberg, *Geol. For. Stochn. Foch*, **36**, (1914), 31.

[5] R. C. Ewing, B. C. Chakoumakos, G. R. Lumpkin and T. Murakami, 'The Metamict State', *MRS Bulletin*, (May/June 1987), 58.

[6] L. W. Hobbs, F. W. Clinard, S. J. Zinkle and R. C. Ewing, 'Radiation Effects in Ceramics', *J. Nucl. Mater.*, **216**, (1994), 291.

[7] B. C. Sales and L. A. Boatner, 'Lead-Iron Phosphate Glass: A Stable Storage Medium for High-Level Nuclear Waste', *Science*, **226**, (Oct. 1984), 45.

[8] L. W. Hobbs, 'Topology and Geometry in the Irradiation-Induced Amorphization of Insulators', *Nucl. Instr. Methods Phys.*, **B 91**, (1994), 30.

[9] Hj. Matzke, 'Radiation Damage in Crystalline Insulators, Oxides and Ceramic Nuclear Fuels', *Rad. Effects*, **64**, (1982), 3.

[10] Hj. Matzke and J. L. Whitton, 'Ion-Bombardment-Induced Radiation Damage in some Ceramics and Ionic Crystals', *Canadian J. Phys.*, **44**, (1966), 995.

[11] H. M. Naguib and R. Kelly, Recent Advances in Science and Technology of Materials, ed. A. Bishay, Plenum, New York, vol. 1, (1974), 321.

[12] L. M. Wang, R. K. Eby, J. Janaczek and R. C. Ewing, *Nucl. Instr. Methods Phys.*, B 59/60, (1991), 395.

[13] H. M. Naguib and R. Kelly, 'Criteria for Bombardment-Induced Structural Changes in Non-Metallic Solids', *Rad. Effects*, **25**, (1975), 1.

[14] R. K. Eby, R. C. Ewing and R. C. Birtcher, 'The Amorphization of Complex Silicates by Ion-Beam Irradiation', *J. Mat. Res.*, **7**, (1992), 3080.

[15] T. F. Page, 'Ion Implantation into Ceramics' in Encyclopedia of Materials Science and Engineering, Ed., R. W. Cahn, Suppl. vol. 1, Pergamon, Oxford, (1988), 247.

[16] D. F. Mullica, H. O. Perkins, D. A. Grossie, L. A. Boatner and B. C. Sales, 'Structure of Dichromate-Type Lead Pyrophosphate', *J. Solid State Chem.*, **62**, (1986), 371.

[17] N. Bordes and R. C. Ewing, Ion-Beam and Electron-Beam Induced Amorphization of Berlinite ($AlPO_4$)', Microstructure of Irradiated Materials, *Mater. Res. Soc. Symp. Proc.*, in press, (1995).

[18] J. Biscoe, A. G. Pincus, C. S. Smith and B. E. Warren, 'X-Ray Study of Lime-Phosphate and Lime-Borate Glass', *J. Am. Ceram. Soc.*, **24**, (1941), 116.

[19] G. D. Wignall, R. N. Rothon, G. W. Longman and G. R. Woodward, 'The Structure of Amorphous aluminium Phosphate by Radial Distribution Functions Derived from X-Ray Diffraction. *J. Mater. Sci.*, **24**, (1977), 1039.

[20] E. Philippot, A. Goiffon and M. Maurin, J. Detaint, J. C. Schwartzel, Y. Toudic, B. Capelle and A. Zarka, 'Evaluation of High Quality Berlinite Crystals Grown in Sulphuric Acid Medium', *J. Crytal Growth*, **104**, (1990), 713.

[21] J. W. Mentor, 'The Direct Study by Electron Microscopy of Crystal Lattices and their Imperfections', *Proc. Roy. Soc. Lon.*, **A236**, (1956), 119.

[22] J. M. Cowley, 'The Electron-Optical Imaging of Crystal Lattices', *Acta Cryst.*, **12**, (1959), 367.

[23] J. C. H. Spence, Experimental High Resolution Electron Microscopy, Clarendon Press, Oxford, 1980.

[24] P. R. Buseck, J. M. Cowley and L. Eyring, High-Resolution Transmission Electron Microscopy and Associated Techniques, Oxford Univ. Press, 1988.

[25] L. C. Qin, Sc.D. Thesis, M.I.T., 1994.

[26] W. R. K. Clark, J. N. Chapman, A. M. MacLeod and R. P. Ferrier, 'Radiation Damage Mechanisms in copper Pthalocyanine and its Chlorinated Derivatives', *Ultramicroscopy*, **5**, (1980), 195.

[27] J. C. H. Spence, Experimental High-Resolution Electron Microscopy, Oxford University Press, New York, 1988.

[28] K. Furukawa, 'The Radial Distribution Curves of Liquids by Diffraction Methods', *Rep. Prog. Phys.*, **25**, (1962), 395.

[29] R. L. Mozzi, Ph.D. Thesis, M.I.T., 1968.

[30] A. C. Wright, 'The structure of Amorphous Solids by X-Ray and Neutron diffraction', *Adv. Struc. Res. Diff. Methods*, **5**, (1974), 1.

[31] A. C. Wright and A. J. Leadbetter, 'Diffraction Studies of Glass Strucute', *Phys. Chem. Glasses*, **17**, (1976), 122.

[32] C. W. B. Grigson, 'Studies of Thin Films by Electron Beams', *Adv. Electron. and Electron Phys. suppl.*, 4, (1968), 187.

[33] D. B. Dove, 'electron Diffraction Analysis of Local Atomic Order in Amorphous Films', *Phys. Thin films*, **7**, (1973), 1.

[34] A. C. Wright, 'Neutron and X-Ray Amorphography', in Experimental Techniques of Glass Science, Eds. C. J. Simmons and O. H. El-Bayoumi, Ceramic Transactions, American Ceramic Society, Westerville, Ohio, (1992).

[35] N. F. Mott and H. S. W. Massey, The theory of Atomic Collisions, Oxford University Press, (1965).

[36] C. W. B. Grigson, 'High-Speed Direct Recording System for Electron Diffraction' *Nature*, **192**, (1961), 647.

[37] C. W. B. Grigson, 'Scanning Electron Diffraction System', *J. Jpn. Phys. Soc.*, **17**, Supp.II (1962), 298.

[38] C. W. B. Grigson, D. B. Dove and G. R. Stilwell, 'Some Applications of an Improved Scanning Electron Diffraction System', *Nature*, **205**, (1965), 1198.

[39] M. F. Tompsett and C. W. B. Grigson, 'Scanning Electron Diffraction of Solids', *Nature*, **206**, (1969), 923.

[40] J. Chang and D. B. Dove, 'Scanning electron Diffraction of Amorphous Germanium Films', in Microscopie Electronique 1970, Proc. Seventh Inter. Congr. Electron Microsc., Vol.**2**, Grenoble, (1970), 183.

[41] J. F. Graczyk, Ph.D. Thesis, M.I.T., 1968.

[42] S. C. Moss and J. F. Graczyk, 'Evidence of Voids with the As-Deposited Strucutre of Glassy Silicon', *Phys. Rev. Lett.*, **23**, (1969), 1167.

[43] J. F. Graczyk and P. Chaudhari, 'A Scanning Electron Diffraction Study of Vapor Deposited and Ion Implanted Thin Films of Ge(I)', *Phys. Stat. Sol.(b)* **58**, (1973), 163.

[44] J. F. Graczyk, 'Structure of Glow Discharged Amorphous Silicon', *Phys. Stat. Sol.(a)* **55**, (1979), 231.

[45] D. J. H. Cockayne and D. R. McKenzie, 'Electron Diffraction Analysis of Polycrystalline Amorphous Thin Films', *Acta Cryst.*, **A44**, (1988), 870.

[46] G. R. Anstis, G. J. Auchterlonie and J. C. Barry, 'Investigation of Amorphous Materials by Electron Diffraction - the Effects of Multiple Scattering', *Ultramicroscopy*, **26**, (1988), 65.

[47] A. Sprout, D. R. McKenzie and D. J. H. Cockayne, 'Structural Studies of Hydrogenated Amorphous Silicon-Carbon Alloys', **Phil. Mag., B54**, (1986), 113.

[48] Z. Q. Liu, D. R. McKenzie, D. J. H. Cockayne and D. M. Dwarte, 'Electron Diffraction Study of the Structure of Boron- and Phosphorus-Doped Hydrogenated Amorphous Silicon', **Phil. Mag., B57**, (1988), 753.

[49] W. G. Sainty, D. R. McKenzie, P. J. Martin, R. P. Netterfield, D. J. H. Cockayne and D. M. Dwarte, 'The Structure and Properties of Ion-Beam synthesized Boron Nitride Films', *J. Appl. Phys.*, **64**, (1988), 3980.

[50] E. Lorch, 'Neutron Diffraction by Germania, Silica and Radiation-Damaged Silica Glasses', *J. Phys.* **C2** (1969) 229.

[51] P. Debye, 'Zerstreung von Rontgenstrahlen', *Ann. Physik* 46 (1915) 809.

[52] B.E. Warren, H. Krutter and O. Morningstar, 'Fourier Analysis of X-Ray Patterns of Vitreous SiO_2 and B_2O_3', *J. Am. Cer. Soc.* 19 (1936) 202.

[53] Tswett, Proc. Warsaw Soc. Nat. Sci., Biol. Sect. **14(6)**, (1903).

[54] R. L. M. Synge, 'The Hofmann Degradation of Glutamine Residues in Gliadin', *Biochem. J.*, **33**, (1939), 671.

[55] R. L. M. Synge, 'Amino Acids. I. The Partition of Acetamino Acids Between Immiscible Solvents', **33**, (1939), 1913.

[56] R. L. M. Synge, 'General Review of the Applicability of the Method', Biochem. Soc. Symp., **3**, (1950), 90.

[57] A. J. P. Martin, 'Some Theoretical Aspects of Partition Chromatography', Biochem. Soc. Symp., **3**, (1950), 4.

[58] J. R. Van Wazer, 'Structure and Properties of the Condensed Phosphates. III Solubility Fractionation and Other Solubility Studies', *J. Am. Chem. Soc.*, **72**, Feb., (1950), 644.

[59] J. Gotz, D. Hoebbel and W. Wieker, *J. Non-Cryst. Solids*, **70**, (1987), 615.

[60] J. R. Van Wazer and K. A. Holst, 'Structure and Properties of Condensed Phosphates', *J. Am. Chem. Soc.*, **72**, Feb., (1950), 639.

[61] A. E. R. Westman and P. A. Gartaganis, 'Structural and Thermodynamic Aspects of Phosphate Glasses', *J. Am. Ceram. Soc.*, **40**, (1957), 293.

[62] T. R. Meadowcroft and F. D. Richardson, 'Constitution of Sodium, Potassium, and Lithium Phosphate Glasses', *Trans. Farad. Soc.*, **61**, (1965), 54.

[63] B. C. Sales, R. S. Ramsey, J. B. Bates and L. A. Boatner, 'Investigation of the Structural Properties of Lead-Iron Phosphate Glasses using Liquid Chromatography and Raman Scattering Spectroscopy', *J. Non-Cryst. solids*, **87**, (1986), 137.

[64] B. C. Bunker, G. W. Arnold and J. A. Wilder, 'Phosphate Glass Dissolution in Aqueous Solutions', *J. Non-Cryst. solids*, **64**, (1984), 291.

[65] R. S. Brazell, R. W. Holmberg and J. H. Moneyhun, 'Application of High-Performance Liquid Chromatography-Flow Injection Analysis for the Determination of Polyphosphoric Acids in Phosphorus Smokes', *J. Chromatography*, **290**, (1984), 163.

[66] Y. Hirai, N. Yoza and S. Ohashi, *Chem. Lett.*, (1980), 499.

[67] Y. Hirai, N. Yoza and S. Ohashi, 'Flow Injection Analysis of Inorganic Polyphosphates', *Analytica Chimica Acta*, **115**, (1980), 269.

[68] B. C. Sales, J. O. Ramey, J. C. McCallum and L. A. Boatner, 'Structural Differences Between the Glass State and Ion-Beam-Amorphized States of Lead Pyrophosphates', *J. Non-Cryst. Solids*, **126**, (1990), 179.

[69] L. W. Hobbs, 'Topology and Geometry in the Irradiation-Induced Amorphization of Insulators', *Nucl. Instrum. Meth. Phys. Res.*, **B91**, (1994), 30.

[70] J. C. Maxwell, *Phil. Mag.*, 'On the Calculation of the Equilibrium and Stiffness of Frames', **27**, (1864), 294.

[71] W. H. Zachariasen, 'The Atomic Arrangement in Glass', *J. Am. Chem. Soc.*, **54**, (1932), 3841.

[72] J. L. Finney, 'Random Packings and the Strucutre of Simple Liquids I. The Geometry of Random Close Packing', *Proc. Roy. Soc. Lond.*, **A319**, (1970), 479.

[73] H. S. M. Coxeter 'Regular Polytopes', The Macmillan Company, NY, 2^{ed}, (1973), 165.

[74] N. Rivier, 'Disclination Lines in glasses', *Phil. Mag.*, **A 40 (6)**, (1979), 859.

[75] G. Toulouse and M. Kleaman, 'Principles of a Classification of Defects in Ordered Media', *J. Physique Lett., Paris*, **37**, (1976), L149.

[76] G. Toulouse, 'Symmetry and Topology Concepts for Spin Glasses and Other Glasses', *Phys. Reports*, **49(2)**, (1979), 267.

[77] M. Kleaman and J. F. Sadoc, 'A Tentative Description of the Crystallography of Amorphous Solids', *J. Physique Lett., Paris*, **40**, (1979), L569.

[78] J. F. Sadoc, 'Use of Regular Polytopes for the Mathematical Description of the Order in Amorphous Structures', *J. Non-Cryst. solids*, **44**, (1981), 1.

[79] J. F. Sadoc and R. Mosseri, 'Order and Disorder in Amorphous, Tetrahedrally Coordinated Semiconductors: A Curved-Space Description', *Phil. Mag.*, **B 45 (5)**, (1982), 467.

[80] J. F. Sadoc and R. Mosseri, 'Curved Space Model for Amorphous Structures and its Relation with Diffraction Experiments', *J. de Phys., Paris*, **C8**, (1985), 421.

[81] E. von Fedorow, 'Allgemeinste Krystallisationsgesetze und die darauf fussende eindeutige Aufstellung der Krystalle', *Z. Krist*, **38**, (1904), 321.

[82] J. D. Bernal, 'The Structure of Liquids', *Scientific Am.*, **203**, Aug., (1960), 124.

[83] J. D. Bernal, 'The Bakerian Lecture, 1962: The Structure of Liquids' *Proc. Roy. Soc.*, **A280**, (1964), 299.

[84] M. F. Ashby, F. Spaepen and S. Williams, 'The Structure of Grain boundaries Described as a Packing of Polyhedra', *Acta Met.*, **26**, (1978), 1647.

[85] J. F. Shackelford and J. S. Masaryk, 'The Interstitial Structure of Vitreous Silica', *J. Non-Cryst. Solids*, **30**, (1978), 127.

[86] J. F. Shackelford and B. D. Brown, 'The Lognormal Distribution in the Random Network Structure', *J. Non-Cryst. Solids*, **44**, (1981), 379.

[87] J. F. Shackelford, 'Triangle Rafts - Extended Zachariasen Schematics for Structure Modeling', *J. Non-Cryst. Solids*, **49**, (1982), 19.

[88] J. F. Shackelford and B. D. Brown, 'Characterization of Medium- and Long-Range Structure with connectivity Matrix, *J. Non-Cryst. Solids*, **106**, (1988), 313.

[89] C. S. Marians, "A Language for the Study of Network Silicas' PhD thesis, M.I.T., (1988).

[90] C. S. Marians and L. W. Hobbs, 'The Phase Structure of Aperiodic SiO_2 as a Function of Network Topology', *J. Non-Cryst. Solids*, **106**, (1988), 309.

[91] C. S. Marians and L. W. Hobbs, 'Characterization of SiO_2 surfaces as a Function of Network Connectivity', *J. Non-Cryst. Solids*, **106**, (1988), 317.

[92] C. S. Marians and L. W. Hobbs, 'Local Structure of Silica Glasses', *J. Non-Cryst. Solids*, **119**, (1990), 269.

[93] C. S. Marians and J. K. Burdett, 'Geometric Constraints: A Refined Model for the Structure of Silica Glass', *J. Non-Cryst. Solids*, **124**, (1990), 1.

[94] C. S. Marians and J. K. Burdett, 'Network Properties of Crystalline Silica Polymorphs', *J. Non-Cryst. Solids*, **124**, (1990), 242.

[95] A. R. Cooper, 'Zachariasen's Rules, Madelung Constant, and Network Topology', *Phys. Chem. Glasses*, **19(4)**, (1978), 60.

[96] A. R. Cooper, 'Glass Structure, a Dedication to Zachariasen', *J. Non-Cryst. Solids*, **49**, (1982), 1.

[97] P. K. Gupta and A. R. Cooper, 'Topologically Disordered Networks of Rigid Polytopes', *J. Non-Cryst. Solids*, **123**, (1990), 14.

[98] P. K. Gupta, 'Rigidity, Connectivity, and Glass-Forming Ability', *J. Am. Cer. Soc.*, **76(5)**, (1993), 1088.

[99] J. C. Phillips, 'Topology of Covalent Non-Crystalline Solids I: Short-Range Order in Chalcogenide Alloys', *J. Non-Cryst. Solids*, **34**, 1979, 153.

[100] J. C. Phillips, 'Topology of Covalent Non-Crystalline Solids II: Short-Range Order in Chalcogenide Alloys and A-Si(Ge)', *J. Non-Cryst. Solids*, **43**, 1981, 37.

[101] J. C. Phillips, *Solid State Phys.*, **37**, 1982, 93.

[102] A. J. Garratt-Reed, Private Communication, M.I.T., 1991-1995.

[103] A. Pabst, 'The Metamict State', *Amer. Mineral.*, **37**, (1952), 137.

[104] Y. Eyal and A. Kaufman, 'Alpha-Recoil Damage in Monazite: Preferential Dissolution of the Radiogenic Actinide Isotopes', *Nucl. Techn,*, **58**, (1982), 77.

[105] F. G. Karioris, K. Appaji gowda, L. Cartz and J. C. Labbe, 'Damage Cross-Sections of Heavy Ions in Crystal Structures', *J. Nucl. Mater.*, **108-109**, (1982), 748.

[106] T. C. Ehlert, K. Appaji gowda, F. G. Karioris and L. Cartz, 'Differential Scanning Calorimetry of Heavy Ion Bombarded Synthetic Monazite', *Rad. Effects*, **70**, (1983), 173.

[107] E. R. Vance and K. K. S. Pillay, 'Fission Fragment Damage in Crystalline Phases Possibly Formed in Solidified Radioactive Waste', *Rad. Effects*, **62**, (1982), 25.

[108] N. Bordes and R. C. Ewing, Ion-Beam and Electron-Beam Induced Amorphization of Berlinite ($AlPO_4$)', Microstructure of Irradiated Materials, *Mater. Res. Soc. Symp. Proc.*, in press, (1995).

[109] M. R. Pascucci, J. L. Hutchison and L. W. Hobbs, 'The Metamict Transformation in α-Quartz', *Rad. Effects*, **74**, (1983), 219.

[110] S. R. Elliott, Physics of Amorphous Materials, 2nd. ed., Longman, London, 1990.

[111] S. R. Elliott, 'Medium-Range Structural Order in Covalent Amorphous Solids', *Nature*, **354**, (1991), 445.

[112] A. N. Sreeram and L. W. Hobbs, 'Characterization of Metamictand Glassy Phosphate Ceramics', *Mater. Res. Soc. Symp.Proc.*, **279**, (1993), 559.

[113] S. R. Elliott, 'Origin of the First Sharp Diffraction Peak in the Structure Factor of Covalent Glasses', *Phys. Rev. Lett.*, **67**, (1991), 711.

[114] S. R. Elliott, 'Chemical Ordering of Interstitial Voids: The Origin of the First Sharp Diffraction Peak for Covalent Glasses', *J. Non-Cryst. Solids*, **150**, (1992), 112.

[115] S. R. Elliott, Extended-Range Order, Interstitial Voids and the First Sharp Diffraction Peak of Network Glasses', *J. Non-Cryst. Solids*, (1995), in press.

[116] J. R. Parks and Van Wazer, 'Structure and Properties of the Condensed Phosphates. XII Reorganization Theory and some Applications', *J. Am. Chem. Soc,*, **79**, (1957), 4890.

[117] P. J. Flory, 'Random Reorganization of Molecular Weight distribution in Linear Condensation Polymers', *J. Am. Chem. Soc,*, **64**, (1942), 2205.

[118] B. C. Sales, R. S. Ramsey, J. B. Bates and L. A. Boatner, 'Investigation of the Structural Properties of Lead-Iron-Phosphate Glasses using Liquid Chromatography and Raman Scattering Spectroscopy', *J. Non-Cryst. Solids*, **87**, (1986), 137.

[119] B. C. Sales and L. A. Boatner, 'Optical, Structural, and Chemical Characteristics of Lead-Indium Phosphate and Lead-Scandium Phosphate Glasses', *J. Am. Ceram. Soc.*, **70**, (1987), 615.

[120] B. C. Sales, private communication, 1994.

[121] P. J. Burnett and T. F. Page, 'Criteria for Mechanical roperty Modifications of Ceramic Surfaces by Ion Implantation' *Radiation Effects*, **97**, (1986), 283.

[122] T. F. Page, 'Ion Implantation into Ceramics' in Encyclopedia of Materials Science and Engineering, Ed., R. W. Cahn, Suppl. vol. 1, Pergamon, Oxford, (1988), 247.

[123] J. F. Ziegler, J. P. Biersack and U. Littmark, *The Stopping and Range of Ions in Solids*, Pergamon, New York, 1985.

[124] Dale E. Alexander, private communication, 1994.

[125] Dale E. Alexander, 'TRIM Energy Loss Calculations', Intra-Laboratory Memo, Argonne National Laboratory, January 25, 1995.

[126] C. W. White, C. J. McHargue, P. S. Sklad, L. A. Boatner and G. C. Farlow, 'Ion Implantation and Annealing of Crystalline Oxides', *Materials Science Reports*, **4**, 1989, 41.

[127] C. J. McHargue, G. C. Farlow, C. W. White, J. M. Williams, B. R. Appleton and H. Naramoto, 'The Amorphization of Ceramics by Ion Beams', *Materials Sci. and Eng.*, **69**, (1985), 123.

[128] W. J. Weber, private communication, 1994.

[129] R. K. Eby, R. C. Ewing and R. C. Birtcher, 'The Amorphization of Complex Silicates by Ion-Beam Irradiation', *J. Mater. Res.*, **7 (11)**, (1992), 3080.

[130] A. N. Sreeram and L. W. Hobbs, 'Characterization of Metamictand Glassy Phosphate Ceramics', *Mater. Res. Soc. Symp.Proc.*, **321**, (1994), 26.

[131] J. Rankin, Sc.D. thesis, M.I.T., 1983.

[132] S. J. Zinkle, 'Microstructure of Ion Irradiated Ceramic Insulators', *Nucl. Instrum. Meth. Phys. Res.*, **B91**, (1994), 234.

[133] J. K. N. Lindner, R. Domres and E. H. te Kaat, 'Radiation Damage and Amorphization of Silicon by 6 MeV Ni Ion Implantation', *Nucl. Instrum. Meth. Phys. Res.*, **B39**, (1989), 306.

[134] J. K. N. Lindner, R. Zuschlag and E. H. te Kaat, 'Radiation Damage and Amorphization of Silicon by 2 MeV Nitrogen Ion Implantation', *Nucl. Instrum. Meth. Phys. Res.*, **B62**, (1992), 314.